UNIVERSITÀ
DEGLI STUDI
FIRENZE

DOTTORATO DI RICERCA IN
SCIENZE CHIMICHE

CICLO XXVI

COORDINATORE Prof. Andrea Goti

Syntheses and characterisations of bimetallic star-shaped single molecule magnets

Settore Scientifico Disciplinare CHIM/03

Dottorando
Dott. Pasquale Totaro

Tutore
Prof.ssa *Roberta Sessoli*

Coordinatore
Prof. *Andrea Goti*

Anni 2011/2013

‘Tudo dança

hospedado numa casa

em mudança’

Paulo Leminski

Contents

Chapter 1

Single Molecule Magnet systems

1.1 Introduction

Single molecule magnets (hereafter named SMMs) are a class of compounds of potential technological interest in the new field of molecular spintronics,[1] *i.e.* an emerging technology exploiting in solid-state devices both the intrinsic spin and the charge of electrons.[2] SMMs can be of different chemical nature, they generally are polynuclear coordination complexes of paramagnetic metal ions held together by suitable organic ligands, which often work as an effective shielding among contiguous molecules in the solid. The magnetic centres can be transition-metal, rare-earth ions, or even organic radicals.[3–5] Some of these systems show, at sufficiently low temperature (generally in the liquid helium region), magnetic bistability, which means a slowing down, until a freezing, of the magnetic fluctuations. This phenomenon is revealed, in few cases, by the opening of the magnetic hysteresis.[6] The SMM behaviour results, in most cases, from the combination of a large spin and an easy axis magnetic anisotropy. Contrarily to what occurs in more conventional, bulk, materials, in this case hysteresis has exclusively molecular origin.

These magnetic features can be employed in order to build information storage devices, exploiting the memory effect in the frozen magnetisation of SMMs. Unfortunately, systems studied nowadays show this phenomenon only at technologically prohibitive temperatures. One of the possible approaches to solve this problem, *i.e.* to increase the working temperatures, is based on the rational synthesis of new molecular compounds whose magnetic features, namely spin value and magnetic anisotropy, are increased. This is however not straightforward, as these two parameters are often related in a compensating way.[7]

SMMs, for their nature, work acting as independent units, because each molecule is magnetically almost isolated from the neighbour ones. This happens in the crystalline form, because of the shielding of organic ligand surrounding each magnetic centre. This means that the macroscopic behaviour is due to individual molecules and not from a domain structure of interacting magnetic moments as in bulk traditional magnets, that is, in first approximation, to the scaled-up response of a single molecule.[8] Given the possibility to address the magnetism of a single object it appears clear why, in the last 20 years, these molecules have been considered excellent candidates for molecular spintronics.[1] In order to exploit this feature it is necessary to organise SMMs on a conducting or semiconducting solid interface. Thus, the field of molecular magnetism is currently merging with the field of surface science.

This thesis work mainly reports our synthetic efforts to develop a new synthetic strategy to increase the blocking temperature of a class of tetrairon(III) star-shaped SMM, as well as to increase our understanding of the grafting process of these molecules onto noble metals, thanks to selective deuteration and surface sensitive mass spectrometry.

The work is organised in six chapters. In the following of this first one a brief introduction is reported, discussing about the cornerstones in molecular nanomagnetism, *i.e.* magnetic exchange, magnetic anisotropy and magnetisation dynamics. Finally a brief summary of the different ways to organise SMMs on surfaces is presented.

In the following chapter a new synthetic strategy performed to prepare heterometallic analogues of the tetrairon complex is described, in order to substitute the central ion in the structure. The case of chromium centred clusters has been chosen to test the validity of the synthetic approach. In chapter 3 an EPR investigation on a chromium-centred star-shaped derivative, with strict trigonal symmetry, will be discussed. The feasibility of such a study was achieved thanks to the new synthetic method developed and refined in this work.

Further developments of the synthetic approach, to include a more anisotropic metal ion, like vanadium(III), in the centre of the star-shaped cluster, will be presented in chapter 4, together with the significant achievements in the increase of the blocking temperature and magnetic coercivity.

The same synthetic approach has been employed for the substitution of the external metal ions (chapter 5), trying to prepare a chromium-centred / manganese and chromium-centred / lanthanide clusters. Despite that, in the case of manganese, the final product revealed to be different from the desired one, not having a full control of the reaction, an interesting heptanuclear molecule has been obtained.

Finally, chapter 6 is more surface science oriented, as it deals with an investigation of the grafting mechanism for the tetrairon(III) star-shaped SMM on a gold surface, employing the secondary ion mass spectrometry technique on a selectively deuterated sample.

1.2 Single molecule magnets

1.2.1 Magnetic exchange in polynuclear systems

SMMs are constituted, as far as the aim of this thesis is concerned, by clusters of transition metal ions. The first parameter to consider is thus the total spin S of the ground state of the molecule. Excluding the mononuclear lanthanide complexes[9,10] of high symmetry, in which the orbital contribution is not quenched, a SMM system can be described within the *Spin Hamiltonian* approach, *i.e.* working only with spin operators and treating the orbital contributions as phenomenological parameters. The isotropic exchange contributions is therefore expressed as:

$$\mathcal{H}_{ex} = \sum_{i>j} J_{ij}\, \boldsymbol{S}_i \cdot \boldsymbol{S}_j$$

Equation 1.1

where the sum is over all the pairs of the cluster, often limiting the summation to nearest neighbour i and j spins. J_{ij} is the coupling constant; S_i and S_j are spin operator of the individual spin centres. Exchange couplings (J_{ij}) are said to be *ferromagnetic* or *antiferromagnetic* when they favour parallel or antiparallel alignment of interacting spins, respectively. The resulting spin states, deriving from this treatment, are characterised by a total spin state S_T. The energy of the different S_T states can be calculated analytically only in some high symmetry cases, in particular when a central spin exhibits the same exchange interaction with the neighbouring ones, as the Kambe approach describes.[11]

One of the particular case, in which the Kambe approach is applicable, results to be a tetrameric topology as showed in Figure 1.1, which will be discussed in this thesis.

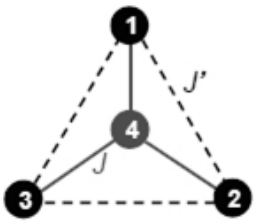

Figure 1.1: Coupling scheme in a star-shaped tetramer. J is the coupling constant between the central and the peripheral spins, J' couples two external spins.

A large family of tetranuclear SMMs presents this specific structure. The first molecule to be synthesised, characterised and studied is the

tetrairon(III) cluster.[12–14] Successively, other analogues, called star-shaped systems, are prepared, using different metal ion.[15,16]

For this tetramer the spin Hamiltonian is described by Equation 1.2:

$$\mathcal{H}_{ex} = J\,[S_1 \cdot S_4 + S_2 \cdot S_4 + S_3 \cdot S_4] + J'\,[S_1 \cdot S_2 + S_2 \cdot S_3 + S_3 \cdot S_1]$$

Equation 1.2

Every spin state, arising from the coupling of the four spins, is defined by three quantum numbers: $|S_\alpha, S_{ext}, S_T\rangle$, where $S_\alpha = S_1 + S_2$, $S_{ext} = S_\alpha + S_3$, and $S_T = S_4 + S_{ext}$. The spin states having the same S_T differ for the other quantum numbers. However, due to the high symmetry, the total energy depends only on S_T and S_{ext}, according to Equation 1.3:

$$E(S_T, S_{ext}) = \frac{J}{2}[S_T(S_T+1) - S_{ext}(S_{ext}+1) - S_4(S_4+1)] + \frac{J'}{2}[S_{ext}(S_{ext}+1) - S_3(S_3+1) - S_2(S_2+1) - S_1(S_1+1)]$$

Equation 1.3

which becomes:

$$E(S_T, S_{ext}) = \frac{J}{2}[S_T(S_T+1) - S_{ext}(S_{ext}+1)] + \frac{J'}{2}[S_{ext}(S_{ext}+1)]$$

Equation 1.4

This simplification brings to Equation 1.4 and is due to the fact that all terms involving local spins S_i introduce only an energy offset.

Therefore, all possible states arising from the coupling of four spins, will have to be accurately counted, in order to consider their correct degeneracy and to calculate their energy following the simplified Equation 1.4. Knowledge of the energy of the spin states then gives full access to the thermodynamic properties of the spin system.

1.2.2 Role of magnetic anisotropy

A further step has to be made in order to better describe, from a magnetic point of view, this type of molecules. The anisotropy has to be considered and in SMMs, the only significant contribution is given by the magneto-crystalline one, in contrast to bulk magnets where surface and shape anisotropy are equally relevant. Magneto-crystalline anisotropy is induced by the combination of spin-orbit coupling with the low symmetry environment, around the metal centres, constituting the SMM. Dipolar contributions are in most cases, but not always, negligible. A quantitative treatment of the magnetic anisotropy is based on the effective Spin Hamiltonian approach, where only the spin variables appear, while the orbital contributions are introduced through parameters.[17] For a general system, with no symmetry, the multipolar expansion up to the second order gives:

$$\mathcal{H}_{anys} = \boldsymbol{S} \cdot \boldsymbol{D} \cdot \boldsymbol{S} = D\left[S_z^2 - \frac{1}{3}S(S+1)\right] + E(S_x^2 - S_y^2)$$

Equation 1.5

where the coordinate frame xyz is taken along the principal axes of the zero field splitting tensor **D**. Its diagonal elements are related to the zero field splitting parameters D and E, which describe the axial and rhombic (or transverse) components of anisotropy respectively, according to the relations:

$$D = D_{zz} - \frac{1}{2}D_{xx} - \frac{1}{2}D_{yy}$$

$$E = \frac{1}{2}(D_{xx} - D_{yy})$$

Equation 1.6

The effect, known as *Zero Field Splitting* (ZFS), of the magnetic anisotropy on the $(2S+1)$ states of the spin multiplet is to remove their degeneracy even in the absence of an external field.

The interesting molecules for our studies are the ones with a negative D value. This value determines, according to Equation 1.5, that the system is much more easily magnetisable when a field is applied along the principal axis, *i.e. z*, named magnetic *easy axis*. Its perpendicular plane is defined as *hard plane* of magnetisation, on which it will then be more difficult having the magnetisation lying.

In SMMs the anisotropy energy is associated to the energy gap in zero field between the states characterized by the largest and smallest $|m|$, where m is the eigenvalue of S_z. In the case of pure axial anisotropy, namely $E = 0$, the gap corresponds to $|D|S^2$ and $|D|(S^2\text{-}1/4)$ for integer and half-integer spins, respectively. A system showing easy axis magnetic anisotropy, having $D < 0$, has the ground doublet characterized by $m = \pm S$, which corresponds to two potential wells separated by an energy barrier,[3] U_{eff}, showed in Figure 1.2 for a zero field case. To each well is associated one direction along the easy axis, on which the magnetisation lies.

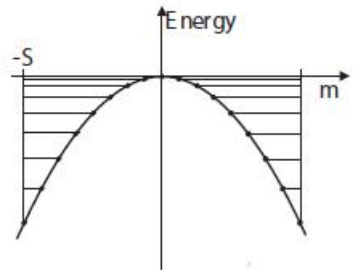

Figure 1.2: Splitting in zero field of the $2S+1$ levels due to an axial anisotropy.

In Figure 1.3 is shown the same energy level, but in the case of non zero field applied.

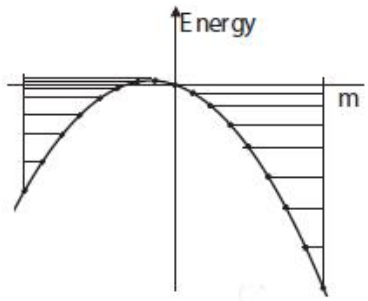

Figure 1.3: Splitting in non zero field of the $2S+1$ levels due to an axial anisotropy.

In the case of a spin system constituted by a single paramagnetic centre carrying $2S$ unpaired electrons, the value of D can be experimentally determined through Electron Paramagnetic Resonance (EPR),[18–20] Inelastic Neutron Scattering (INS)[21] or magnetometry, when performed on a single crystal sample. The magnetic anisotropy can also be estimated theoretically with different methods, as the perturbation theory,[22,23] or a ligand field treatment based on the Angular Overlap Model.[24]

In the case of a polynuclear metal system, such as most SMMs, calculating D value gets more complicated. In general, with first row transition metal ions, it is found that the magnetic anisotropy is weaker than the intra-molecular exchange interactions (strong exchange condition). Hence, the resulting states are well described by the quantum number corresponding to the total spin state, as derived from Equation 1.2, and the magnetic anisotropy is introduced as a perturbation. The magnetic anisotropy of a given total spin state S_T can be related to the single ion contributions, or to the anisotropic part of the interaction, either dipolar or exchange in nature, by using projection techniques:[25]

$$D_{S_T} = \sum_i d_i \boldsymbol{D}_i + \sum_{i>j} d_{ij} \boldsymbol{D}_{ij}$$

Equation 1.7

where i and j run over the magnetic centres inside the SMM. The projection coefficients d_i and d_{ij} depend on how the individual spins project on the total spin state under consideration, and $\mathbf{D_i}$ and $\mathbf{D_{ij}}$ are anisotropy tensors associated with the single ion contributions and with two-spins interactions, respectively. Since the values of d_i and d_{ij} are generally very small, it is not simple to combine a large spin with a large magnetic anisotropy. Although apparently coupling more and more spins to increase S should lead to a quadratic effect on the height of the barrier, the projection of the anisotropies of the single ion makes the barrier scale linearly with S.[7] This aspect will be recalled twice throughout this work, when applied to two different SMMs, which have been synthesised for this study.

We will now introduce the so called giant spin approximation. This consists in evaluating the dynamics of the magnetisation assuming that the whole molecule behaves like a unique large spin, characterised by its axial and transverse anisotropies (derived according to Equation 1.7). This is justified by the fact that at low temperature only the ground spin state is populated.

1.2.3 Dynamics of magnetisation

Slow relaxation of the magnetisation was observed for the first time in a coordination compound constituted by twelve coupled Mn ions, called $Mn_{12}Ac$. Working at sufficiently low temperature, the relaxation becomes slow enough to observe an imaginary component in the alternating current (AC) susceptibility and at even lower temperatures the opening of the hysteresis loops measurements.[6] This impressive slowing down of the fluctuations originates from the double well potential reported in Figure 1.2, characteristic of a large spin with a negative *D* parameter. The application of a magnetic field has the effect of stabilizing and populating preferentially one of the two wells, as showed in Figure 1.3. Once the field is removed, the two wells come back to be equi-energetic, with a part of the population that is transferred from a well to the other, until the equality in population is re-established, giving as result the macroscopic zero magnetisation. Transitions from one state to the other are promoted by deformations of the metal coordination environment (rotations and geometrical strains), which can affect the spin degrees of freedom thanks to spin-orbit coupling. However, at a first level of approximation, these deformations are only able to induce transitions between states differing in m_S by ±1 and ±2. To overcome the energy barrier a multiphonon mechanism is therefore necessary. The overall rate of this relaxation process is determined by the slowest step, as it happens in a chemical reaction. In the case of a SMM, the slowest step is the one on top of the barrier, because at low temperature the highest states are less populated, and also because of the quadratic energy spacing induced by Equation 1.5. The combination of these two factors yields an exponential temperature dependence of the relaxation time, which is typical of a thermally-activated mechanism following the Arrhenius law:

$$\tau = \tau_0 \, e^{\frac{U_{eff}}{k_B T}}$$

Equation 1.8

where U_{eff} is the effective anisotropy barrier and τ_0 is a pre-exponential factor representing the characteristic time of the process.

Also a quantum-type phenomenon in SMMs dynamics of magnetisation, together with the described thermally activated relaxation, can be observed. The latter is poorly efficient at low temperatures and spin reversal takes place by an under-barrier pathway, called quantum tunnelling of magnetisation. Whenever two states, lying on opposite sides of the barrier, have the same energy and the wavefunction of the left well

extends to the right well with a nonzero value, the probability of observing a through-barrier transition is different from zero.[23]

In case of pure axial symmetry, which represents a theoretical scenario, the eigenstates given by $\mathcal{H}_{anys}$ operator (Equation 1.5) are pure m_S states and transitions between the two ground states with $m_S = \pm S$ can only occur through the thermal process schematized in Figure 1.2 and Figure 1.3.[26] However, in a real systems many mechanisms are able to admix states on opposite sides of the barrier. A transverse anisotropy, due to symmetry reduction, or a transverse field, either externally applied or of internal origin, introduces in the $\mathcal{H}_{anys}$ (Equation 1.5) S_x and S_y terms, which admix the states. The eigenstates are, then, described as a linear combination of the pure m_S states:

$$|\Psi_i\rangle = \sum_{m=-S}^{S} \varphi_i(m)|m\rangle$$

Equation 1.9

Generally speaking, if the transverse term is a small perturbation with respect to the axial anisotropy, one of the $|m\rangle$ states is the leading term for each $|\Psi_i\rangle$. This is particularly true for the lowest states in barrier, because the transverse terms in the Spin Hamiltonian only mix these states at a high order of perturbation. In the case of a system with a small spin value, transverse terms, which are inevitable, make the energy barrier become transparent. Then it is not to observe the SMM behaviour coming from the low temperature divergence of the relaxation time.

The possibility of a quantum relaxation depends on the delocalization of the wavefunction, in analogy to the quantum mechanics of a particle in a double well potential. But, in the case of spins, the magnetic field plays an additional role. A field applied along the anisotropy axis, thus coupling with the S_z component of the spin, produces a shift of the levels on both sides of the barrier toward opposite directions. Perturbation theory tells that any admixing is more efficient the closer is the energy of the unperturbed states.

The case of zero field, reported in Figure 1.2, is a special case where all unperturbed levels are degenerate in pairs. This is therefore expected to be a favourite case for tunnel relaxation. However, this energy matching is re-established for other characteristic values of the applied field (Figure 1.3), described by Equation 1.10:

$$H_n = n\frac{|D|}{g\mu_B}$$

Equation 1.10

This behaviour determines the characteristic steps of SMM hysteresis at the resonant field, as showed in Figure 1.4. The vertical segments of the curve reflect accelerations of the relaxation rate and thus can be attributed to the quantum tunnelling process.

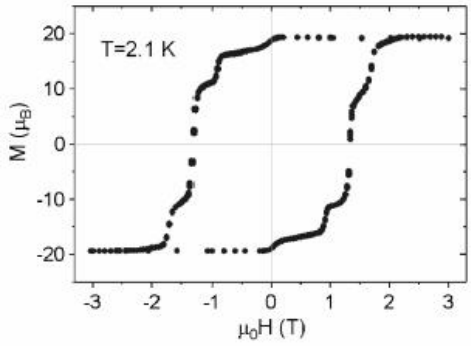

Figure 1.4: Typical stepped hysteresis loop of a SMM ($Mn_{12}Ac$) single crystal with the applied field parallel to the tetragonal axis.[27]

This trend of the magnetisation can be theoretically reproduced with the approach mentioned before, by taking into account that the true eigenstates of the system are not pure $|m\rangle$ states but they are described as linear combination $|\Psi_i\rangle$ according to Equation 1.9.

1.3 SMMs grafted on surfaces

The possibility of exploiting the behaviour of molecular spins for their employment in spintronic devices[28] has stimulated a large interdisciplinary effort in molecular magnetism and surface science. SMM are ideal candidate systems as they possess a large magnetic moment in their ground state which can response to external probes.[29] The interest in the area has certainly been revived since Fe_4-based systems have been demonstrated to retain SMM behaviour when deposited on a surface.[30] From then on many experiments have been performed on these polynuclear systems when interfaced with a surface, showing that Fe_4 exhibits the necessary redox stability and structural robustness. Studies on bulk samples have revealed that Fe_4 clusters in the layers closer to the surface-vacuum interface retain both their static and dynamic magnetic features,[31] as well as the quantum tunnelling of the magnetisation.[32] Some more recent experiments also shed the first light on the transport properties of Fe_4 systems in an electrical junction.[33] All these experiments seem to indicate that the structure and organization of molecules on the surface can be crucial in determining the final properties of a molecular device.

The adsorption of molecules on surfaces is a complex phenomenon, the main novelty, with respect to the bulk material, is represented by the interaction of the SMM with the substrate. Adsorption can be promoted by either nonspecific van der Waals forces (physical adsorption or *physisorption*) or by specific chemical interactions (*i.e.* chemical complementarity) accompanied by a significant change in the electronic states (chemical adsorption or *chemisorption*) due to a strong interaction with the surface. In the former the enthalpies of interactions are significantly lower ($\Delta H<10$ kcal/mol) than in the chemisorption process ($\Delta H>10$ kcal/mol).[35] In addition to surface–molecule interactions, intermolecular forces may still be operative, although with reduced dimensionality (2D) as compared with crystalline phases (3D). Both factors operate in synergy to determine the preferred adsorption geometry. Physisorption is the easiest and, in principle, the least chemically-demanding method to produce surface arrays.

1.3.1 Deposition processes

Two main approaches exist in order to organise SMMs on surfaces. The first is the sublimation of the complex in Ultra High Vacuum (UHV) conditions, commonly used for deposition of thin films of metals on the surface of a substrate, as schematised in Figure 1.5.

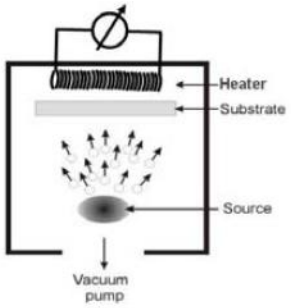

Figure 1.5: Scheme of a metal evaporator.

This technique allows the creation of multicomponent nanostructures and, at variance with solution-based techniques, it does not rely on the chemical properties of the surface, allowing for a wide choice of substrates and for a better control of surface cleanliness. However, as a consequence of the scarce thermal stability of most polynuclear systems, up to now thermal evaporation has found limited applicability in the field of SMMs.[36]

The second is a wet-chemistry method, the easiest one is the *drop casting* method that consists in dissolving a molecule in a volatile solvent, in dropping a specific amount of this solution on the surface and letting the solvent to evaporate. If very dilute solutions have been used, it is statistically possible to achieve a homogeneous deposition. Generally no real chemical bonding occurs between surface and molecule.

A chemisorption process allows a higher control of the deposition: molecules chemically linked to a surface can selectively form a monolayer. This fact is exhaustively exploited in the Self-Assembling of Monolayers (SAMs) technique.[37] It permits to deposit ordered monolayers of molecules on the surface. The structure of the employed molecule is at the basis of this process: the spontaneously occurring interaction between the surface and a linking group (chemical functionality with a strong affinity for a specific substrate) on the molecule is strong enough to form either polar covalent or ionic bonds with the surface, while lateral interactions (through a spacer unit) between adjacent molecules permit a real assembly of these molecules in a bidimensional structure.

Generally, self-assembling occurs in a two steps reaction as showed in Figure 1.6: when the selected substrate is immersed in a solution (usually 10^{-3} M) containing molecules functionalised with a specific linker group, an interaction with surface rapidly occurs; then a slower organisation, that permits the bidimensional ordering, is achieved. After the formation of this deposit the functionalized slide can be extracted from the solution and cleaned with pure solvents that remove the physisorbed material like contaminants and excess of deposited molecules.[38]

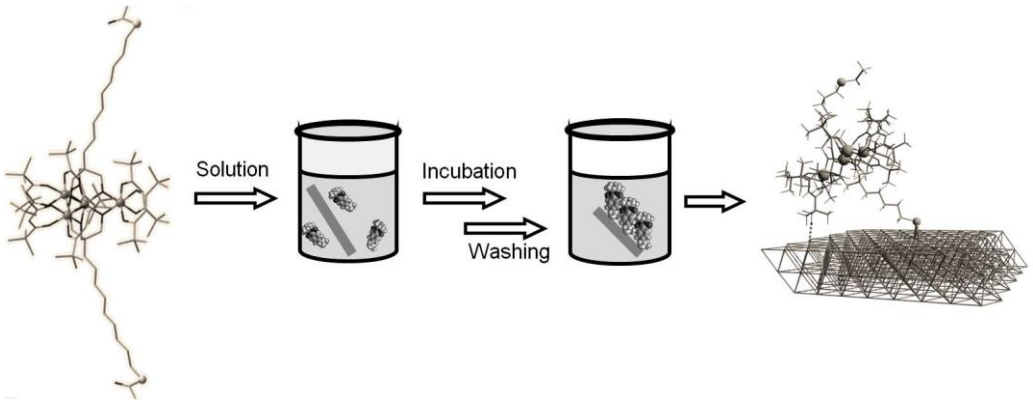

Figure 1.6: Scheme of the preparation of a SAM of Fe_4 derivative on gold through a thioacetyl anchor group.

The specific molecule–substrate interactions involved in chemisorption can embrace a wide range of strengths. As different substrates have different chemical reactivity, a careful design of molecular structure and a proper choice of deposition techniques are essential to achieve the required chemical complementarity between molecule and substrate.

Regarding what we are interested in, namely the deposition of SMMs, in principle a wide type of approaches can be used. The simplest one is to make react a pre-functionalised SMM, that comprises an anchor group, with the substrate, as schematised in Figure 1.6.

It is also possible to introduce the functionalisation of a given surface with a monolayer of ligands bearing ending linking groups that react with the SMM of interest, as displayed in Figure 1.7.[39]

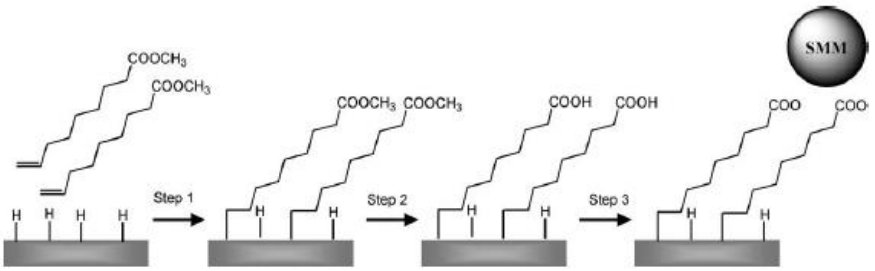

Figure 1.7: Three-steps process used for anchoring SMMs on Si(100).

A third approach explores both the functionalisation of the clusters and the surfaces.[40] Such an approach is based on an electrostatic interaction between a positively charged adsorbate and the surface of interest. A schematic representation of this approach is shown in Figure 1.8

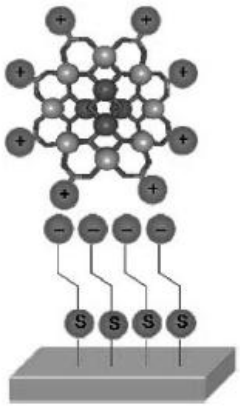

Figure 1.8: Representation of a polycationic Mn_{12} SMM deposited onto a gold surface functionalized with an anionic self-assembled monolayer.

It is important to stress that SAM deposition is a very useful technique for star-shaped based molecules. The relative ease of functionalisation of such molecules allows the introduction of a linking group as will be discussed in 1.4 section, using mild conditions. From a synthetic point of view, that is the aim of this thesis, this permits a full control of the geometry and morphology of the SAM, as well as a control of the interactions between substrate and adsorbate.

1.4 Tetrairon(III) star-shaped SMMs family

Tetrairon(III) clusters, named Fe_4, are among the simplest inorganic systems showing SMM behaviour.[12,14,41] The archetypal member of this class is the tetrairon(III) compound, which is called Fe_4std hereafter, $[Fe_4(\mu\text{-}OMe)_6(dpm)_6]$ (Hdpm = dipivaloylmethane). As shown in Figure 1.9, the four iron(III) ions are arranged in centred-triangular fashion and six methoxide ligands connect a central Fe^{III} ion to three peripheral iron centres, placed at the vertices of an isosceles triangle. Although the cluster has idealized D_3 symmetry, because the inter-ion distances are very similar, the crystallographic symmetry is only C_2 (the twofold axis passes through Fe1 and Fe2). The crystal lattice comprises at least two additional geometric isomers which differ from the major one in the arrangement of the dpm ligands.[12]

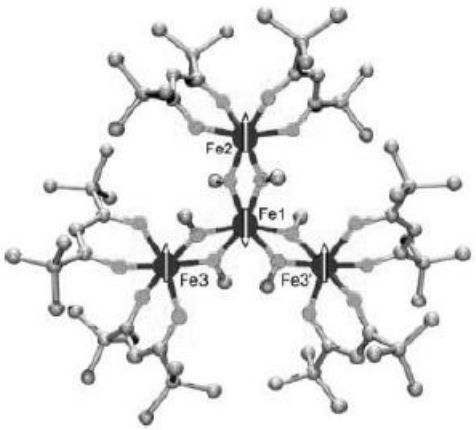

Figure 1.9: Molecular structure of Fe_4std. The arrows give the spin configuration in the $S = 5$ ground state of the molecule. Black: iron(III); light grey: oxygen; grey: carbon.

The cluster is easily synthesized starting from $FeCl_3$, Hdpm and NaOMe according to:

$$2\ FeCl_3 + 4\ Hdpm + 6\ NaOMe \longrightarrow [Fe_2(OMe)_2(dpm)_4] + 4\ MeOH + 6\ NaCl$$

$$3\ [Fe_2(OMe)_2(dpm)_4] + 2\ FeCl_3 + 6\ NaOMe \longrightarrow 2\ [Fe_4(OMe)_6(dpm)_6] + 6\ NaCl$$

Scheme 1.1

The preparation goes through the formation of the dimer $[Fe_2(\mu\text{-}OMe)_2(dpm)_4]$, which is made to react stoichiometrically with additional

$FeCl_3$ and NaOMe in a Et_2O/MeOH solvent, to afford the Fe_4std cluster in good yield.[14]

Due to the S = 5/2 spin of each iron(III) ion and the antiferromagnetic coupling between the central ion and each peripheral one, the ground spin state has S = 5. For what concerns the ZFS parameters, D is negative, as typical for an easy axis system, and equal to -0.206 cm^{-1} and E = 0.010 cm^{-1}. SMM behaviour is thus observed, though at very low temperature due to the low anisotropy barrier (U_{eff}/k_B = 3.5 K).[12]

A significant step in the improvement of the magnetic properties of this SMM has been achieved by replacing the six methoxide bridges in the structure with as many oxygen donor atoms of two tripodal alkoxide ligands H_3L, with formula R-C(CH2OH)$_3$, which are placed on the opposite sides of the tetrairon discoid.[13] The ligand substitution reaction is:

$$[Fe_4(OMe)_6(dpm)_6] + 2\ H_3L \longrightarrow [Fe_4(L)_2(dpm)_6] + 6\ MeOH$$

Scheme 1.2

Figure 1.10: Sketch of a site specific substitution reaction performed on Fe_4std by using tripodal ligands with formula R-C(CH_2OH)$_3$.

This site-specific ligand replacement has major consequences on the molecular properties of the new clusters, when compared to Fe_4std. Upon ligand replacement, the magnetic properties are in general enhanced. Slightly changes in the coordination geometry induce an almost doubling of the D parameters, and most derivatives present also an increased axial symmetry, in some cases crystal imposed D_3 symmetry, both effects contributing to a dramatic increase of the energy barrier, reaching values of the barrier up to 17 K.[13] Despite this achievement, in order to directly observe the blocking of the magnetization, it is still necessary to reach sub-Kelvin temperatures.

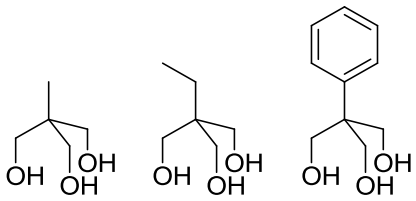

Figure 1.11: H_3L ligands used in this work. Respectively R = Me, Et, Ph.

The chelating effect of the tripodal ligands also makes the complex much more stable in solution than its Fe_4std precursor. This induced feature, together with the possibility to perform a wide-range of modifications on the triol ligands, have been widely exploited to organise such a type of molecules on surface. Through the introduction of tripodal ligands functionalised with a suitable anchor group in the R part of the molecule, it has been possible to deposit Fe_4 on surfaces, in order to characterise its magnetic property as a mono or multi-layer.

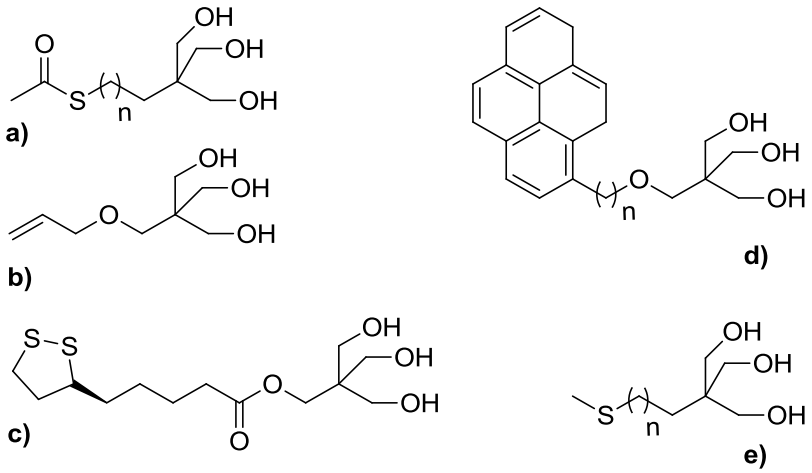

Figure 1.12: Some example of tripodal ligand able to bound surfaces.

The H_3L ligands comprise the three functional units that are necessary to form a self assembly monolayer, SAM: the complexing unit (tripodal alkoxide) that forms the magnetic core, the spacer and the linker. The spacer determines the distance, thus the interaction intensity, between the magnetic centres and the surface. Depending on the surface the molecule has to bind, the linker can have different chemical structures. For a H-functionalised silicon solid interface, a double bond can be employed (Figure 1.12b).[42] The pyrene-ring functionalisation (Figure 1.12d) can exploit π-stacking interaction to be bound to carbon nanotubes.[43] The sulphur functionalised triols are able to be adsorbed on a gold surface, with various options.[30,32,44–47]

(1) Sanvito, S. *Nat. Mater.* **2007**, *6*, 803–804.

(2) Wolf, S. A.; Awschalom, D. D.; Buhrman, R. A.; Daughton, J. M.; von Molnár, S.; Roukes, M. L.; Chtchelkanova, A. Y.; Treger, D. M. *Science* **2001**, *294*, 1488–1495.

(3) Gatteschi, D.; Sessoli, R.; Villain, J. *Molecular Nanomagnets*; Oxford University Press: Oxford, **2006**; p. 361.

(4) Caneschi, A.; Gatteschi, D.; Sessoli, R.; Barra, A. L.; Brunel, L. C.; Guillot, M. *J. Am. Chem. Soc.* **1991**, *113*, 5873–5874.

(5) Sessoli, R.; Tsai, H. L.; Schake, A. R.; Wang, S.; Vincent, J. B.; Folting, K.; Gatteschi, D.; Christou, G.; Hendrickson, D. N. *J. Am. Chem. Soc.* **1993**, *115*, 1804–1816.

(6) Thomas, L.; Lionti, F.; Ballou, R.; Gatteschi, D.; Sessoli, R.; Ballou, B. *Nature* **1996**, *383*, 145–147.

(7) Waldmann, O. *Inorg. Chem.* **2007**, *46*, 10035–10037.

(8) Cornia, A.; Mannini, M.; Sainctavit, P.; Sessoli, R. *Chem. Soc. Rev.* **2011**, *40*, 3076–3091.

(9) Ishikawa, N.; Sugita, M.; Ishikawa, T.; Koshihara, S.-Y.; Kaizu, Y. *J. Am. Chem. Soc.* **2003**, *125*, 8694–8695.

(10) Sessoli, R.; Powell, A. *Coord. Chem. Rev.* **2009**, *253*, 2328–2341.

(11) Kambe, K. *J. Phys. Soc. Japan* **1950**, *5*, 48–51.

(12) Barra, a. L.; Caneschi, a.; Cornia, a.; Fabrizi de Biani, F.; Gatteschi, D.; Sangregorio, C.; Sessoli, R.; Sorace, L. *J. Am. Chem. Soc.* **1999**, *121*, 5302–5310.

(13) Cornia, A.; Fabretti, A. C.; Garrisi, P.; Mortalò, C.; Bonacchi, D.; Gatteschi, D.; Sessoli, R.; Sorace, L.; Wernsdorfer, W.; Barra, A.-L. *Angew. Chemie (International ed.)* **2004**, *43*, 1136–1139.

(14) Accorsi, S.; Barra, A.-L.; Caneschi, A.; Chastanet, G.; Cornia, A.; Fabretti, A. C.; Gatteschi, D.; Mortalo, C.; Olivieri, E.; Parenti, F.; Rosa, P.; Sessoli, R.; Sorace, L.; Wernsdorfer, W.; Zobbi, L. *J. Am. Chem. Soc.* **2006**, *128*, 4742–4755.

(15) Tancini, E.; Rodriguez-Douton, M. J.; Sorace, L.; Barra, A.-L.; Sessoli, R.; Cornia, A. *Chem. Eur. J.* **2010**, *16*, 10482–10493.

(16) Totaro, P.; Westrup, K. C. M.; Boulon, M.-E.; Nunes, G. G.; Back, D. F.; Barison, A.; Ciattini, S.; Mannini, M.; Sorace, L.; Soares, J. F.; Cornia, A.; Sessoli, R. *Dalt. Trans.* **2013**, *42*, 4416–4426.

(17) Abragam, A.; Bleaney, B. *Electron Paramagnetic Resonance of Transition Ions*; Dover Publications: New York, **1986**.

(18) A, B.; Gatteschi, D. *Transit. Met. Chem.* **1982**, *8*, 1.

(19) Gatteschi, D.; Barra, A. L.; Caneschi, A.; Cornia, A.; Sessoli, R.; Lorenzo, S. *Coord. Chem. Rev.* **2006**, *250*, 1514–1529.

(20) Campbell, S. J.; Booth, J. G.; Cadogan, J. M.; Hicks, T. J.; Rhyne, J. J.; Shinjo, T.; Wiesinger, G.; Barra, A. L.; Caneschi, A.; Gatteschi, D.; Sessoli, R. *J. Magn. Mater.* **1998**, *177*, 709–710.

(21) Caciuffo, R.; Amoretti, G.; Murani, A.; Sessoli, R.; Caneschi, A.; Gatteschi, D. *Phys. Rev. Lett.* **1998**, *81*, 4744–4747.

(22) Barra, A.-L.; Gatteschi, D.; Sessoli, R.; Abbati, G. L.; Cornia, A.; Fabretti, A. C.; Uytterhoeven, M. G. *Angew. Chemie Int. Ed.* **1997**, *36*, 2329–2331.

(23) Goldberg, D. P.; Telser, J.; Krzystek, J.; Montalban, A. G.; Brunel, L.-C.; Barrett, A. G. M.; Hoffman, B. M. *J. Am. Chem. Soc.* **1997**, *119*, 8722–8723.

(24) Bencini, A.; Ciofini, I.; Uytterhoeven, M. G. *Inorganica Chim. Acta* **1998**, *274*, 90–101.

(25) Bencini, A.; Gatteschi, D. *Electron Paramagnetic Resonance of Exchange Coupled Systems*; Springer-Verlag: Berlin, **1990**; p. 287.

(26) Villain, J.; Hartman-Boutron, F.; Sessoli, R.; Rettori, A. *Europhys. Lett.* **1994**, *27*, 159–164.

(27) Sessoli, R.; Gatteschi, D.; Caneschi, A.; Novak, M. *Nature* **1993**, *365*, 141–143.

(28) Bogani, L.; Wernsdorfer, W. *Nat. Mater.* **2008**, *7*, 179–186.

(29) Leuenberger, M. N.; Loss, D. *Nature* **2001**, *410*, 789–793.

(30) Mannini, M.; Pineider, F.; Sainctavit, P.; Danieli, C.; Otero, E.; Sciancalepore, C.; Talarico, A. M.; Arrio, M.-A.; Cornia, A.; Gatteschi, D.; Sessoli, R. *Nat. Mater.* **2009**, *8*, 194–197.

(31) Mannini, M.; Pineider, F.; Sainctavit, P.; Joly, L.; Fraile-Rodríguez, A.; Arrio, M.-A.; Cartier dit Moulin, C.; Wernsdorfer, W.; Cornia, A.; Gatteschi, D.; Sessoli, R. *Adv. Mater.* **2009**, *21*, 167–171.

(32) Mannini, M.; Pineider, F.; Danieli, C.; Totti, F.; Sorace, L.; Sainctavit, P.; Arrio, M.; Otero, E.; Joly, L.; Cezar, J. C.; Cornia, A.; Sessoli, R. *Nature* **2010**, *468*, 417–421.

(33) Burzurí, E.; Zyazin, A. S.; Cornia, A.; van der Zant, H. S. J. *Phys. Rev. Lett.* **2012**, *109*, 147203.

(34) Wiesendanger, R. *Scanning Probe Microscopy and Spectroscopy: Methods and Applications*; Cambridge University Press: Cambridge, **1994**; p. 637.

(35) Zangwill, A. *Physics at Surfaces*; Cambridge University Press: Cambridge, **1988**; p. 454.

(36) Margheriti, L.; Mannini, M.; Sorace, L.; Gorini, L.; Gatteschi, D.; Caneschi, A.; Chiappe, D.; Moroni, R.; de Mongeot, F. B.; Cornia, A.; Piras, F. M.; Magnani, A.; Sessoli, R. *Small* **2009**, *5*, 1460–6.

(37) Schreiber, F. *Prog. Surf. Sci.* **2000**, *65*, 151–257.

(38) Ulman, A. *Chem. Rev.* **1996**, *96*, 1533–1554.

(39) Gómez-Segura, J.; Veciana, J.; Ruiz-Molina, D. *Chem. Commun.* **2007**, 3699–3707.

(40) Coronado, E.; Forment-Aliaga, A.; Romero, F. M.; Corradini, V.; Biagi, R.; De Renzi, V.; Gambardella, A.; Del Pennino, U. *Inorg. Chem.* **2005**, *44*, 7693–7695.

(41) Saalfrank, R. W.; Scheurer, A.; Bernt, I.; Heinemann, F. W.; Postnikov, A. V; Schünemann, V.; Trautwein, A. X.; Alam, M. S.; Rupp, H.; Müller, P. *Dalt. Trans.* **2006**, 2865–2874.

(42) Pellegrino, G.; Motta, A.; Cornia, A.; Spitaleri, I.; Fragalà, I. L.; Condorelli, G. G. *Polyhedron* **2009**, *28*, 1758–1763.

(43) Danieli, C.; Cornia, A.; Cecchelli, C.; Sessoli, R.; Barra, A.-L.; Ponterini, G.; Zanfrognini, B. *Polyhedron* **2009**, *28*, 2029–2035.

(44) Perfetti, M.; Pineider, F.; Poggini, L.; Otero, E.; Mannini, M.; Sorace, L.; Sangregorio, C.; Cornia, A.; Sessoli, R. *Small* **2013**.

(45) Barra, A.-L.; Bianchi, F.; Caneschi, A.; Cornia, A.; Gatteschi, D.; Gorini, L.; Gregoli, L.; Maffini, M.; Parenti, F.; Sessoli, R.; Sorace, L.; Talarico, A. M. *Eur. J. Inorg. Chem.* **2007**, *2007*, 4145–4152.

(46) Rodriguez-Douton, M. J.; Mannini, M.; Armelao, L.; Barra, A.-L.; Tancini, E.; Sessoli, R.; Cornia, A. *Chem. Commun.* **2011**, *47*, 1467–1469.

(47) Pineider, F.; Mannini, M.; Danieli, C.; Armelao, L.; Piras, F. M.; Magnani, A.; Cornia, A.; Sessoli, R. *J. Mater. Chem.* **2010**, *20*, 187–194.

Chapter 2

Fe_3Cr star-shaped SMMs

2.1 Heterometallic star-shaped SMMs

We have seen, in the previous chapter, the crucial parameters that mostly influence the magnetic bistability of molecules, namely the spin of the molecule and its magnetic anisotropy. Alteration of the magnetic core of already investigated SMMs, with the insertion of different metal ions at specific sites, is of great interest as a route for the enhancement of magnetic properties and clarification of the origin of magnetic anisotropy. This approach is particularly well suited to the class of tetranuclear SMMs of general formula $[M_4(\mu\text{-}OMe)_6(dpm)_6]$ or $[M_4(L)_2(dpm)_6]$ previously described, which have demonstrated to have an unprecedented robustness among polynuclear coordination complexes and a very useful chemical versatility, which has allowed to obtain different types of nanostructures.

First attempts to substitute an iron(III) in the Fe_4 cluster with a different tripositive metal ion, with similar ionic radii, were performed by Cornia's group.[1] In particular they managed to introduce a Cr(III) ion into the centre of the star shaped structure, with negligible metal scrambling among central and peripheral positions. The synthesis brought to a Fe_4 isomorphous heteronuclear complex, $[Fe_3Cr(L^{Ph})_2(dpm)_6]\cdot Et_2O$, in which the chromium spin value $S=3/2$, antiferromagnetically coupled with the peripheral ions, confers an increase of the total spin of the molecule to $S=6$ (for Fe_4 complexes $S=5$), even if with a decrease of the energy to $D\simeq 9$ K, in comparison with $D\simeq 20$ K for Fe_4.

The synthesis of the chromium centred $[Fe_3Cr(L^{Ph})_2(dpm)_6]\cdot Et_2O$ goes through a "one-pot" reaction from stoichiometric amounts of suitable iron(III) and chromium(III) precursors and a slight excess of the tripodal alcohol (H_3L^{Ph} = 2-hydroxymethyl-2-phenylpropane-1,3-diol), as showed in Scheme 2.1b as general procedure. High-frequency EPR and magnetic studies indicated, however, that the crystalline product of this synthesis was a solid solution of chromium-centred Fe_3Cr ($S=6$, 84%) and Fe_4 ($S=5$, 16%) species which co-crystallise in the same environment.[1]

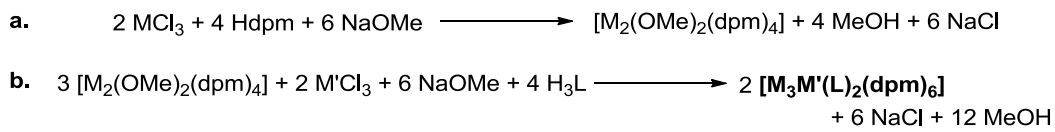

Scheme 2.1: M is referred to Fe and M' to Cr.

2.2 Synthetic strategy for Fe_3Cr cluster

In this thesis, an alternative, stepwise synthetic approach for heterometallic aggregates has been devised, aimed first, at minimizing metal scrambling during assembly of the polynuclear frame, which brings to the formation of an homometallic cluster and, secondly, at tailoring the magnetic properties of the products by convenient choice of metal ions and ligands in the starting materials. This new synthetic route, which has been here first employed, has to be more flexible in terms of selection of metal ions to be used, and for this reason a modular and stepwise approach has been developed.

The preparation of Fe_3Cr aggregates is based on the initial formation of an anionic core structure, $\{Cr^{III}L_2\}^{3-}$, subsequently trapped by reaction with three equivalents of $\{Fe(\beta\text{-diketonate})_2\}^{+}$, forming the peripheral blocks of the final complex, to give the desired chromium-centred triangular topology.

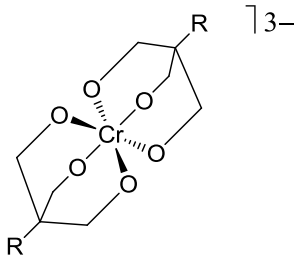

Figure 2.1: Chromium core topology.

Due to its well-known chemical inertness, chromium(III) was expected to produce a kinetically stable, central core unit, and was then selected to test the feasibility of the synthetic proposal. This modular approach should, however, be general enough to allow combinations of a variety of M/M'-containing building blocks (M, M' = different d- and/or f-block metals) and to significantly expand the number of "designed" heterometallic products.

The overall synthetic strategy consists in the reaction of a dimeric iron(III) unit with the preformed chromium(III) core, previously mentioned as showed below:

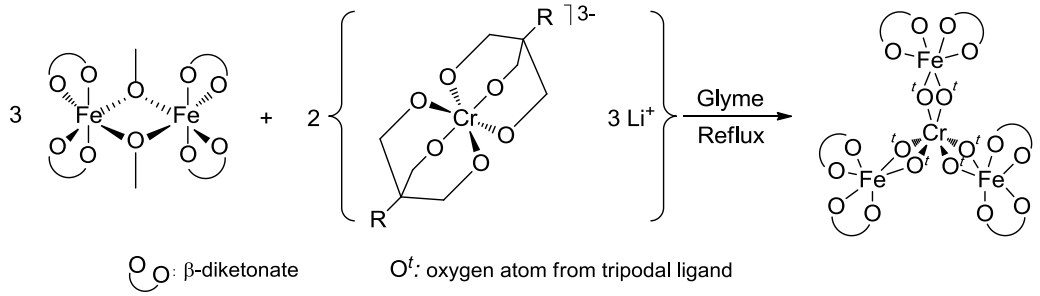

Scheme 2.2: R is referred to Me, Et or Ph.

Reactions were carried out in three steps: namely (**I**) the preparation of the tripodal lithium alkoxide, (**II**) its 2:1 reaction with the chromium(III) starting material to form the Cr^{III} core and (**III**) the combination of this core with the iron(III) preformed dimer, to give the propeller-like M_4 complexes.

Step I

$$H_3L + 3\ n\text{-BuLi} \longrightarrow Li_3L + C_4H_{10}$$

$$CrCl_3 \xrightarrow{\text{thf, Zn}} CrCl_3(thf)_3$$

Step II

$$2\ FeCl_3 + 4\ Hdpm + 6\ MeONa \longrightarrow [Fe_2(\mu\text{-}OMe)_2(dpm)_4] + 4\ MeOH + 6\ NaCl$$

$$CrCl_3(thf)_3 + 2\ Li_3L \longrightarrow \{Li_3\,[CrL_2]^{3-}\} + 3\ LiCl$$

Step III

$$3\ [Fe_2(\mu\text{-}OMe)_2(dpm)_4] + 2\ \{Li_3[CrL_2]\} \xrightarrow[\Delta]{\text{Glyme}} 2\ [Fe_3Cr(L)_2(dpm)_6] + 6\ MeOLi$$

Scheme 2.3

Glyme (1,2-dimethoxyethane) was selected as the reaction solvent because of its chelating ability towards hard metal ions, such as Li^+, in an attempt to stabilise Li^+ bound to the core and prevent polymerisation (Figure 2.2) which could occurs with these Cr-O bonds.

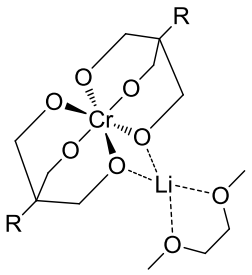

Figure 2.2: Proposed complexation of a lithium cation by the tripodal alkoxide and the solvent. Only one occurrence is shown for clarity.

Referring to the choice of the tripodal ligand the objective, for the first reaction attempts, was focused on a simple tripodal derivative, in order to understand the feasibility of the synthetic proposal and to optimize the three reaction steps. The ligands had to afford a good crystal quality to the product and, at the same time, a proper solubility features to the whole final molecule, in order to facilitate the crystallisation process. As a forward stage, the use of a functionalised tripodal ligand, suitable to bound the complex on a surface, will be investigated. We identified three ligands as appropriate candidates, which were all employed in this thesis work: 2-hydroxymethyl-2-methylpropane-1,3-diol (H_3L^{Me}), 2-Ethyl-2-hydroxymethyl-propane-1,3-diol (H_3L^{Et}), 2-hydroxymethyl-2-phenylpropane-1,3-diol (H_3L^{Ph}).

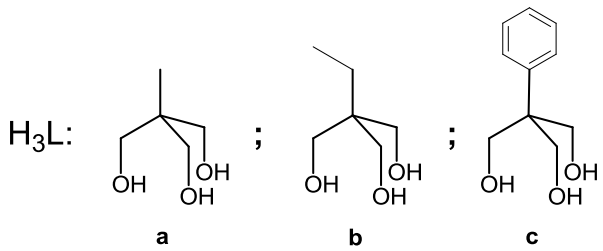

Figure 2.3: Employed tripodal ligands. **a**: H_3L^{Me}; **b**: H_3L^{Et}; **c**: H_3L^{Ph}.

The preparation of such molecules was based on a Tollens condensation,[2] from the relative aldehyde, as showed in Scheme 2.4.

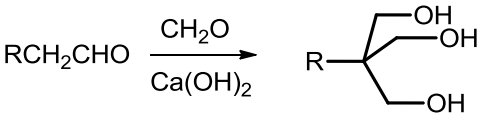

Scheme 2.4: Tollens condensation scheme.

Polyalcohols or their alkoxide derivatives are employed as ligands for d-block ions and reveal the bridging mode of coordination as being far more common in the products than the simple chelating mode.[3–9] This appears to depend less on the experimental metal-to-ligand proportions than on the order and/or rate of addition and naturally on steric constraints imposed by the reactants, including ancillary ligands. Metal coordination numbers, being themselves dependent on ionic or covalent radii, also play their role in determining binding modes.

The preparation of the starting materials (step I) is fundamental for the success of such a strategy. The polymeric nature of the chromium(III) chloride would not allow a reaction with a tridentate ligand, so a conversion into a monomeric chromium complex, as $[CrCl_3(thf)_3]$, is of crucial importance. At the same time, the complete deprotonation of the ligand is mandatory, first, in order to substitute three chloride ions bound on the chromium ion, then, to form the anionic coordination complex $\{CrL_2\}^{3-}$.

Deprotonation of H_3L with *n*-butyllithium was shown to be complete by FTIR analysis of the resulting lithium alkoxides.

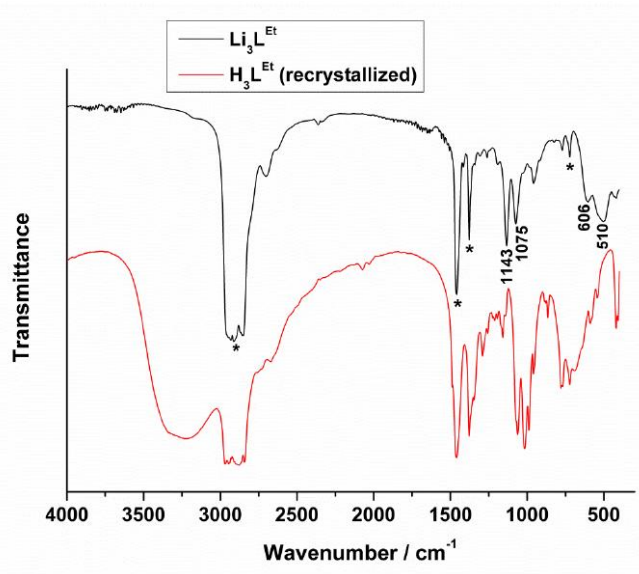

Figure 2.4: Comparison of the FTIR spectra (Nujol mulls) of the tripodal alcohol H_3L^{Et}, red line, and its corresponding lithiated alkoxide, Li_3L^{Et} (black line). Absorption bands for Nujol are marked with asterisks. In the spectrum of the alkoxide, the absence of the broad ν(O-H) band above 3000 cm^{-1} is indicative of full deprotonation of the corresponding alcohol.

Butyllithium was chosen because of its strongly basic character and also because double alkoxides of Li^+, with transition metal ions, present a lower degree of polymerisation when compared to analogues with larger alkali metal cations. As an example, studies by Mehrotra and Singh on a series of alkali metal/titanium(IV) complexes, formulated as $\{M'\{Ti(OPr^i)_5\}\}_n$, M′ = Li^+, Na^+ and K^+, have shown that the degree of polymerisation (n) is determined by the ratio between the ionic radii of the alkali- and transition-metal ions. Lower ratios (<1.4 for Li^+) lead to discrete molecular products with n = 1 or 2, while larger ratios give one- and threedimensional polymeric systems for Na^+ and K^+ respectively.[10] The same tendency was also reported for double alkoxides of vanadium(IV) and Li^+ or K^+.[11,12]

As preliminary starting materials preparation, the iron(III) dimer has to be synthesised,[13] as showed in Scheme 2.3, in order to be used in the last stage, reacting with the chromium core. The complex $[Fe_2(\mu\text{-}OMe)_2(dpm)_4]$ is obtained from anhydrous iron(III) chloride, in excellent yield, employing sodium methoxide, which works as ligand for iron and as base for β-diketone, which is the peripheral ligand for the iron.

The step II described in Scheme 2.3 is the nucleus of the strategy and consists of the addition of $[CrCl_3(thf)_3]$ to the boiling lithium alkoxide suspension. This stage was performed slowly over a period of several hours, to prevent polynuclear aggregation of the desired core product. This was accomplished by slow extraction of the chromium starting material into the alkoxide suspension by the refluxing solvent, in a way that the dissolved Cr^{III} would be added to an excess of the lithium alkoxide.

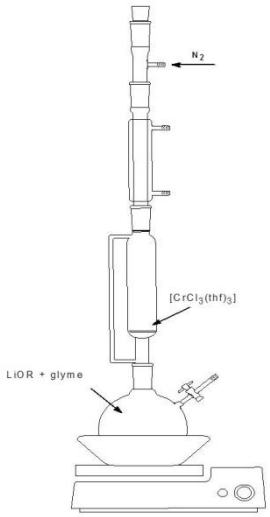

Figure 2.5: Reaction apparatus used for the $CrCl_3(thf)_3$ addition in several hours by a slow extraction of the hot boiling solvent condensed on the filter plate and subsequent leaching of its chromium starting material solution in the ligand flask.

On one occasion, the light green solid $Li_3[CrL_2]$ intermediate was isolated and partially characterised by FTIR.

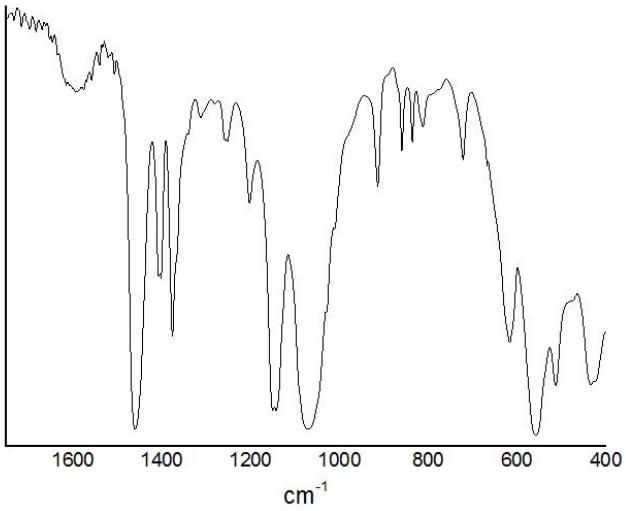

Figure 2.6: FTIR spectrum (range 1750-400 cm^{-1}) of $\{Li_3[Cr(L^{Et})_2]\}$. The low wavelength region is typical for metal-oxygen bonds.

The paramagnetic nature of the Cr(III) ion can be exploited to perform experiments of Electron Paramagnetic Resonance (EPR). The spectrum, shown in Figure 2.7 was recorded on a frozen suspension in 1,2-dimethoxy ethane of a freshly prepared chromium core. It shows a sharp line centred

at g = 1.98, expected for Cr^{3+}, which is in agreement with our hypothesis on a six coordinated chromium intermediate.

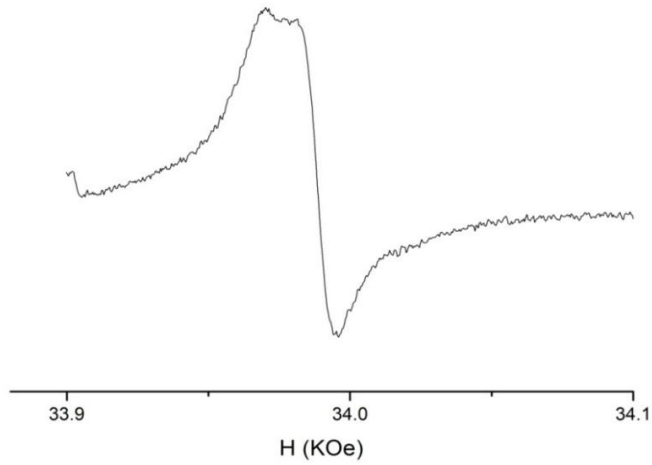

Figure 2.7: W–band (94.35 GHz) EPR spectrum of a frozen suspension sample of $\{Li_3[Cr(L^{Et})_2]\}$ core; it shows low anisotropy and no evidence of zero field splitting.

The high polarity of the product prevented its dissolution in the reaction mixture, so any attempt of isolation or purification of the chromium complex failed. In particular the chromium core solid is very soluble in methanol, but its crystallisation is very difficult; various attempts were tried, especially of vapour diffusion or layer of an ether solvent into the methanol solution. Another tried approach was the filtration of the $\{Li_3[CrL_2]\}$ suspension, concentrate the mother liquor and put it in the freezer for several days. In all cases we obtained just the precipitation of a small amount of salt.

The isolation or the study on the mechanism of this reaction was not one of the objectives of this thesis, so in order to proceed with the synthesis the chromium core suspension was employed in the following reaction step with the iron(III)-β-diketonate dimer, without further treatments as lithium salts are the only reaction by-products forming.

The latter reaction (step III in Scheme 2.3) is conducted with the addition of the greenish chromium core suspension in glyme, to the orange iron dimer suspension in the same solvent, then heating the lot up. When the system reaches about 70°C the solids suspended in the solvent start to dissolve, creating a brown-reddish solution, while some grey salts remain undissolved.

After the reaction of the Cr(III) core with the iron(III) β-diketonate dimer in the suitable proportion, the subsequent crystallisation process depends on the tripodal ligand involved in the reaction. Regarding compounds Fe_3CrL^{Me} and Fe_3CrL^{Et} as soon as the reaction is stopped and cooled down it precipitates as a powder (in the case of Fe_3CrL^{Me}) or a microcrystalline powder (Fe_3CrL^{Et}) together with lithium salts; is then necessary to extract the products with dry hexane and recrystallise them by slow evaporation at RT. For Fe_3CrL^{Me} the crystallisation time, meaning the period in which the hexane solution was allowed to evaporate in a close chamber, was very long, obtaining small crystals after some months. Fe_3CrL^{Ph} behaves in different ways, because it remains in solution once the reaction mixture has been cooled down. After a first filtration to eliminate salts, a concentration of the mother liquor allowed to obtain good quality crystals at -20°C after several days. Alternative crystallisation procedures gave poorer results. As an example, vapour diffusion of methanol into aliquots of the brown-reddish reaction mixture in glyme gave approximately 1:1 mixtures of small, reddish-brown prisms of Fe_3CrL^{Et} or Fe_3CrL^{Ph} together with larger, bright red hexagonal plates. These were investigated by x-ray diffraction and resulted to be the $[Fe_2(\mu\text{-}OMe)_2(dpm)_4]$ starting material.

These results are compatible with the relatively low yields obtained for the three products (ca. 29% Fe_3CrL^{Et}, 23% Fe_3CrL^{Ph}, not even calculated for Fe_3CrL^{Me}), compared to the 54% yield reported for the “one pot” synthesis of the Fe_3Cr/Fe_4 solid solution.[1] This suggests that the equilibrium and/or the rate constants of the hexacoordinated chromium core formation reaction strongly limit the whole reaction yield, as not enough Cr-containing core is formed in step II to react with the iron(III) dimer in step III.

In subsequent repetitions of the synthesis of Fe_3CrL^{Et}, attempts to avoid contamination with LiCl/Li(OMe) by filtering the hot reaction mixture immediately after the third reaction step did not improve the result, as the products crystallised on the sintered glass disk during filtration. The preparation of Fe_3CrL^{Ph}, on the other hand, gave clean crystals straight from the reaction mixture at −20 °C, because of the higher solubility conferred to the product by the phenyl substituent on the tripodal alkoxide. In this case, removal of the LiCl/LiOMe contaminant was carried out at RT before the reaction mixture was cooled down for *ca.* 3–4 weeks.

Elemental analysis data obtained for Fe_3CrL^{Me}, Fe_3CrL^{Et} and $Fe_3CrL^{Ph}\cdot C_4H_{10}O_2$ are well in accordance with the results of single crystal x-ray diffraction, EPR and magnetic studies performed on the products, as described below. Additionally, the fingerprint region (400–1650 cm^{-1}) of the Fourier-transform infrared (FTIR) spectra of Fe_3CrL^{Et} and

$Fe_3CrL^{Ph}\cdot C_4H_{10}O_2$ (Figure 2.8) gives very useful hints on the formation of the Fe_3Cr aggregates and can therefore be employed as a quick and easily accessible diagnostic tool.

Figure 2.8 presents a comparison of these spectra with that of the $[Fe_2(\mu\text{-}OMe)_2(dpm)_4]$ starting material. No Fe_3CrL^{Me} FTIR spectrum was run because of the low yield relative to this derivative. New bands appearing at 1074 (Fe_3CrL^{Et}) and 1094 cm^{-1} ($Fe_3CrL^{Ph}\cdot C_4H_{10}O_2$) and at 594 ($Fe_3CrL^{Et}$) and 591 cm^{-1} ($Fe_3CrL^{Ph}\cdot C_4H_{10}O_2$) can be assigned to $\nu(C\text{–}O_{alkoxide})$ and $\nu(M\text{–}O_{alkoxide})$ absorptions respectively,[14–16] being therefore indicative of the combination of the $\{Cr(L)_2\}^{3-}$ core with the peripheral $\{Fe(dpm)_2\}^{+}$ units, to give the propeller-like assembly. Also, the absorption at 1050 cm^{-1} for the iron(III) dimer, which has been assigned to $\nu(C\text{–}O_{methoxide})$,[13,15] disappears in the spectra of Fe_3CrL^{Et} and $Fe_3CrL^{Ph}\cdot C_4H_{10}O_2$ as the methoxide bridges are replaced with the tripodal alkoxide bridging groups.

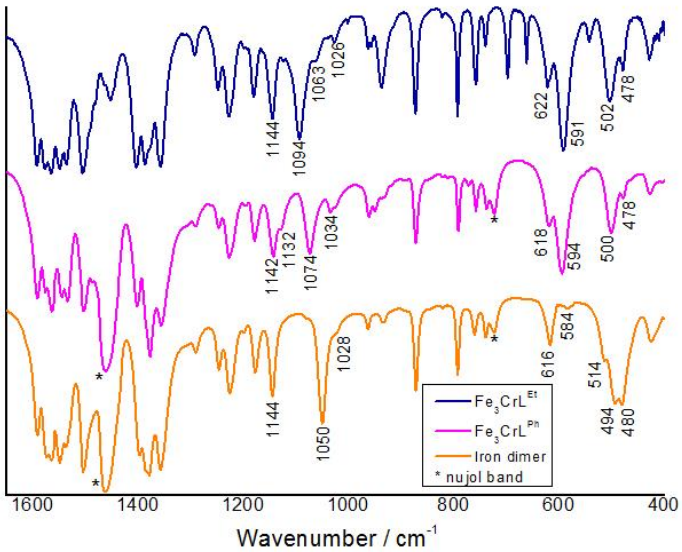

Figure 2.8: FTIR spectra in 1650-400 cm^{-1} of Fe_3CrL^{Et} (blue), Fe_3CrL^{Ph} (pink) and iron dimer (orange).

2.3 Experimental

Syntheses were carried out under N_2 with the use of Schlenk techniques. Solvents (Aldrich) were dried by standard procedures[17] and distilled under N_2 prior to use. Chromium(III) chloride, anhydrous iron(III) chloride and *n*-butyllithium (1.6 M solution in hexanes) were supplied by Aldrich and used without further purification. 2-Hydroxymethyl-2-ethyl-propane-1,3-diol (H_3L^{Et}, Aldrich) was recrystallised from a hot 1:1 mixture of dry thf and toluene, which gave 87% yield of colourless crystals after standing overnight at –20°C. 2-Hydroxymethyl-2-methylpropane-1,3-diol (H_3L^{Me}, Aldrich) was recrystallised from a hot dry 1:1 thf/toluene solution, which gave 69% yield of colourless crystals after standing overnight at –20°C. $[CrCl_3(thf)_3]$,[18] 2-hydroxymethyl-2-phenylpropane-1,3-diol (H_3L^{Ph})[2] and $[Fe_2(\mu\text{-}OMe)_2(dpm)_4]$[19] were prepared in high yields by published methods. H_3L^{Ph} was recrystallised from a 3:1 toluene/thf mixture, with nearly quantitative yield.

2.3.1 Syntheses

$[Fe_3Cr(L^{Et})_2(dpm)_6]$

Step 1 A colourless solution of H_3L^{Et} (300 mg, 2.24 mmol) in 18 ml of thf was cooled to 0°C to receive the dropwise addition of 4.2 ml (6.7 mmol) of a 1.6 M solution of *n*-butyllithium in hexanes. The reaction mixture was stirred for a period of 5h 30min, during which it was allowed to warm up slowly to room temperature (RT). The solid product, Li_3L^{Et} (309 mg, 2.03 mmol, 90.8% yield), was isolated by filtration, dried under vacuum for 1h 30min and then immediately used in the following reaction step. **Step 2** Dry Li_3L^{Et} (2.03 mmol) was suspended in *ca.* 140 mL of 1,2-dimethoxyethane (glyme) and stirred at RT for 30min. A reflux system was then assembled, in which the boiling solvent from this white suspension was employed to continuously extract purple $[CrCl_3(thf)_3]$ (375 mg, 1.00 mmol) into the hot alkoxide suspension over a period of 12h. This produced a light greyish-green suspension that was cooled down to RT. **Step 3** Golden yellow $[Fe_2(\mu\text{-}OMe)_2(dpm)_4]$ (1.36 g, 1.50 mmol) was suspended in 50 ml of glyme and stirred at RT for *ca*. 15min, before receiving the slow addition of the light greyish-green suspension prepared in the previous step. The system was then heated under reflux for 5h, changing into a reddish-brown solution as soon as boiling started, and kept this appearance up to the end of the procedure.

After reflux, the reaction mixture was cooled down overnight to RT, producing 0.58 g of dark reddish-brown crystals mixed with an off-white powder, probably a mixture of LiCl and Li(OMe). Partial solvent removal

from the filtrate (under vacuum) and standing at -20°C for two days produced a second lot of smaller and cleaner dark-coloured crystals (12 mg). The mixture of products (complex Fe_3CrL^{Et} + white solid) was extracted with hexanes (proportion 10 mg:1 ml), which dissolved the dark-coloured crystals but not the white contaminant. Slow evaporation of this solution at RT gave clean rhombohedral prisms of Fe_3CrL^{Et}. Final yield: 464 mg, 0.294 mmol, 29.4%. The product is soluble in hexanes, toluene and benzene; slightly soluble in acetone and insoluble in glyme or more polar solvents. Found for Fe_3CrL^{Et}: C, 59.05; H, 8.70; Cr, 3.32; Fe, 10.71 %. Calc. for $C_{78}H_{136}O_{18}CrFe_3$: C, 59.24; H, 8.67; Cr, 3.29; Fe, 10.59 %. Fe:Cr = 3.00 (mol/mol).

$[Fe_3Cr(L^{Ph})_2(dpm)_6]\cdot C_4H_{10}O_2$ ($2\cdot C_4H_{10}O_2$)

The experimental procedure conducted was the same as above, employing 290 mg (1.59 mmol) of H_3L^{Ph}, 4.77 mmol of *n*-butyllithium, 210 mg (0.560 mmol) of $[CrCl_3(thf)_3]$ and 0.820 g (0.904 mmol) of $[Fe_2(\mu\text{-}OMe)_2(dpm)_4]$. In this case, compound $Fe_3CrL^{Ph}\cdot C_4H_{10}O_2$ was obtained as pure single-crystals (110 mg) after the reaction mixture was first filtered to eliminate LiCl/Li(OMe) (this by-product did not contaminate the crystals) and then cooled down to -20°C for several weeks. Two additional batches (70 mg) of crystals were isolated by filtration after consecutive steps of partial solvent evaporation from the mother liquor. The reaction mixture was finally taken to dryness under vacuum and the remaining solid (*ca.* 1 g) was dissolved in glyme (80 ml), filtered through Celite to eliminate a small amount of a fine residue, concentrated to about half volume and placed in a closed chamber with MeOH for vapour diffusion over a period of four weeks. Formation of a significant amount of bright red plates of the $[Fe_2(\mu\text{-}OMe)_2(dpm)_4]$ starting material was observed (0.283 g), together with deep brown-reddish prisms of $Fe_3CrL^{Ph}\cdot C_4H_{10}O_2$ (45 mg). Total yield: 225 mg, 0.127 mmol, 22.7 %. Compound $Fe_3CrL^{Ph}\cdot C_4H_{10}O_2$ is soluble in non-polar organic solvents, even more than Fe_3CrL^{Et}. Found for $Fe_3CrL^{Ph}\cdot C_4H_{10}O_2$: C, 60.46; H, 8.25; Cr, 2.87; Fe, 9.64 %. Calc. for $C_{90}H_{146}O_{20}CrFe_3$: C, 61.15; H, 8.33; Cr, 2.94; Fe, 9.48 %. Fe:Cr = 3.13 mol/mol.

$[Fe_3Cr(L^{Me})_2(dpm)_6]$

The same experimental procedure was used as for Fe_3CrL^{Et} and Fe_3CrL^{Ph}, employing 2.50 mmol of H_3L^{Me}, 7.50 mmol of *n*-butyllithium, 1.249 mmol of $[CrCl_3(thf)_3]$ and 1.875 mmol of $[Fe_2(\mu\text{-}OMe)_2(dpm)_4]$. After the whole procedure the reaction mixture was filtered to eliminate lithium salts as soon as the preparation was stopped and then taken to dryness completely. Aliquots (about 100 mg) of the obtained brown orange solid were dissolved in 20 ml of dry hexane. The solutions were filtered in order to remove a certain amount of orange solid (probably iron dimer) and then were left evaporating slowly. Small dark brown hexagonal prism crystals of Fe_3CrL^{Me} were obtained after various weeks in a very low yield. All the other attempts to crystallise the product were unsuccessful (at -20°C directly from the reaction mixture or by vapour diffusion of methanol into glyme solution), producing an amorphous powder or, at the best, a microcrystalline powder. The total yield was impossible to calculate because the preparation produced only few small crystals. Found for Fe_3CrL^{Me}: C, 58.65; H, 8.54; Cr, 3.31; Fe, 10.76 %. Calc. for $C_{76}H_{132}O_{18}CrFe_3$: C, 58.76; H, 8.57; Cr, 3.35; Fe, 10.79 %. Fe:Cr = 3.03 mol/mol.

All Fe_3Cr products (Fe_3CrL^{Et} and $Fe_3CrL^{Ph}\cdot C_4H_{10}O_2$ and Fe_3CrL^{Me}) are air-stable in solid state, while their brown-reddish solutions suffer from very slow decomposition in air, as revealed by the ^{1}H-NMR analyses described below. This decomposition is possibly due to a hydrolytic process involving the alkoxide ligand.

2.4 Characterisations

Fe_3CrL^{Me} was employed for magnetic and EPR investigation, after the resolution of its crystallographic structure, since an accurate measure of its trigonal anisotropy was possible. For these kinds of investigations only a single Fe_3CrL^{Me} crystal was used. Other characterisations were not possible because of the low achievable yield of this specific compound.

Fe_3CrL^{Et} and Fe_3CrL^{Ph} were involved in an usual characterisation procedure, in order to explore features of such cluster.

2.4.1 Single-crystal x-ray diffraction analyses

Data for Fe_3CrL^{Et} and $Fe_3CrL^{Ph}\cdot C_4H_{10}O_2$ were collected at RT on a Bruker Kappa X8 APEX II CCD diffractometer with graphite monochromatised Mo-K_α (λ = 0.71073 Å) radiation. Reddish-brown crystals of Fe_3CrL^{Et} and $Fe_3CrL^{Ph}\cdot C_4H_{10}O_2$ (0.443 x 0.371 x 0.196 mm and 0.554 x 0.207 x 0.128 mm respectively) were mounted on glass fibres. X-PREP was used to perform the Gaussian absorption correction based on indexed crystal faces. Cell dimensions were based on all 1459 and 6747 observed reflections ($I>2\sigma_I$) for Fe_3CrL^{Et} and $Fe_3CrL^{Ph}\cdot C_4H_{10}O_2$, respectively. Structure resolution (by direct methods), and refinement (by full-matrix least-squares on F^2), were carried out with SHELXS-97[20] and SHELXL-97[21] respectively. Refinements employed anisotropic displacement parameters for all non-hydrogen atoms, while H atoms were included in calculated positions with constrained thermal parameters.

In the case of complex $Fe_3CrL^{Ph}\cdot C_4H_{10}O_2$, additional electron density was located in four cavities of approximately 360 $Å^3$ and with *ca.* 45 electrons each, which were taken as the total potential solvent accessible volume. This corresponds to four molecules of 1,2-dimethoxyethane per unit cell, a result confirmed by ^{1}H-NMR as shown below. This residual electron density, which was included in the molecular formula of $Fe_3CrL^{Ph}\cdot C_4H_{10}O_2$ in Table 2.1, has been treated with the SQUEEZE routine in PLATON.[22,23]

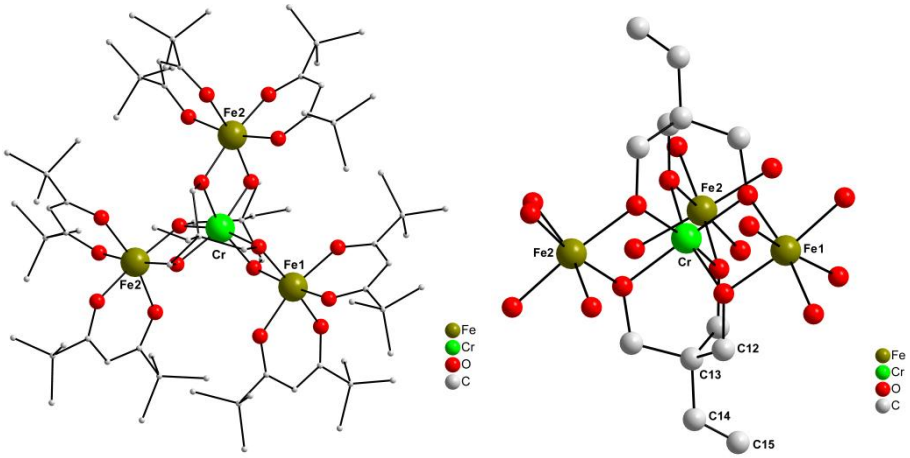

Figure 2.9: Representations of the molecular structure of $[Fe_3Cr(L^{Et})_2(dpm)_6]$. Left: view of the complete molecule. Right: emphasis on the coordination spheres of the metal centres (C and H atoms of the β-diketonate ligands not shown). Carbon C15 is equally disordered over three equivalent positions about the C_3 axis.

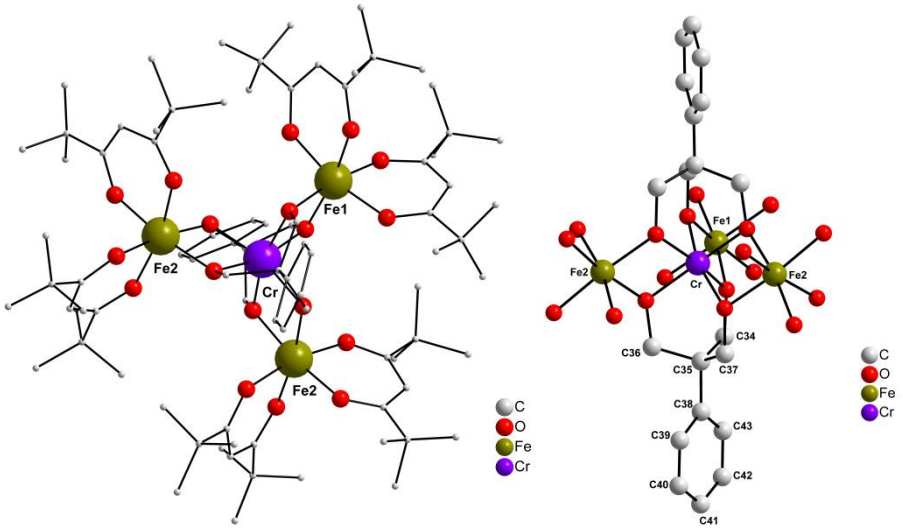

Figure 2.10: Representations of the molecular structure of $[Fe_3Cr(L^{Ph})_2(dpm)_6]$ Left: view of the complete molecule. Right: emphasis on the coordination spheres of the metal centres and on the binding of the tripodal alkoxide.

Although apparently well formed, with readily distinguishable faces and angles, crystals of both products diffract weakly. In the tripodal alkoxide ligand of Fe_3CrL^{Et}, C(15) was found to be disordered (occupation factor 0.333) over equivalent positions about the C_3 axis. Additionally, for both complexes some of the carbon thermal ellipsoids in the β-diketonate ligands Fe_3CrL^{Et} are considerably elongated [C(8), C(9) and C(10) for and C(9),

C(10), C(11), C(20), C(32) and C(44) for $Fe_3CrL^{Ph}{\cdot}C_4H_{10}O_2$], a common occurrence for this type of ligand, particularly considering that data collection was carried out at 293(2) K.

Crystals of Fe_3CrL^{Et} and $Fe_3CrL^{Ph}{\cdot}C_4H_{10}O_2$ are optically anisotropic (pleochroic), changing from brown-reddish to green when viewed from different directions. Table 2.1 presents crystallographic and refinement data for both products, while Table 2.2 contains selected structural information. Figure 2.9 and Figure 2.10 represent the molecular structures of the two complexes.

	Fe_3CrL^{Et}	$Fe_3CrL^{Ph}{\cdot}C_4H_{10}O_2$
Empirical formula	C_{78} H_{136} Cr Fe_3 O_{18}	C_{90} H_{146} Cr Fe_3 O_{20}
Formula weight / g mol^{-1}	1581.42	1767.62
Temperature / K	293(2)	293(2)
Crystal system	Trigonal	Monoclinic
Space group	*R*-3*c*:*h* (No. 167:h)	*C*2/*c* (No. 15)
a / Å	16.4250(5)	19.6204(7)
b / Å	16.4250(5)	22.0622(7)
c / Å	58.768(3)	24.7198(9)
α / °	90	90
β / °	90	107.964(2)
γ / °	120	90
V / $Å^3$	13730.5(8)	10178.8(6)
F(000)	5100	3792
Z	6	4
ρ_{calcd} / Mg m^{-3}	1.148	1.153
μ / mm^{-1}	0.639	0.583
θ range / °	1.59 to 26.82	1.73 to 26.80
Reflections collected	56495	73182
Independent reflections	3222 [R(int) = 0.0737]	10712 [R(int) = 0.0499]
Reflections with $I > 2\sigma_I$	1459	6747
Parameters refined	154	488
Completeness to θ_{max} /%	98.2	99.3
Goodness-of-fit on F^2	1.020	1.054
R_1, wR_2 ($I > 2\sigma_I$)[a]	R_1 = 0.0660, wR_2 = 0.1704	R_1 = 0.0665, wR_2 = 0.1958
R_1, wR_2 (all data)[a]	R_1 = 0.1411, wR_2 = 0.2245	R_1 = 0.1047, wR_2 = 0.2188
Largest diff peak / hole (e/$Å^3$)	0.281 and -0.177	0.770 and -0.463

Table 2.1: Crystal and structure refinement data for [$Fe_3Cr(L^{Et})_2(dpm)_6$] and [$Fe_3Cr(L^{Ph})_2(dpm)_6$]

[a] As defined by the SHELXL-97 program.[20]

Fe_3CrL^{Et} crystallises in the relatively high symmetry, trigonal $R\bar{3}c$ space group, similarly to the homometallic complex [$Fe_4(L^{Me})_2(dpm)_6$] (Fe_4L^{Me}).[19] Therefore, it presents D_3 crystallographic symmetry and the carbon atom C(15) of the ethyl substituent is disordered over three equivalent, 0.333-occupancy positions related by the C_3 axis. Product $Fe_3CrL^{Ph}{\cdot}C_4H_{10}O_2$ crystallises in the same space group (*C2/c*) as the Fe_3CrL^{Ph} compounds reported earlier,[1] but without contamination by the homometallic complex – as confirmed by elemental, spectroscopic and magnetic analyses – and with

glyme rather than diethyl ether as the crystallisation solvent. This molecule has C_2 symmetry, with the twofold axis lying along the Cr···Fe(1) direction.

Bond Lengths / Å	Fe_3CrL^{Et}		Fe_3CrL^{Ph}	
$M_{central}\cdots M_{peripheral}$	Cr···Fe	3.023	Cr···Fe	3.021
$M_{peripheral}\cdots M_{peripheral}$	Fe···Fe	5.237	Fe···Fe	5.232
$M_{central}–O_{tripodal}$	Cr–O(3)	1.949(3)	Cr–O(7)/O(9)	1.953(2)
			Cr–O(8)	1.951(2)
$M_{peripheral}–O_{tripodal}$	Fe–O(3)	1.963(3)	Fe(1)–O(8)	1.977(2)
			Fe(2)–O(7)	1.975(2)
			Fe(2)–O(9)	1.983(2)
$M_{peripheral}–O_{diketonate}$	Fe–O(1)	1.996(3)	Fe(1)–O(1)	1.999(3)
			Fe(1)–O(2)	2.014(2)
	Fe–O(2)	1.986(4)	Fe(2)–O(3)	1.991(2)
			Fe(2)–O(4)	2.001(3)
			Fe(2)–O(5)	1.996(3)
			Fe(2)–O(6)	1.986(2)
Bond Angles / º	Fe_3CrL^{Et}		Fe_3CrL^{Ph}	
$M_{peripheral}\cdot\cdot M_{central}\cdot\cdot M_{peripheral}$	Fe···Cr···Fe	120.00	Fe(1)···Cr···Fe(2)	119.40
			Fe(2)···Cr···Fe(2)	121.21
$M_{peripheral}\cdots M_{peripheral}\cdots$ $M_{peripheral}$	Fe···Fe···Fe	60.00	Fe(1)···Fe(2)···Fe(2)	59.67
			Fe(2)···Fe(1)···Fe(2)	60.66
$O_{tripodal}–M_{central}–O_{tripodal}$	O(3)#1-Cr-O(3)#3	90.80(11)	O(8)-Cr-O(7)	89.81(9)
			O(8)#1-Cr-O(9)	89.91(9)
			O(7)#1-Cr-O(9)	90.89(9)
	O(3)#1-Cr-O(3)	79.13(17)	O(7)-Cr-O(9)	80.16(9)
			O(8)#1-Cr-O(8)	80.21(14)
	O(3)#1-Cr-O(3)#4	101.46(17)	O(8)-Cr-O(9)	101.02(1)
			O(7)-Cr-O(7)#1	102.28(13)
	O(3)#1-Cr-O(3)#5	164.14(18)	O(8)-Cr-O(7)#1	164.37(9)
			O(9)-Cr-O(9)#1	165.77(13)
$M_{central}–O_{tripodal}–M_{peripheral}$	Cr–O(3)–Fe	101.20(12)	Cr-O(8)-Fe(1)	100.41(11)
			Cr-O(7)-Fe(2)	100.62(10)
			Cr-O(9)-Fe(2)	100.31(10)
$O_{tripodal}–M_{peripheral}–O_{diketonate}$	O(3)–Fe–O(1)#1	93.50(13)	O(8)-Fe(1)-O(1)#1	94.14(10)
			O(7)-Fe(2)-O(4)	93.29(10)
	O(3)–Fe–O(2)#1	170.93(14)	O(8)-Fe(1)-O(1)	170.44(11)
			O(7)-Fe(2)-O(5)	170.46(10)
			O(9)-Fe(2)-O(4)	171.69(10)
	O(3)–Fe–O(1)	97.36(14)	O(8)-Fe(1)-O(2)#1	99.83(10)
			O(7)-Fe(2)-O(3)	97.90(10)
			O(9)-Fe(2)-O(6)	96.98(10)
	O(3)–Fe–O(2)	92.58(13)	O(8)#1-Fe(1)-O(2)#1	89.93(10)
			O(7)-Fe(2)-O(6)	91.98(9)
			O(9)-Fe(2)-O(3)	92.41(9)
			O(9)-Fe(2)-O(5)	92.10(10)
$O_{tripodal}–M_{peripheral}–O_{tripodal}$	O(3)#1–Fe–O(3)	78.46(16)	O(8)-Fe(1)-O(8)#1	78.96(13)
			O(7)-Fe(2)-O(9)	78.91(9)
$O_{diketonate}–M_{peripheral}–O_{diketonate}$	O(2)#1-Fe-O(1)	84.47(15)	O(1)-Fe(1)-O(2)	84.68(10)
			O(3)-Fe(2)-O(5)	85.52(10)
			O(3)-Fe(2)-O(4)	85.80(10)
			O(6)-Fe(2)-O(5)	85.92(10)
	O(2)#1-Fe-O(1)#1	86.19(15)	O(1)-Fe(1)-O(2)#1	86.68(11)
			O(6)-Fe(2)-O(4)	86.04(11)
	O(2)#1-Fe-O(2)	96.4(2)	O(1)-Fe(1)-O(1)#1	93.43(16)
			O(5)-Fe(2)-O(4)	95.84(11)
	O(1)Fe–O(1)#1	166.0(2)	O(2)#1-Fe(1)-O(2)	167.39(14)
			O(6)-Fe(2)-O(3)	167.52(10)

Table 2.2: Selected bond lengths (Å) and angles (deg) for $[Fe_3Cr(L^{Et})_2(dpm)_6]$ and $[Fe_3Cr(L^{Ph})_2(dpm)_6]$.

Table 2.3 compares corresponding molecular dimensions for Fe_3CrL^{Et}, Fe_3CrL^{Ph} and four different propeller-like complexes reported in the literature. The two heterometal complexes Fe_3CrL^{Ph} [1] (one pot synthesis) and $[Fe_3Cr(L'')_2(dpm)_6]$ (Fe_3CrL'') are isostructural with Fe_3CrL^{Et} and Fe_3CrL^{Ph} (H_3L'' = 11-(acetylthio)-2,2-bis-(hydroxymethyl)undecan-1-ol).[1,24] The third compound, $[Cr_4(L^{Et})_2(2,2'\text{-bipy})_3Cl_6]$ (Cr_4Et) is a tetrachromium(III) species with three distinct ligands (2,2′-bipyridine, chloride and alkoxide) bound to each of the peripheral metal centres.[25] Despite this diversity, the tripodal alkoxide in complex Fe_3CrL^{Et} and in Cr_4L^{Et} is the same (L^{Et}), so that a comparable geometry is expected for their central cores. Notice that both Fe_3CrPh and Fe_3CrL'' contain *ca.* 16% of Fe_4 species and their molecular dimensions are weighted averages over the two different cores. Data in Table 2.3 clearly show that most bonding and nonbonding distances about the metal ions are smaller in Fe_3CrL^{Et} and $Fe_3CrL^{Ph}\cdot C_4H_{10}O_2$ than in Fe_3CrL^{Ph} (one pot synthesis) and Fe_3CrL'', and close to the values found in Cr_4L^{Et}. This is consistent with the smaller ionic radius of six-coordinate chromium(III) as compared to iron(III)[26] and therefore with the exclusive presence of Cr-centred species in the new products. This is even more significant when one considers the higher temperature of data collection for Fe_3CrL^{Et} and $Fe_3CrL^{Ph}\cdot C_4H_{10}O_2$ (293 K, Table 2.1), which could lead to slightly longer bonds. When the comparison is extended to include the Fe_4L^{Me} complex, which crystallises in the same space group as product Fe_3CrL^{Et},[19,27] the trend in bond lengths involving the central metal ion becomes even more visible. Also, the average helical pitch angle between the plane of the metal ions and the propeller “blades” (the planes formed by the $M_{central}(O)_2M_{peripheral}$ units) is in the range reported for Cr-centred complexes (60–64.5°),[1,24–28] and is significantly smaller than for Fe_4L^{Me} and analogues.[19,27,29]

Bonding and non-bonding distances / Å		**Fe_3CrL^{Et} (293K)**	**Fe_3CrL^{Ph} $\cdot C_4H_{10}O_2$ (293K)**	**Fe_3CrL'' (120K)** [24] (a)	**Fe_3CrL^{Ph} (120K) one pot** [1]	**Cr_4L^{Et} (100 K)** [25] (b)	**Fe_4L^{Me} (100 K)** [19]
$M_{central}$–$O_{tripodal}$		Cr–O(3)	$Cr–O^t$ (av)	$Cr–O^t$ (av)	$Cr–O^t$ (av)	Cr(1)–O^t (av)	Fe(1)–O(1)
		1.949(3)	1.952(2)	1.958(3)	1.9634(14)	1.954(3)	1.9810(12)
$M_{peripheral}$–$O_{tripodal}$		Fe–O(3)	$Fe–O^t$ (av)	$Fe–O^t$ (av)	$Fe–O^t$ (av)	$Cr_{peripheral}$–O^t (av)	Fe(2)–O(1)
		1.963(3)	1.978(2)	1.979(2)	1.9835(14)	1.973(3)	1.9639(12)
$M_{peripheral}$–$O_{diketonate}$		$Fe–O^{dk}$ (av)	$Fe–O^{dk}$ (av)	$Fe–O^{dk}$ (av)	$Fe–O^{dk}$ (av)	------	$Fe(2)–O^{dk}$ (av)
		1.996(3)	1.998(3)	2.001(2)	2.0051(15)	------	1.9993(13)
$M_{central}\cdots C_{central}$ (c)		Cr···C(13) (av	Cr···C(35)	Cr···C(4)	Cr···C(13)	Cr···C(4)/C(10) (av)	Fe···C(2) (av)
		2.986	3.015	3.004	3.027	2.951	3.026
$M_{central}\cdots M_{peripheral}$		Cr···Fe	Cr···Fe (av)	Cr···Fe (av)	Cr···Fe (av)	$Cr(1)\cdots Cr_{peripheral}$ (av)	Fe(1)···Fe(2)
		3.023	3.021	3.012	3.043	3.039	3.086
$M_{peripheral}\cdots M_{peripheral}$		Fe···Fe	Fe···Fe (av)	Fe···Fe (av)	Fe···Fe (av)	$Cr_{peripheral}\cdots Cr_{peripheral}$ (av)	Fe(2)···Fe(2′)
		5.237	5.232	5.216	5.324	5.262	5.345
Helical pitch angle (d)/°		63.4	63.3	62.2	64.4	60.2	70.8
Space group		*R*-3*c* (Trigonal)	*C*2/*c* *(monoclinic)*	*C*2/*c* (Monoclinic)	*C*2/*c* (Monoclinic)	*P*-1 (Triclinic)	*R*-3*c* (Trigonal)

Table 2.3: Abbreviations: av = average; O^t = oxygen atom from the tripodal ligand; O^{dk} = oxygen atom from the β-diketonate. [a]$[Fe_3Cr(L'')_2(dpm)_6]$ with H_3L''=11-(acetylthio)-2,2-bis-(hydroxymethyl)-undecan-1-ol. [b]$[Cr_4(L^{Et})_2(2,2'\text{-bipy})_3Cl_6]$. [c]$C_{central}$ = central carbon atom in the tripodal alkoxide ligand, $[R\underline{C}(CH_2O)_3]^{3-}$. [d]Average dihedral angle between the planes defined by the $M_{central}(O)_2M_{peripheral}$ units and the four metal ions.

2.4.2 ^{1}H-NMR analyses

^{1}H NMR spectra (400.13 MHz) were acquired at 303 K on a Bruker AVANCE 400 NMR spectrometer operating at 9.4 T and equipped with a 5-mm multinuclear direct detection probe. C_6D_6, supplied by Cambridge Isotope Laboratories (CIL), was degassed by the freeze-pump-thaw technique[17] and stored under N_2 over 4A molecular sieves.

Important and definitive structural information can be retrieved from ^{1}H-NMR, which can confirm the actual formation of the desired molecule and the chemical purity of the product. It is of great interest, for such complexes, the possibility to investigate the chemical robustness in solution by periodically running an ^{1}H-NMR spectrum, of the same sample, in an interval of some weeks. We can follow the stability of the molecule to the air, preparing the sample tube and then sealed it in order to be measured in time.

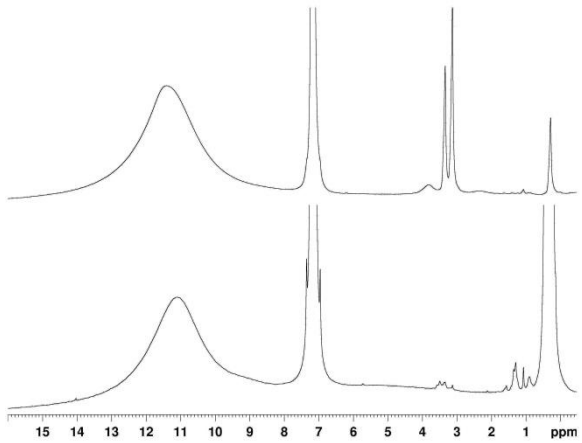

Figure 2.11: ^{1}H-NMR spectra (400.13 MHz) recorded from freshly prepared C_6D_6 solutions of Fe_3CrL^{Et} (bottom, *ca.* 2.5 mmol l^{-1}) and $Fe_3CrL^{Ph}\cdot C_4H_{10}O_2$ (top, 8.1 mmol l^{-1}) at 303K.

Figure 2.11 compares the ^{1}H-NMR spectra of Fe_3CrL^{Et} and $Fe_3CrL^{Ph}\cdot C_4H_{10}O_2$ (while a spectrum for Fe_3CrL^{Me} was not measured because of the small amount of product obtained) recorded in C_6D_6 solutions at 303 K in the chemical shift range from −0.5 to 16 ppm. The main, broad resonance peaks at 11.13 and 11.34 ppm for Fe_3CrL^{Et} and $Fe_3CrL^{Ph}\cdot C_4H_{10}O_2$ respectively are given by the tert-butyl hydrogen atoms of the dpm ligands bound to the peripheral iron(III) centres, in accordance with earlier reports.[1,30] These chemical shifts are lower than for the same hydrogen nuclei in $[Fe(dpm)_3]$ (12.9 ppm at 295 K in $CDCl_3$ solution)[30] because of the existing antiferromagnetic interaction between the central and peripheral metal ions in this family of tetranuclear complexes, which

decreases the unpaired spin density delocalised onto the ligand orbitals.[1,31] The Bu^t hydrogen atoms of chromium(III)-bound dpm are characterised by a much lower Larmor frequency (2.5 ppm for $[Cr(dpm)_3]$, for example), so the observed position of this resonance in the ^{1}H-NMR spectra of Fe_3Cr complexes has been interpreted as strong evidence in favour of a Cr-centred molecular structure.

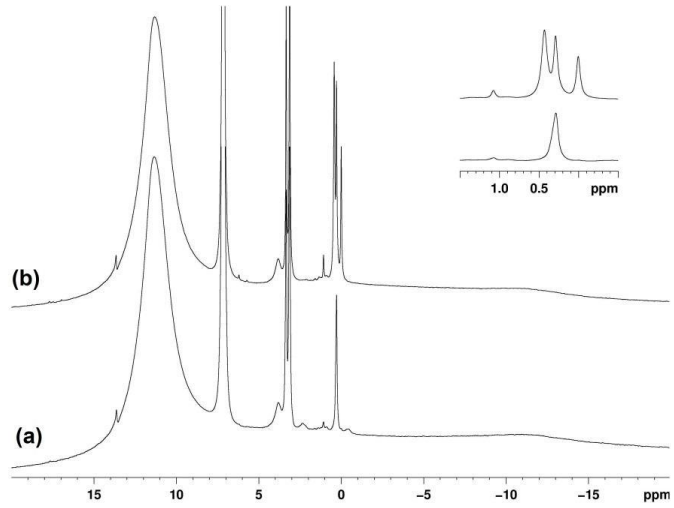

Figure 2.12: ^{1}H-NMR spectra (400.13 MHz; C_6D_6) of Fe_3CrL^{Ph} at 303K. (a) Freshly prepared sample; (b) after 8 days at room temperature. The addition of tetramethylsilane (tms, δ = 0.0 ppm) to the sample was carried out after recording spectrum (a). Inset: Low frequency region, evidencing the peaks at 1.07 (free Hdpm) and 0.44 ppm (possibly water). Note the very broad signal at *ca.* -11.5 ppm, given by the methine resonance in Fe(III)-bound dpm. The peak at *ca.* 13.7 ppm is a quadrature detection artefact at the centre of the large spectral window employed in these experiments (+60 to –40 ppm).

The methine hydrogen from each β-diketonate, in turn, is observed as a very broad and weak resonance at −11.0 and−11.5 ppm for Fe_3CrL^{Et} and $Fe_3CrL^{Ph}{\cdot}C_4H_{10}O_2$ respectively (Figure 2.12 and Figure 2.13), while the weak and broad peak at 3.80 ppm in the spectrum of $Fe_3CrL^{Ph}{\cdot}C_4H_{10}O_2$ has been attributed[1] to one of three types of aromatic hydrogen atoms in the tripodal alkoxide, $(L^{Ph})^{3-}$.

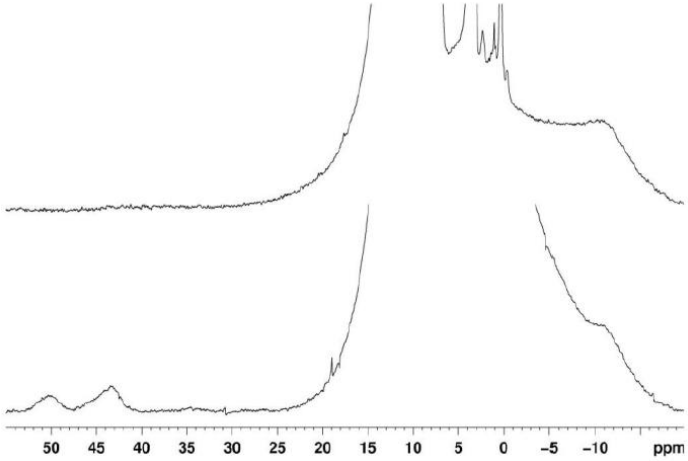

Figure 2.13: Vertical expansion of the ^{1}H-NMR spectra (400.13 MHz; C_6D_6) of complexes Fe_3CrL^{Et} (bottom) and Fe_3CrL^{Ph} (top) at 303K, emphasizing the low intensity, broad peaks tentatively assigned to the alkyl protons of the tripodal alkoxide in Fe_3CrL^{Ph}, $[C\underline{H}_3C\underline{H}_2C(CH_2O)_3]^{3-}$ (43.2 and 50.3 ppm respectively), and to the methine hydrogen of dpm in both complexes [-11.0 (shoulder) and -11.5 ppm for Fe_3CrL^{Et} and Fe_3CrL^{Ph} respectively].

The other phenyl hydrogens could not be located. In the case of Fe_3CrL^{Et}, two broad peaks at 43.2 and 50.3 ppm with a reasonable 3:2 area proportion were tentatively assigned to the alkyl protons of $(L^{Et})^{3-}$, $[C\underline{H}_3C\underline{H}_2C(CH_2O)_3]^{3-}$ (Figure 2.13). Also in Figure 2.12, the low frequency resonance at 0.29 ppm is due to methyl groups of the silicone grease employed in the Schlenk-type glassware. Signals between 0.8 and 3.7 ppm in the spectrum of Fe_3CrL^{Et} are due to solvent impurities, apart from the sharp peak at 1.07 ppm that comes from trace amounts of free Hdpm (Bu^t hydrogens). Finally, the peaks detected at 3.12 and 3.33 ppm in the spectrum of $Fe_3CrL^{Ph}\cdot C_4H_{10}O_2$ were attributed respectively to the $C\underline{H}_3O$– and –$C\underline{H}_2O$– groups of glyme, which occurs as the crystallisation solvent. Integration of the peaks at 11.34 ppm and in the range of 3.1–3.4 ppm gave a 1:1 proportion of glyme to the tetranuclear product, in accordance with x-ray data.

Stability studies were carried out for both Fe_3CrL^{Et} and $Fe_3CrL^{Ph}\cdot C_4H_{10}O_2$ in C_6D_6 solutions kept in capped tubes at RT for two weeks. Samples were analysed shortly after preparation and also after 4, 8 and 15 days, with no sign of precipitation. Spectral changes were very small and slow (Figure 2.12), probably because of the chemical inertness imparted to the products by the presence of chromium(III). The most visible occurrences were the small increase in intensity of the Bu^t peak of free Hdpm, together with the emergence (and gradual growth) of a peak at 0.44

ppm that could be assigned to traces of water absorbed from the atmosphere. This low frequency peak did not correlate to any ^{13}C resonance in a HMBC (Heteronuclear Multiple Bond Correlation, not reported) experiment carried out for the “aged” C_6D_6 solution of complex $Fe_3CrL^{Ph}\cdot C_4H_{10}O_2$ (10 days after preparation).

2.4.3 Magnetic properties of Fe_3Cr propellers

Variable temperature DC magnetic measurements were performed with a Quantum Design MPMS SQUID magnetometer on crystalline samples of $[Fe_3Cr(L^{Et})_2(dpm)_6]$ and $[Fe_3Cr(L^{Ph})_2(dpm)_6]\cdot C_4H_{10}O_2$ (11.1 and 17.0 mg respectively), at temperatures ranging from 1.8 to 300 K and with an applied field H = 1 kOe (up to 25 K) or 10 kOe (at and above 25 K). Samples were ground and pressed in pellets to avoid orientation effects. Diamagnetic corrections of -903 and -1150 (x 10^{-6} emu mol^{-1}), estimated from Pascal's constants,[32,33] were employed for Fe_3CrL^{Et} and $Fe_3CrL^{Ph}\cdot C_4H_{10}O_2$, respectively. Isothermal magnetisation *vs.* H curves were registered up to 50 kOe at 1.9, 2.5 and 4.5 K using the same equipment. AC susceptibility was measured on microcrystalline powder samples from 1.8 to 8.0 K. An Oxford Instruments MAGLAB2000 platform equipped with a laboratory-developed inductance probe was used for Fe_3CrL^{Et} in the frequency range from 0.1 to 70 kHz. Measurements on $Fe_3CrL^{Ph}\cdot C_4H_{10}O_2$ were carried out in the range 0.01 – 10 kHz with a Quantum Design PPMS.

The magnetic properties of the family of propeller-like tetrairon(III) clusters have been widely investigated and found to be dominated by the antiferromagnetic interaction between the central and the peripheral metal ions, which stabilizes a ferrimagnetic spin arrangement of the ground state characterised by a spin value S = 5. Previous investigations of the magnetic properties of solid solutions of Fe_3Cr and Fe_4 clusters were carried out by deconvoluting the contributions of the two species.[1,24] Thanks to the synthetic route previously described, it has been possible to investigate here pure Fe_3Cr propellers. Moreover, as the magnetic properties are strongly influenced by the way the metal ions are connected and the overall topology, we will show in the following that our detailed magnetic investigation confirms the exclusive formation of the Fe_3Cr species through this novel synthetic route.

The temperature dependence of the product of the molar magnetic susceptibility with temperature, χT, where χ is assumed to equal the M/H ratio, was measured over a wide temperature range, 2-300 K, and the results are reported in Figure 2.14 for Fe_3CrL^{Et}.

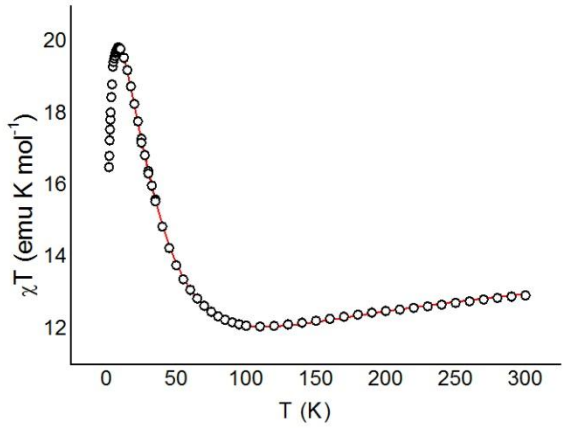

Figure 2.14: Temperature dependence of the molar magnetic susceptibility multiplied by temperature for Fe_3CrL^{Et}. The solid line represents calculated values (see text).

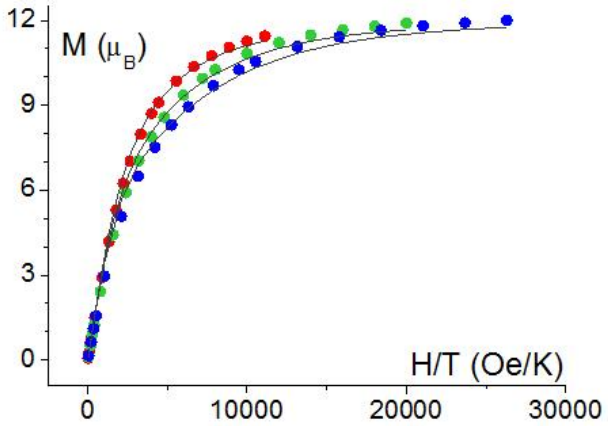

Figure 2.15: Field dependence of the molar magnetisation of Fe_3CrL^{Et} at 1.9 (blue), 2.5 (green) and 4.5 K (red) versus the rescaled variable *H/T*. The lines are calculated values assuming axial anisotropy of the ground *S*=6 state.

The room temperature value, 12.93 emu K mol^{-1}, is slightly smaller than the expected value for three uncorrelated S = 5/2 and one S = 3/2 spins with g = 2, *ca.* 15 emu K mol^{-1}, decreases smoothly on lowering the temperature to reach the minimum of 12.07 emu K mol^{-1} at 110 K and increases for lower temperatures to reach 19.84 emu K mol^{-1} at 9 K. At very low temperature a drastic decrease is observed and will be discussed later. Very similar behaviour is observed for $Fe_3CrL^{Ph}\cdot C_4H_{10}O_2$ and the data are shown in Figure 2.16.

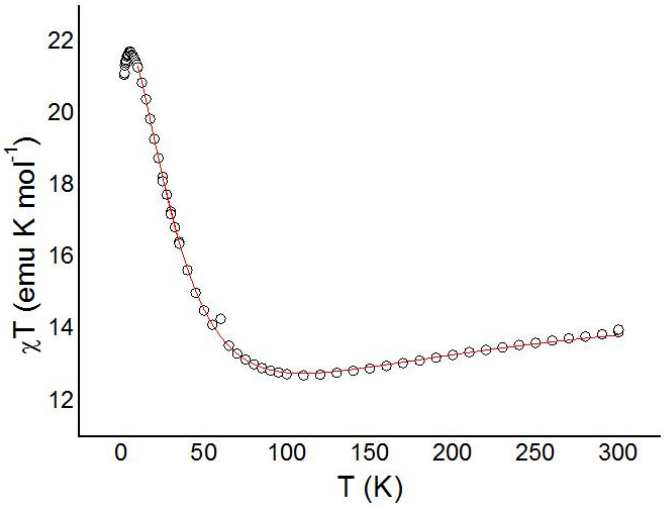

Figure 2.16: Temperature dependence of the molar magnetic susceptibility multiplied by temperature of Fe_3CrL^{Ph}.

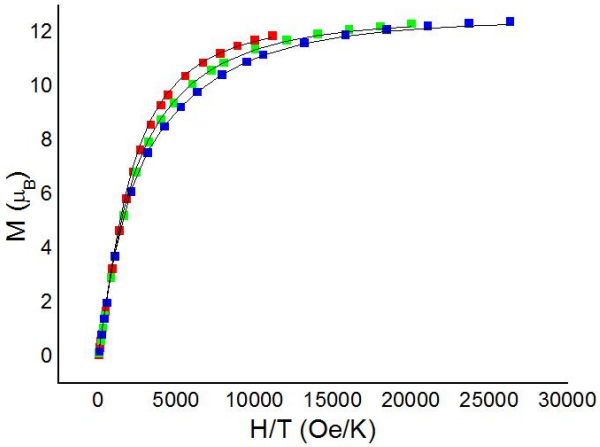

Figure 2.17: Field dependence of the magnetisation of Fe_3CrL^{Ph} at 1.9 (blue), 2.5 (green), and 4.5 K (red) versus the rescaled variable *H/T*. Solid lines represent the best fit values.

This behaviour is typical of ferrimagnetic spin arrangements, because on decreasing the temperature the higher values spin states are the first to be depopulated, due to the antiferromagnetic interaction between the central and peripheral spins. The ground state however, is not the one with smaller spin, because the external spins are oriented parallel to each other, thus resulting in a low temperature increase at low temperatures.

The values achieved at low temperature are in good agreement with S=3*5/2-3/2=6 ground state, χT *ca.* 21 emu K mol^{-1} for g=2. It is interesting

to notice here that in case metal scrambling would occur during the crystallisation the ground state would have a much lower spin S=2*5/2+3/2-5/2=4, with a χT of only 10 emu K mol^{-1}.

The data were reproduced assuming the following Exchange Spin Hamiltonian for a Cr centred propeller:

$$\hat{H} = J\hat{\mathbf{S}}_{Cr}\cdot(\hat{\mathbf{S}}_{Fe}+\hat{\mathbf{S}}_{Fe'}+\hat{\mathbf{S}}_{Fe''})+J'(\hat{\mathbf{S}}_{Fe}\cdot\hat{\mathbf{S}}_{Fe'}+\hat{\mathbf{S}}_{Fe'}\cdot\hat{\mathbf{S}}_{Fe''}+\hat{\mathbf{S}}_{Fe}\cdot\hat{\mathbf{S}}_{Fe''})$$

Equation 2.1

where the apex refers to symmetry related iron atoms, assuming threefold symmetry.

The best fit parameters are J = 13.4(4) cm^{-1}, J′ = −0.40(18) cm^{-1} and g = 1.97(1) for Fe_3CrL^{Et}, whereas J = 13.5(9) cm^{-1}, J′ = −0.19 (38) cm^{-1} and g = 2.04(2) for Fe_3CrL^{Ph}. These results in a ground S = 6 spin state separated from two degenerate S = 5 states by *ca.* 23 cm^{-1} and 22 cm^{-1} for Fe_3CrL^{Et} and $Fe_3CrL^{Ph}\cdot C_4H_{10}O_2$, respectively. The nearest neighbour interaction *J* is slightly smaller than for Fe_4 derivatives, 16–20 cm^{-1}, but compares well with the value (12.5 cm^{-1}) found in Fe_3CrL^{Ph}.[1] As the decrease of T at low temperature suggests the presence of zero field splitting of the ground spin multiplet, the isothermal magnetisation *vs.* field data at T = 1.9 K, 2.5 K and 4.5 K were measured. In fact at these temperatures only the ground S=6 is populated and deviations from the Brillouin curve are to be ascribed to the presence of zero field splitting, being the cluster well isolated one from the other and thus the intermolecular interactions rather weak.

The data, Figure 2.15, Figure 2.17, do not rescale on the reduced variable H/T, pointing to a sizeable magnetic anisotropy. The curves were reproduced assuming that only the S = 6 state is populate and split by axial anisotropy according to the Spin Hamiltonian:

$$\hat{\mathbf{H}}_{\mathrm{EPR}} = \mu_{\mathrm{B}}g\hat{\mathbf{S}}\cdot\hat{\mathbf{B}} + D\left[\hat{\mathbf{S}}_z^2 - S(S+1)/3\right] + E\left(\hat{\mathbf{S}}_x^2 - \hat{\mathbf{S}}_y^2\right)$$

Equation 2.2

with *D* = −0.20(8) cm^{-1}, g = 2.00(8) for Fe_3CrL^{Et} and *D* = −0.17(9) cm^{-1}, g = 2.08(9) for $Fe_3CrL^{Ph}\cdot C_4H_{10}O_2$, respectively. The quality of the fits provides strong support for the occurrence of only chromium centred Fe_3Cr species in the crystals, although a very low concentration of Fe_4 impurities could easily escape detection in static magnetic measurements.

The calculated *D* values are in good agreement with previous estimations performed on the solid solutions of Fe_3Cr and Fe_4. They therefore confirm a significant decrease of the magnetic anisotropy compared to the Fe_4 analogues. This can be ascribed to the fact that the Cr, in the octahedral environment produced by the tripodal ligand, induces a positive single ion *D* parameter, *i.e.* easy plane anisotropy. In contrast the Fe(III) ion in the same environment contributes with easy axis anisotropy.[1]

More informative are AC susceptibility data because the energy barrier associated with the magnetic anisotropy is expected to be significantly smaller in Fe_3Cr than in Fe_4 species (|D|S2 ≈ 10 K vs. 15 K for the energy barrier respectively as seen in chapter 1). In Figure 2.18 we show the frequency dependence of the out-of-phase component, χ′′, recorded on Fe_3CrL^{Et} at various temperatures. The results for $Fe_3CrL^{Ph}\cdot C_4H_{10}O_2$ are available in Figure 2.19). A static field of 1 kOe was applied to reduce the efficiency of under-barrier relaxation and shift the peaks to lower frequency, but peaks in χ′′ are also observable in zero field. The data were simulated assuming a single relaxing species using the Debye model and adding a phenomenological parameter, α, to account for a distribution of the relaxation time.

$$\chi''(\omega) = (\chi_T - \chi_S)\frac{(\omega\tau)^{1-\alpha}\cos\left(\frac{\pi\alpha}{2}\right)}{1 + 2(\omega\tau)^{1-\alpha}\sin\left(\frac{\pi\alpha}{2}\right) + (\omega\tau)^{2-2\alpha}}$$

Equation 2.3

Where χ_T and χ_S respectively are the isothermal and adiabatic limit of the susceptibility.

The fit is very good with reasonable α values ranging between 0.01 and 0.15, thus confirming the presence of one species only. In contrast, the solid solution Fe_3CrL^{Ph} revealed two relaxation processes ascribed to Fe_3Cr and Fe_4 species.[1]

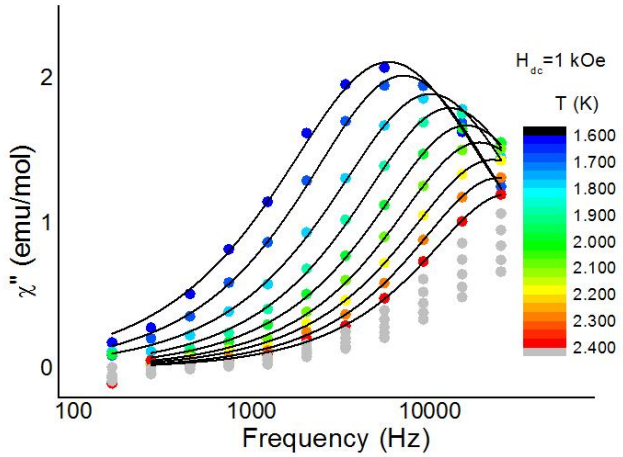

Figure 2.18: Frequency dependence of the out-of-phase component of the ac molar susceptibility of Fe_3CrL^{Et} in H_{dc} = 1 kOe and several temperatures (see colour legend). The black lines are the calculated values assuming one relaxing species.

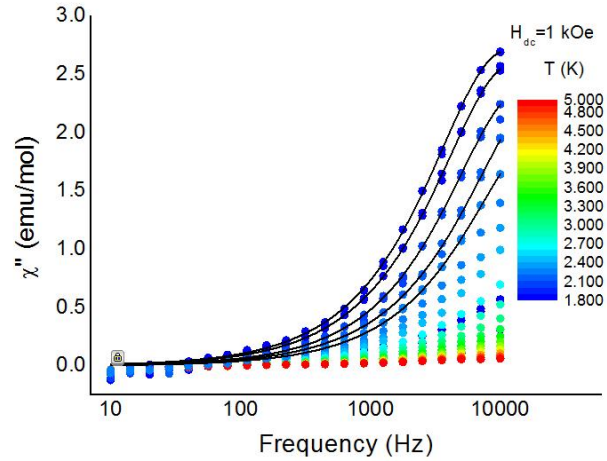

Figure 2.19: Frequency dependence of the out-of-phase component of the molar ac susceptibility of Fe_3CrL^{Ph} in *Hdc* = 1 kOe and several temperatures (see color legend). The black lines are the calculated values assuming one relaxing species.

From the data of Figure 2.18 and Figure 2.19, the temperature dependence of the relaxation time was extracted and shown in Figure 2.20 and Figure 2.21 respectively for Fe_3CrL^{Et} and Fe_3CrL^{Ph}. The activation energy was found to be ΔE = (8.7 ± 0.3) K and (7.1 ± 1.1) K, with pre-exponential factors $\tau^0 = (1.3 \pm 0.1) \times 10^{-7}$ s and $(2.8 \pm 1.6) \times 10^{-7}$ s, for Fe_3CrL^{Et} and $Fe_3CrL^{Ph}\cdot C_4H_{10}O_2$, respectively.

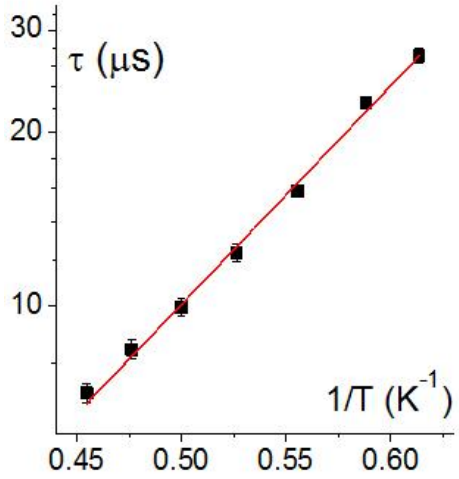

Figure 2.20: Temperature dependence of the relaxation time for Fe_3CrL^{Et} in a semi-logarithmic plot. The red line is the best fit curve using the Arrhenius law.

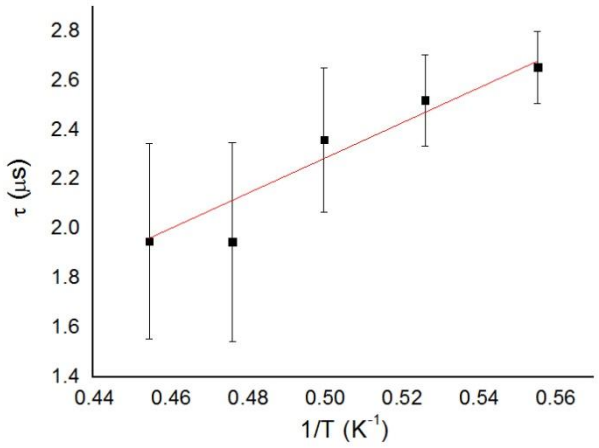

Figure 2.21: Temperature dependence of the relaxation for Fe_3CrL^{Ph} time in a semi-logarithmic plot and in red the best fit curve obtained with the Arrhenius law.

In the case of $Fe_3CrL^{Ph}\cdot C_4H_{10}O_2$, a different equipment was used with a slightly smaller range of available frequencies and temperatures (see Figure 2.22). This led to larger errors in the data treatments. The activation barrier for Fe_3CrL^{Et} is *ca.* 10% smaller than the energy splitting of the S = 6 multiplet, suggesting a non-negligible contribution of tunnelling mechanisms, already evidenced by the significant slowing down of the relaxation under static applied fields.

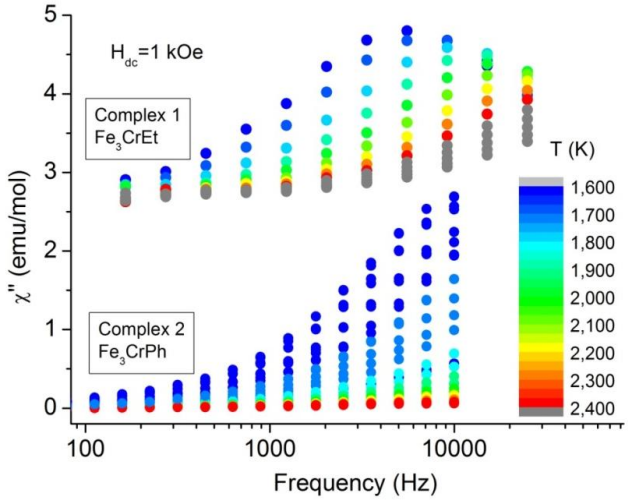

Figure 2.22: Comparison of the out-of-phase component of the molar ac susceptibility for Fe_3CrL^{Et} and Fe_3CrL^{Ph} in *Hdc* = 1 kOe. The measurements are carried out with two different equipments. Data of Fe_3CrL^{Et} has been shifted vertically for clarity.

2.4.4 Electron Paramagnetic Resonance

W-band EPR spectra were recorded on microcrystalline powders of Fe_3CrL^{Et}, $Fe_3CrL^{Ph}\cdot C_4H_{10}O_2$ and the solid solution of Cr-centred Fe_3Cr and Fe_4 reported in reference [1] by using a Bruker Elexsys E-600 spectrometer. The powders were blocked in wax to avoid preferential orientation due to magnetic torque. Temperature control in the range of 5-20 K was achieved using a ^{4}He continuous flow cryostat (CF935, Oxford Instruments). Spectral simulations were carried out using the Sim software developed by H. Weihe, University of Copenhagen.[34]

Although the magnetic characterisation indicates that Fe_3CrL^{Et} and $Fe_3CrL^{Ph}\cdot C_4H_{10}O_2$ do not contain Fe_4 clusters, Electron Paramagnetic Resonance spectra were recorded because of the high sensitivity of the technique. W-band EPR spectra recorded on powder samples of Fe_3CrL^{Et} and $Fe_3CrL^{Ph}\cdot C_4H_{10}O_2$ are shown in Figure 2.23.

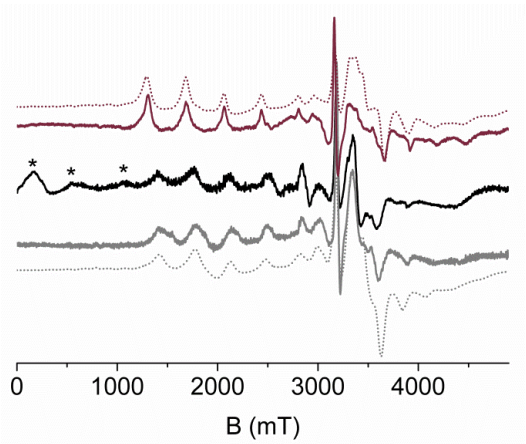

Figure 2.23: Experimental (continuous traces) and best simulated (dotted traces) W-band EPR spectra at 10 K, of Fe_3CrL^{Et} (upper, purple), of Fe_3CrL^{Ph} obtained following the procedure reported in ref. 1 (centre, black), and Fe_3CrL^{Ph} (lower, grey). The asterisks mark the signals attributed to the residual Fe_4 cluster, observable only for the black spectrum.

The spectra of Fe_3CrL^{Et} and $Fe_3CrL^{Ph}\cdot C_4H_{10}O_2$ are characterised by well defined fine structures, especially in the low field region that for systems with $D<0$ corresponds to parallel transitions region. The temperature dependences in Figure 2.24 shows the typical increase of the intensity on the lowest field transition on decreasing the temperature, typical for an S = 6 ground state with an easy axis anisotropy.

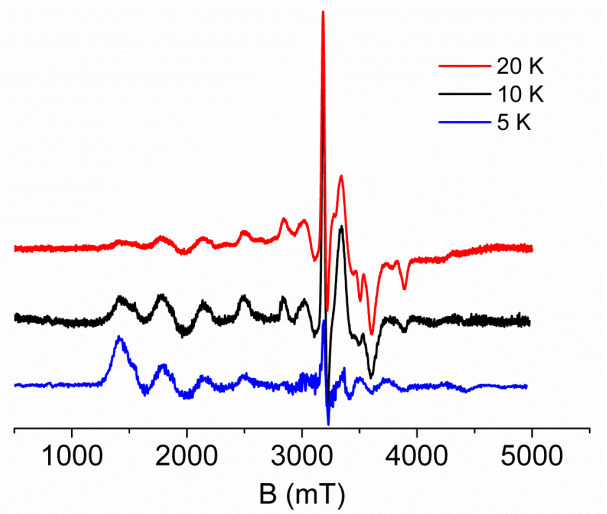

Figure 2.24: Temperature dependence of the W-band (94.35 GHz) EPR spectrum of a microcrystalline powder sample of Fe_3CrL^{Ph}.

For comparison we also reported in Figure 2.23 the spectrum of the Fe_3CrL^{Ph} derivative, previously obtained with the one step synthetic procedure. In this case, in addition to the features observed in $Fe_3CrL^{Ph}\cdot C_4H_{10}O_2$, a second set of resonances is revealed. On the basis of the line positions and their temperature dependence, this contribution can be easily attributed to the Fe_4 cluster present in the solid solution.[1,19,35] The absence of this series of signals in the spectra of Fe_3CrL^{Et} and $Fe_3CrL^{Ph}\cdot C_4H_{10}O_2$ definitely confirms the exclusive presence of Fe_3Cr clusters in both products, even in the limit of EPR sensitivity.

The obtained spectra were further used to accurately determine the zero field splitting parameters of the measured clusters, thus complementing the results of DC and AC magnetic characterisation. Good simulations of all spectra were obtained using the following Spin Hamiltonian:

$$\hat{\mathbf{H}}_{\mathrm{EPR}} = \mu_{\mathrm{B}} g \hat{\mathbf{S}} \cdot \hat{\mathbf{B}} + D\left[\hat{\mathbf{S}}_z^2 - S(S+1)/3\right] + E\left(\hat{\mathbf{S}}_x^2 - \hat{\mathbf{S}}_y^2\right)$$

Equation 2.4

Best fit spectra were obtained by using g = (2.000 ± 0.005), D = (−0.174 ± 0.001) cm^{-1}, E = (0.016 ± 0.001) cm^{-1} for Fe_3CrL^{Et}, and g = (2. 009 ± 0.008), D = (−0.168 ± 0.001) cm^{-1} and E = (0.014 ± 0.002) cm^{-1} for $Fe_3CrL^{Ph}\cdot C_4H_{10}O_2$.

The observation of a sizeable transverse term E indicates that, although crystallising in a trigonal space group, molecules of Fe_3CrL^{Et} are

intrinsically nonaxial, as expected for an ethyl-substituted tripodal ligand. The high crystallographic symmetry thus results from disorder effects, as already evidenced by x-ray analysis (see section 2.4.1). The parameters so obtained are in agreement with the findings of AC susceptibility, suggesting that the anisotropy barrier to the thermal relaxation is somehow higher in Fe_3CrL^{Et} than in $Fe_3CrL^{Ph}\cdot C_4H_{10}O_2$. Furthermore, the presence of transverse anisotropy terms in the Spin Hamiltonian is consistent with the relevant contribution of tunnelling mechanisms to the relaxation of the magnetisation observed by AC susceptibility. Finally, we note that the remarkable broadening of the transitions observed at high field requires the inclusion of *D*- and *E*-strain parameters, with $0.5|E|$ as an upper limit estimate for the *E* distribution width. Such a large value for *E*-strain is not a novelty for propeller-like clusters, having been recently reported for an Fe_4 cluster doped in a diamagnetic matrix of Ga_4.[36]

(1) Tancini, E.; Rodriguez-Douton, M. J.; Sorace, L.; Barra, A.-L.; Sessoli, R.; Cornia, A. *Chem. Eur. J.* **2010**, *16*, 10482–10493.

(2) Viguier, R.; Serratrice, G. *Eur. J. Inorg. Chem.* **2001**, 1789–1795.

(3) Schlegel, C.; Slageren, J. Van; Manoli, M.; Brechin, E. K.; Dressel, M. *Polyhedron* **2009**, *28*, 1834–1837.

(4) Tidmarsh, I. S.; Scales, E.; Brearley, P. R.; Wolowska, J.; Sorace, L.; Caneschi, A.; Laye, R. H.; McInnes, E. J. L. *Inorg. Chem.* **2007**, *46*, 9743–9753.

(5) Tidmarsh, I. S.; Batchelor, L. J.; Scales, E.; Laye, R. H.; Sorace, L.; Caneschi, A.; Schnack, J.; McInnes, E. J. L. *Dalton Trans.* **2009**, *312*, 9402–9409.

(6) Morgenstern, B.; Steinhauser, S.; Hegetschweiler, K.; Garribba, E.; Micera, G.; Sanna, D.; Nagy, L. *Inorg. Chem.* **2004**, *43*, 3116–3126.

(7) Morgenstern, B.; Kutzky, B.; Neis, C.; Stucky, S.; Hegetschweiler, K.; Garribba, E.; Micera, G. *Inorg. Chem.* **2007**, *46*, 3903–3915.

(8) Schlegel, C.; Burzurí, E.; Luis, F.; Moro, F.; Manoli, M.; Brechin, E. K.; Murrie, M.; van Slageren, J. *Chem. Eur. J.* **2010**, *16*, 10178–10185.

(9) Batchelor, L. J.; Shaw, R.; Markey, S. J.; Helliwell, M.; McInnes, E. J. L. *Chem. Eur. J.* **2010**, *16*, 5554–5557.

(10) Mehrotra, R. C.; Singh, A. *Polyhedron* **1998**, *17*, 689–704.

(11) Reis, D. M.; Westrup, K. C. M.; Nunes, G. G.; Barison, A.; Ribeiro, R. R.; de Sá, E. L.; Hughes, D. L.; Fernandes Soares, J. *J. Braz. Chem. Soc.* **2009**, *20*, 613–626.

(12) Nunes, G. G.; Friedermann, G. R.; Hitchcock, P. B.; de Sá, E. L.; Fernandes Soares, J. *Inorganica Chim. Acta* **2006**, *359*, 1435–1441.

(13) Wu, B. Y. C. S.; Rossman, G. R.; Gray, H. B.; Hammond, G. S.; Schugar, H. J. *Inorg. Chem.* **1972**, *11*, 990–994.

(14) Brown, D. A.; Cunningham, D.; Glass, W. K. *J. Chem. Soc. A Inorganic, Phys. Theor.* **1968**, 1563–1568.

(15) Kokot, E.; Mockler, G.; Sefton, G. *Aust. J. Chem.* **1975**, *28*, 299–304.

(16) Bradley, D. C.; Mehrotra, R. C.; Gaur, D. P. *Metal alkoxides*; Academic Press: New York, **1978**; p. 411.

(17) Armarego, W. L. .; Perrin, D. . *Purification of Laboratory Chemicals*; 4th ed.; Butterworth-Heinemann, **1997**; p. 544.

(18) Herwig, W.; Zeiss, H. *J. Org. Chem.* **1958**, *23*, 1404.

(19) Accorsi, S.; Barra, A.-L.; Caneschi, A.; Chastanet, G.; Cornia, A.; Fabretti, A. C.; Gatteschi, D.; Mortalo, C.; Olivieri, E.; Parenti, F.; Rosa, P.; Sessoli, R.; Sorace, L.; Wernsdorfer, W.; Zobbi, L. *J. Am. Chem. Soc.* **2006**, *128*, 4742–4755.

(20) Sheldrick, G. M. SHELXS-97: Program for Crystal Structure Solution, University of Göttingen, Germany **1997**.

(21) Sheldrick, G. M. SHELXL-97: Program for Crystal Structure Refinement, University of Göttingen **1997**.

(22) Sheldrick, G. M. *Acta Crystallogr. A.* **2008**, *64*, 112–22.

(23) Spek, A. L. *J. Appl. Crystallogr.* **2003**, *36*, 7–13.

(24) Mannini, M.; Tancini, E.; Sorace, L.; Sainctavit, P.; Arrio, M.-A.; Qian, Y.; Otero, E.; Chiappe, D.; Margheriti, L.; Cezar, J. C.; Sessoli, R.; Cornia, A. *Inorg. Chem.* **2011**, *50*, 2911–2917.

(25) Batchelor, L. J.; Sander, M.; Tuna, F.; Helliwell, M.; Moro, F.; van Slageren, J.; Burzurí, E.; Montero, O.; Evangelisti, M.; Luis, F.; McInnes, E. J. L. *Dalt. Trans.* **2011**, *40*, 5278–5284.

(26) Shannon, R. D.; Prewitt, C. T. *Acta Crystallogr. Sect. B Struct. Crystallogr. Cryst. Chem.* **1969**, *25*, 925–946.

(27) Cornia, A.; Fabretti, A. *Angew. Chemie Int. Ed.* **2004**, *43*, 1136–1139.

(28) Saalfrank, R. W.; Bernt, I.; Chowdhry, M. M.; Hampel, F.; Vaughan, G. B. M. *Chem. Eur. J.* **2001**, *7*, 2765–2769.

(29) Gregoli, L.; Danieli, C.; Barra, A.-L.; Neugebauer, P.; Pellegrino, G.; Poneti, G.; Sessoli, R.; Cornia, A. *Chem. Eur. J.* **2009**, *15*, 6456–6467.

(30) Douglas Kissler, K.; Sheppard, S. K.; Eaton, G. R.; Eaton, S. S. *J. Magn. Reson.* **1985**, *63*, 74–87.

(31) Barra, a. L.; Caneschi, a.; Cornia, a.; Fabrizi de Biani, F.; Gatteschi, D.; Sangregorio, C.; Sessoli, R.; Sorace, L. *J. Am. Chem. Soc.* **1999**, *121*, 5302–5310.

(32) Kahn, O. *Molecular Magnetism*; Wiley: New York, **1993**; p. 396.

(33) Carlin, R. L. *Magnetochemistry*; Springer-Verlag: Berlin, **1986**; p. 328.

(34) Jacobsen, C. J. H.; Pedersen, E.; Villadsen, J.; Weihe, H. *Inorg. Chem.* **1993**, *32*, 1216–1221.

(35) Prasad, T. K.; Poneti, G.; Sorace, L.; Rodriguez-Douton, M. J.; Barra, A.; Neugebauer, P.; Costantino, L.; Sessoli, R.; Cornia, A. *Dalt. Trans.* **2012**, *41*, 8368–8378.

(36) Vergnani, L.; Barra, A.-L.; Neugebauer, P.; Rodriguez-Douton, M. J.; Sessoli, R.; Sorace, L.; Wernsdorfer, W.; Cornia, A. *Chem. Eur. J.* **2012**, *18*, 3390–3398.

Chapter 3

Transverse anisotropy in a trigonal Fe_3Cr cluster

3.1 Transverse anisotropy in a trigonal Fe_3Cr cluster

As we have previously seen in chapter 2, one of the greatest advantages coming from this synthetic approach arises from the pure heterometallic Fe_3Cr phase, with no contamination of Fe_4 cluster, originated from the synthesis. Despite the fact that the cluster with the H_3L^{Et} tripodal ligand crystallizes in a trigonal space group, each cluster has actually a lower symmetry (two fold symmetry) due to the ligand structure. The higher symmetry of the cluster depends on the fact that the average of the three positions (available for the ethyl residue around its axis) is detected. This is sufficient to induce transverse anisotropy of second order, which makes the determination of higher order transverse components of 3^{rd} and 6^{th} order hardly detectable by EPR spectroscopy. On the other hand, we have seen in chapter 1 that high order transverse anisotropy terms are actually dominating the tunnel mechanism of relaxation.

We decided therefore to extend the synthetic approach, developed in chapter 2, to a H_3L^{Me} tripodal ligand derivative, in order with such a ligand, to eliminate the disorder brought by the ethyl residue of the H_3L^{Et} ligand (as we showed in 2.4.1 section), and having at the same time, a crystallographic imposed trigonal symmetry.

The synthesis, discussed in detail in 2.3.1 section of the previous chapter, involves first the formation of the central molecule chromium core $\{[Cr(L^{Me})_2]Li_3\}$, then its reaction with Fe^{III} dimer, to build the external part of the complex. A very low yield (not calculated) was attainable, due to the low solubility of the ligand, conferred to the chromium intermediate. The recrystallisation has also hardly succeeded, involving several months for small, but well formed and not geminated, crystals to form by slow evaporation of hexane in a closed chamber.

Small dark brown hexagonal prism crystals of Fe_3CrL^{Me} were used to determine the unit cell by x-ray diffractometry and for monocrystal EPR investigations. The latter and the development of the theoretical approach were carried by Dr Lorenzo Sorace who works in our research group.

3.2 Fe_3CrL^{Me} crystallographic cell determination

Freshly synthesised hexagonal prismatic single crystals of Fe_3CrL^{Me} were used for a crystallographic investigation at 100 K using Mo K_α radiation (λ = 0.71073 Å). The goal of this measurement was, first of all, to check the crystallisation group of Fe_3CrL^{Me} and if it was isomorphous with the analogue Fe_4L^{Me},[1] then, to find the cell parameters in order to identify the faces of the crystal.

From this study we found out that the complex crystallises in the trigonal space group $R\bar{3}c$ with the unit cell parameters a=b=16.1435(11) Å and c=57.073(2) Å (hexagonal setting), determining that it is completely isomorphous with its tetrairon(III) analogue.[1] This allows us to assume that Fe_3CrL^{Me} has the same crystallographic structure of Fe_4L^{Me}. In the case of Fe_3CrL^{Me} cluster the structure was impossible to solve because of the features of its crystals, which were geminated or too small for the data collection. Such cluster has three C_2 fold axis along the central iron – peripheral iron direction, due to its perfect planarity, and a main C_3 fold axis perpendicular to the molecular plane, passing through the central ion. For this reason the latter symmetry axis is also the magnetic axis of the molecule.

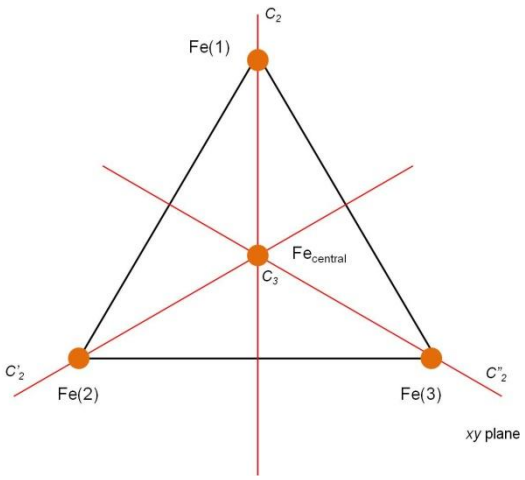

Figure 3.1: Schematic representation of Fe_4 cluster geometry in the molecular plane (*xy*). Red lines are the twofold axes. C_3 symmetry axis (not drawn) is perpendicular to the plane and pass through the central atom.

The Miller indices of the crystal faces were obtained by cell determination in order to orient the crystals in the EPR spectrometer (see below). The flat and more developed faces of the crystal were identified as (001) and (00$\bar{1}$)

and were, thus, perpendicular to the trigonal symmetry axis *z*. This allowed an easy mounting for rotation around c and in a plane perpendicular to it.

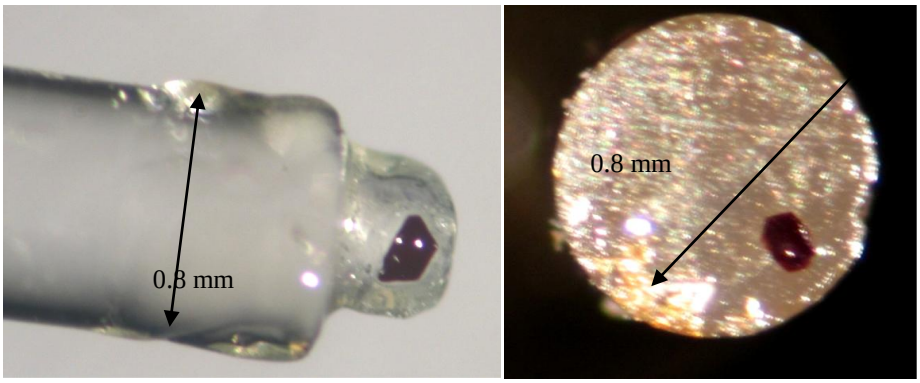

Figure 3.2: Picture of the crystal of Fe_3CrL^{Me}, glued on a cubic crystal of NaCl, used for W-band EPR study: rotation – right: in the *xy* plane (hard plane); left: from the *z* axis to the *xy* plane.

This particular well-built crystal conformation, with the most developed face (001) perpendicular to the easy axis of magnetisation *z*, *i.e.* relative to the molecular hard plane *xy*, together with the proved chemical crystal purity obtained with this modular synthetic strategy, allow us to accurately study and determine the transverse magnetic anisotropy of the molecule. Such a study cannot be possible in case of using the one pot synthesis as described in ref 2. Moreover, the homometallic isomorfous analogue of Fe_3CrL^{Me}, Fe_4L^{Me}, does not respect the mandatory features of crystal quality. Therefore, this investigation could not be applied, beyond the fact that it has second order transverse anisotropy terms, which make the detection of higher order terms impossible and only theorizable.[1] Such an investigation was tried on Fe_4 cluster, and brought to a non consistent result with respect to a trigonal anisotropy, because tetrairon cluster has a threefold symmetric distribution of rhombic anisotropy.

3.3 Fe_3CrL^{Me} magnetic characterisation

Magnetic measurements, for Fe_3CrL^{Me} derivative, are in good agreement with the ones for Fe_3CrL^{Et} and Fe_3CrL^{Ph}, showing the contribution of only one specie.

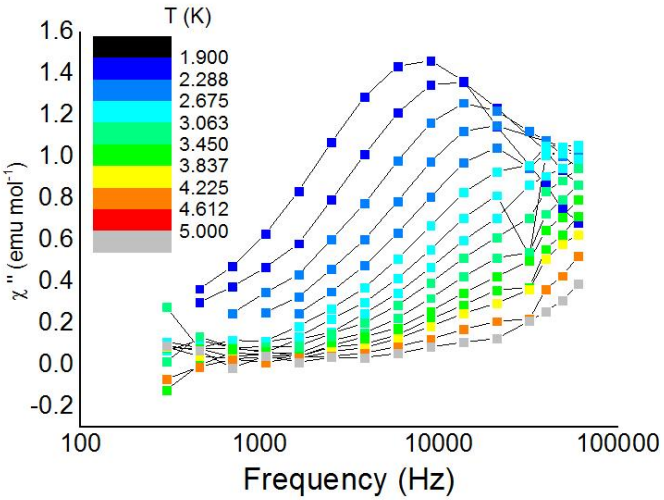

Figure 3.3: Frequency dependence of the out-of-phase component of the AC molar susceptibility of Fe_3CrL^{Me} in H_{dc} = 1 kOe and several temperatures (see colour legend).

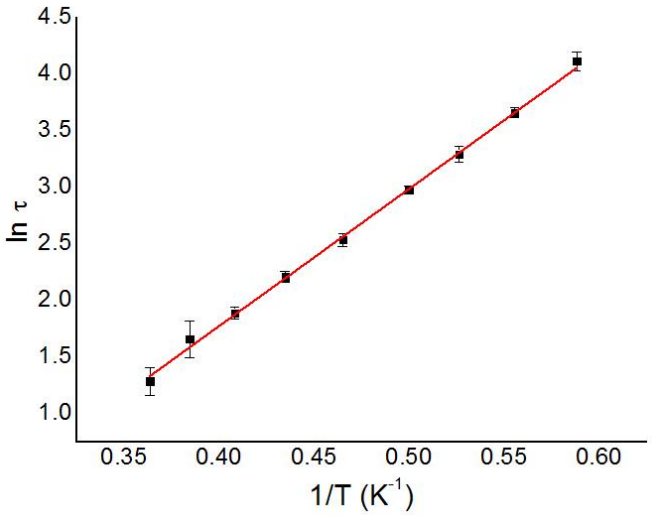

Figure 3.4: Temperature dependence of the relaxation for Fe_3CrL^{Me} time in full logarithmic scale and in red the best fit curve obtained with the Arrhenius law.

From the fitting of the AC susceptibility curves, in Figure 3.3, of the out-of-phase component, χ'', using the Debye model as discussed in chapter 2 (Equation 2.3), the temperature dependence of the relaxation time was extracted (Figure 3.4). The activation energy was found to be $\Delta E = (12.1 \pm 0.1)$ K, with pre-exponential factors $\tau^0 = (4.6 \pm 0.1) \times 10^{-8}$ s. The anisotropy D value is consistent with the others with different tripodal ligand.

It has to be noted that AC measurements in Figure 3.5 show that Fe_3Cr complex has a slowdown of the relaxation process in presence of a magnetic field. Comparing the relaxation frequencies in H_{DC} = 1 kOe and H_{DC} = 100 Oe at the same temperature it is possible to see that the more intense is the field, the larger is the relaxation time, with a decrease of the process rate. This is due to the presence of high order transverse anisotropy which induces quantum tunnelling, as discussed in chapter 1.

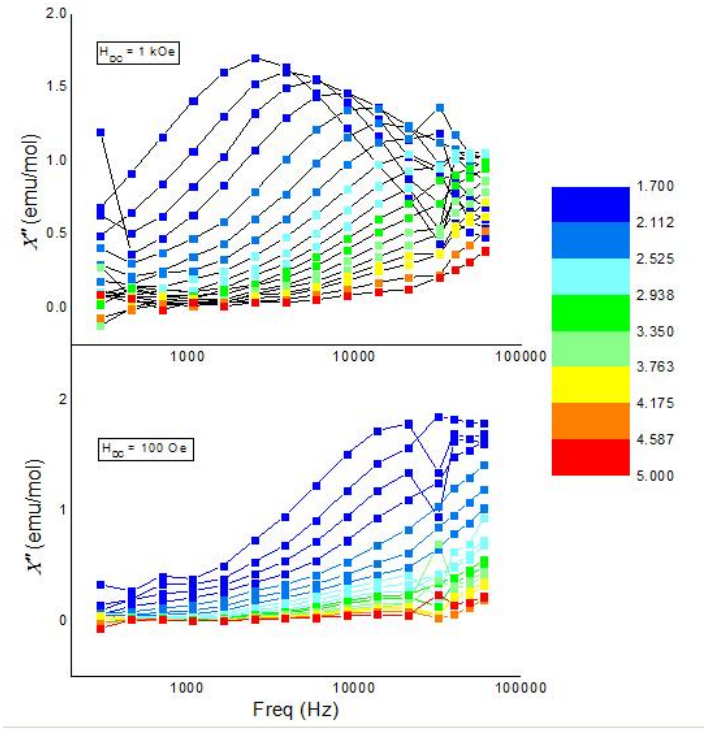

Figure 3.5: Frequency dependence of the out-of-phase component of the AC molar susceptibility of Fe_3CrL^{Me} in H_{DC} = 1 kOe (top) and H_{DC} = 100 Oe (bottom).

3.4 Determination of Fe_3CrL^{Me} transverse anisotropy by EPR

As described in chapter 1, transverse magnetic anisotropy is of primary importance for the appearance of quantum effects in the double well potential of a SMM. In fact, when the anisotropy is purely axial, *i.e.* the plane perpendicular to the easy axis is completely isotropic, quantum tunnelling is forbidden in a longitudinal field.[3] By contrast, transverse anisotropy can mix spin states localised on different sides of the barrier, thereby opening effective tunnelling pathways.

The low-temperature magnetic properties of such systems are usually analysed using a giant-spin approach (GSA). Within this formalism, only the ground spin multiplet is considered, the system is described in terms of states corresponding to the total spin and magnetic anisotropy is then introduced as a perturbation, acting on the ground manifold. A multipolar series expansion is used to describe the system, with terms up to the $2S^{\text{th}}$ order in spin operators, the so-called Stevens operator equivalents, $B_k^q \hat{O}_k^q$.[4] The main advantage of the GSA lies in the relatively small number of free parameters required, since the number of terms is both spin ($k \leq 2S$, $-k \leq q \leq k$) and symmetry restricted. To correctly grasp the origin of high-order ($k > 2$) anisotropy terms appearing in the GSA, as well as to account for some subtle effects in relaxation, it is essential to adopt a multispin approach (MSA), which explicitly considers the internal degrees of freedom, *e.g.* the anisotropy of each constituent spin and the details of spin-spin interactions.[5–8] These high-order anisotropies are especially relevant in axially symmetric molecules, where second-order ($k = 2$) transverse anisotropy ($q \neq 0$) vanishes and quantum tunnelling can be promoted only by transverse terms with $k > 2$ and $q \neq 0$. High-order transverse anisotropies have been experimentally determined and their relation to the multispin nature of the systems proved for two SMMs with fourfold symmetry only.[7,8]

For these reasons the analysis of systems with rigorous threefold (trigonal) symmetry represents a great advance in SMM field. Indeed, since $\hat{O}_k^q$ terms with $q = 3$ and 6 couple only states differing by $\Delta M_S = \pm 3, \pm 6$, where M_S labels the projection of the total spin onto the C_3 (z) axis, nonzero tunnelling gaps would be limited to level crossings with $|\Delta M_S| = 3n$ (n is a positive integer). This should provide a peculiar periodicity of the tunnel splitting, and thus of magnetisation dynamics, on application of a transverse field.[9] Moreover in the case of an $S = 6$ state in trigonal symmetry, as the Fe_3CrL^{Me} cluster, the two states of the ground doublet,

i.e. $M_S = \pm 6$, are directly admixed by transverse anisotropy, since $\Delta M_S = 12 = 3n$.

The EPR characterisation was performed at W-band frequency, due to the zfs parameter of the system that requires high frequency and a wide field range to record all the resonance lines of the S=6 ground state of the molecule. The experimental setup is completed with a resonant cavity, in which the sample is placed, suitable for the frequencies we used. This led to an enormous increase of the sensibility of the method.

The first experiment consisted in measuring the EPR spectra of Fe_3CrL^{Me} with the static magnetic field along the trigonal $\boldsymbol{z}$ axis at variable temperature (6-40 K). The spectra are presented in Figure 3.6 in their standard derivative form. At the lowest investigated temperature seven main lines are observed, which can be attributed to $\Delta M_S = 1$ transitions between the lowest lying M_S levels of the $S = 6$ ground multiplet.

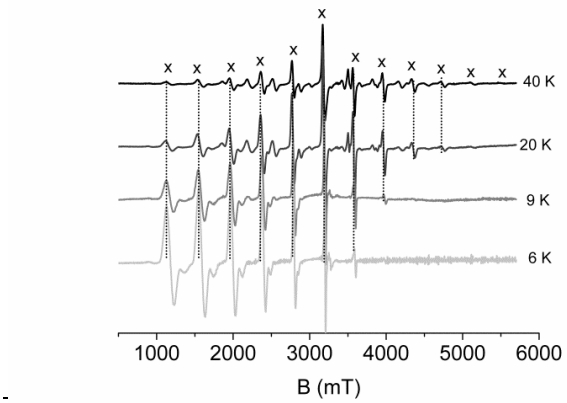

Figure 3.6: *Temperature dependence of the W-band EPR spectrum of Fe_3CrL^{Me} obtained with static field applied along the c crystallographic axis. The crosses and the dotted lines evidence the 12 signals of the ground S = 6 state.*

Interestingly, even at this temperature, additional weaker signals are visible in between the main lines. On increasing temperature their relative intensity increases, suggesting that they originate from transitions within the first-excited spin multiplets with $S = 5$; at 20 K, the whole sets of 12 and 10 lines expected for the $S = 6$ and $S = 5$ states are observed. A further set of evenly-spaced lines, barely visible at 20 K, become more pronounced at the highest measured temperature (40 K), so that we attribute them to the second set of excited multiplets with $S = 4$.

The spectra were plotted using GSA based axial Hamiltonian, fitting the resonance fields of the $|M_S\rangle \rightarrow |M_S+1\rangle$ transitions as a function of M_S quantum number

$$\hat{H}_{ax} = \mu_B g_z B_z \hat{S}_z + DS_z^2 + B_4^0 \hat{O}_4^0$$

Equation 3.1

The simulation yielded the following values for the axial zero field splitting: S = 6, g_z = (2.007 ± 0.002), D = (-0.1845 ± 0.0007) cm^{-1}, S = 5, g_z = (2.002 ± 0.003), D = (-0.155 ± 0.001) cm^{-1}. The negative D parameters indicate that ***z*** is an easy magnetic axis, as expected for a SMM, and that ***xy*** is an hard magnetic plane. As mentioned in chapter 2 the same parameters for the analogue Fe_3CrL^{Et} are g = (2.000 ± 0.005), D = (−0.174 ± 0.001) cm^{-1} and for $Fe_3CrL^{Ph}{\cdot}C_4H_{10}O_2$ g = 2.00, D = (−0.168 ± 0.001) cm^{-1} in a ground S = 6 spin state.

Rotation of the crystal away from the ***z*** axis expectedly results in a reduction of the field range spanned by the spectrum, which reaches its minimum extension close to the magic angle. It is immediately evident from Figure 3.7 that on moving from θ = 0° to θ = 90° a relevant broadening of the EPR lines occurs, so that the spectrum in the ***xy*** plane is much less resolved than in the axial direction. As a consequence, the lines observed when the field is applied at large angles from the easy axis cannot be assigned by simple inspection.

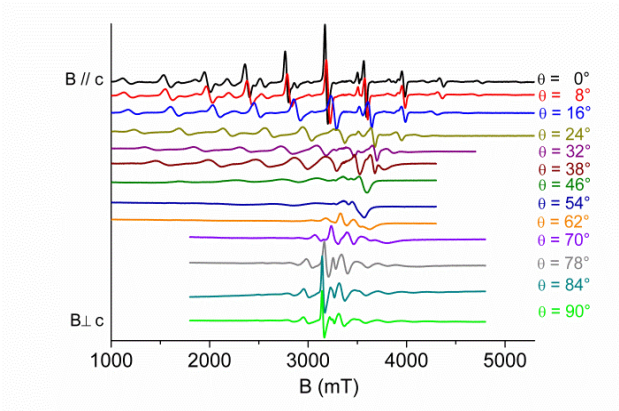

Figure 3.7: *Angular dependence of the W-band EPR spectrum of* Fe_3CrL^{Me} *at 20 K when rotating the crystal from the c crystallographic axis (θ = 0°) to the* ***xy*** *plane (θ = 90°, φ = 15°; here, when φ = 30°the applied static field is parallel to the Fe-Cr direction).*

Figure 3.8 presents the angular dependence of the spectra recorded at 20 K by applying the static field in the ***xy*** plane at different angles (φ) from the Fe-Cr direction (see the caption of Figure 3.7 for definition). Due to the extremely weak angular dependence of the resonance fields the intensity of the spectra was plotted in a bidimensional graph with a colour intensity scale, which allows evidencing a 60° periodicity of some specific resonances. This confirms the expected threefold symmetry and indicates that the rotation was correctly performed around ***z*** with a negligible misalignment (< 1°).

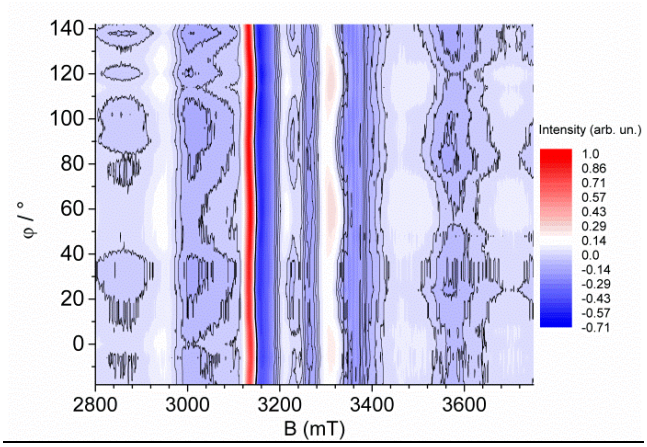

Figure 3.8: *Bidimensional plot of the angular dependence of W-band EPR spectra measured in the* ***xy*** *plane (i.e. perpendicular to the trigonal axis). At φ = 30° the static field is parallel to the Fe-Cr direction.*

In the following discussion we will focus on the angular dependence of the transitions occurring around 2980, 3146, 3330 and 3530 mT. On the basis of the above estimates of axial zfs parameters, these bands can be unequivocally attributed to resonances within the ground $S = 6$ multiplet. A first relevant point to be noted is that the lowest-field transition displays an angular modulation with opposite phase as compared to the remaining three transitions. This is a clear indication that the observed periodicity cannot be ascribed to a local lowering of the D_3 molecular symmetry while preserving trigonal crystal symmetry, *i.e.* to a 3-fold symmetric distribution of rhombic anisotropies, as previously suggested for the corresponding Fe_4 derivative.[10]

In our case, the observed angular dependence was then firmly attributed to the presence of trigonal anisotropy terms in the zfs interactions.

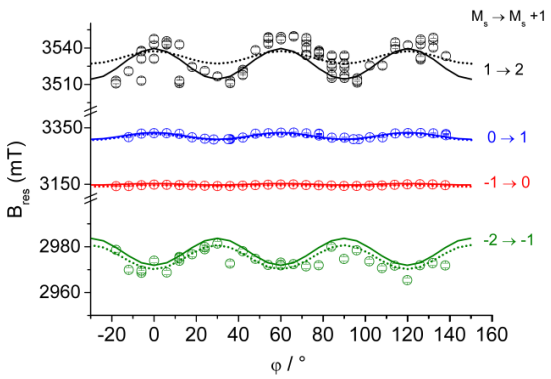

Figure 3.9: *Experimental (circles) and calculated angular dependence of the central $|M_S>$ → $|M_S+1>$ transitions in the **xy** plane.*

It is essential to stress that, this type of anisotropy, with the lowest field transition which displays an angular modulation with opposite phase compared with the remaining three transitions, is a clear indication that the observed periodicity cannot be ascribed to a local lowering of the D_3 molecular symmetry while preserving trigonal crystal symmetry, *i.e.*, to a threefold symmetric distribution of rhombic anisotropies, as previously suggested for the corresponding Fe_4 derivative.[10] In our case, the observed angular dependence was then firmly attributed to the presence of trigonal anisotropy terms in the zfs interactions. For a D_3 symmetric molecule the complete giant spin Hamiltonian up to the sixth order is:

$$\widehat{H}_{D_3} = \mu_B \boldsymbol{B} g \hat{S} + DS_z^2 + B_4^0 \hat{O}_4^0 + B_4^3 \hat{O}_4^3 + B_6^3 \hat{O}_6^3 + B_6^6 \hat{O}_6^6$$

Equation 3.2

As a first step toward an accurate determination of B_k^q parameters with $q = 3$ and 6, we performed sample calculations to test the effect of each term on the resonance field for the examined transitions. It turned out that the experimentally observed relative phases were correctly reproduced even by introducing a $B_6^0 \hat{O}_6^6$ term only. However, retrieval of the correct modulation amplitudes and resonance fields requires the introduction of both $B_4^3 \hat{O}_4^3$ and $B_6^3 \hat{O}_6^3$ terms. We noted that, while the sign of B_6^6 is directly related to the phase of angular modulation, the absolute signs of B_k^3 had no effect, and only their relative signs could be determined from the available data. Angle-dependent measurements away from the *xy* plane would resolve this ambiguity but are unfeasible owing to the crystal morphology. This behaviour is directly related to the form of Stevens operators with odd q, which contain contributions from odd powers of S_z.[11] For the same reason

these terms in principle affect the position of the parallel transitions, too. Therefore, the angle-dependent resonance fields in the plane and those along the easy axis for the $S = 6$ state were simultaneously fitted using full diagonalisation of the spin Hamiltonian matrix. The best fit simulations presented in Figure 3.9 were obtained with the $S = 6$ parameters gathered in Table 3.1.

	***S* = 6**
g_z	2.008 ± 0.001
$g_{x,y}$	2.0131 ± 0.001
D	-0.1845 ± 0.0005 cm^{-1}
B_4^0	+2.0 ± 0.1 x 10^{-7} cm^{-1}
B_4^3	± 3.0 ± 0.5 x 10^{-4}
B_6^3	∓ 1.0 ± 0.1 x 10^{-5}
B_6^6	5.5 ± 0.5 x 10^{-7}
ΔB_{pp} [a]	30 mT
σ_D [a]	100 MHz
ΔE [a]	-

Table 3.1: Best-fit parameters obtained from the simulation of the EPR spectra within the GSA for the lowest multiplets S = 6 of Fe_3CrL^{Me}
[a] ΔB_{pp} is the distance between the position of the maximum and of the minimum in the first-derivative lineshape. σ_D is defined as the full width at half maximum of the Gaussian distribution of the scalar parameter D, ΔE is the energy of the excited multiplets above the ground $S = 6$ state.

As we discussed previously, the simultaneous presence of both $q = 3$ and $q = 6$ terms in the giant spin Hamiltonian turned out to be necessary to correctly reproduce the observed behaviour. It is essential to stress that sixth-order anisotropy terms cannot arise from the projection of single-ion anisotropies. Indeed, chromium(III) ion is an $S = 3/2$ centre, and its single-ion anisotropy may provide neither $k = 4$ nor $k = 6$ contributions (since $k \leq 2S$); in much the same way, high-spin iron(III) has no sixth-order single-ion terms, being an $S = 5/2$ ion. It has further to be noted that the use of GSA, and thus of latter equation, to describe both ground and excited states, apparently implies that the corresponding zfs parameters are independent of each other. However, in the strong exchange approximation

on which GSA relies, the second-order zfs tensor of any spin state S for a Fe_3Cr cluster is related to the microscopic anisotropic parameters (*i.e.*, single-ion and pairwise dipolar and anisotropic exchange interactions) through:

$$\mathbf{D}_S = d_{Fe}(\mathbf{D}_{Fe(1)} + \mathbf{D}_{Fe(2)} + \mathbf{D}_{Fe(3)}) + d_{Cr}\mathbf{D}_{Cr} + \sum_{j>i} d_{Fe(i),Fe(j)}\mathbf{D}_{Fe(i),Fe(j)} + \sum_{i=1,3} d_{Fe(i),Cr}\mathbf{D}_{Fe(i),Cr}$$

Equation 3.3

where $\mathbf{D}_{\mathrm{Fe}(i)}$ and $\mathbf{D}_{\mathrm{Cr}}$ are the single-ion anisotropy tensors, $\mathbf{D}_{\mathrm{Fe}(i),\mathrm{Fe}(j)}$ and $\mathbf{D}_{\mathrm{Fe}(i),\mathrm{Cr}}$ are the sum of dipolar and anisotropic exchange ones, while d_{Fe}, d_{Cr}, $d_{Fe,Fe}$ and $d_{\mathrm{Fe,Cr}}$ are projection coefficients calculated according to recursive relations.[12]

To account for both the observed threefold in-plane anisotropy and the magnitude of the axial anisotropy of the excited states, the strong exchange approximation inherent to the GSA must be abandoned and a multispin Hamiltonian (MSH) must be introduced:

$$\hat{H}_{MSH} = \sum_{i=1}^{3,j>i} \hat{\boldsymbol{S}}_{Fe(i)} \boldsymbol{J}_{Fe(i),Fe(j)} \hat{\boldsymbol{S}}_{Fe(j)} + \sum_{i=1}^{3} \hat{\boldsymbol{S}}_{Fe(i)} \boldsymbol{J}_{Fe(i),Cr} \hat{\boldsymbol{S}}_{Cr} + \mu_B \sum_{i=1}^{3} \boldsymbol{B}\, \boldsymbol{g}_{Fe(i)} \hat{\boldsymbol{S}}_{Fe(i)}$$
$$+ \mu_B \boldsymbol{B} \boldsymbol{g}_{Cr} \hat{\boldsymbol{S}}_{Cr} + \sum_{i=1}^{3} \hat{\boldsymbol{S}}_{Fe(i)}\, \boldsymbol{D}_{Fe(i)} \hat{\boldsymbol{S}}_{Fe(i)} + \hat{\boldsymbol{S}}_{Cr} \boldsymbol{D}_{Cr} \hat{\boldsymbol{S}}_{Cr}$$

Equation 3.4

where $\hat{\boldsymbol{S}}_{Fe(i)}$ (i = 1, 2, 3) and $\hat{\boldsymbol{S}}_{Cr}$are the spin operators for the iron and chromium centres, while $\boldsymbol{J}_{Fe(i),Fe(j)}$ and $\boldsymbol{J}_{Fe(i),Cr}$ represent the interaction tensors within iron-iron and iron-chromium pairs, respectively, containing both isotropic exchange and dipolar contributions. As before $\boldsymbol{D}_{Fe(i)}$ and $\boldsymbol{D}_{Cr}$ are the zfs tensors of the iron and chromium sites, whose g matrices are indicated by $\boldsymbol{g}_{Fe(i)}$ and $\boldsymbol{g}_{Cr}$, respectively. Following the usual conventions for D_3 symmetry, we chose the molecular reference frame (XYZ) with Z along the threefold symmetry axis, Y along the Cr-Fe(1) direction and X orthogonal to Y and Z. The orientation of each local tensor eigenframe (xyz) in the molecular frame was then specified in terms of its Euler angles α, β, γ (ZYZ convention).[11,13] The D_3 molecular symmetry imposes a number of constraints on the tensors/matrices appearing in the aforementioned equation. For instance, $\boldsymbol{D}_{Cr}$ and $\boldsymbol{g}_{Cr}$ must be axial along Z, and a principal direction of $\boldsymbol{D}_{Fe(i)}$ and $\boldsymbol{g}_{Fe(i)}$ must lie along the twofold axis joining Fe(i) with

Cr. In addition, the three $\boldsymbol{D}_{Fe(i)}$ tensors and the three $\boldsymbol{g}_{Fe(i)}$ matrices must be related by a threefold rotation around Z, with similar relationships holding for $\boldsymbol{J}_{Fe(i),Fe(j)}$ and $\boldsymbol{J}_{Fe(i),Cr}$ tensors (see Figure 3.10).

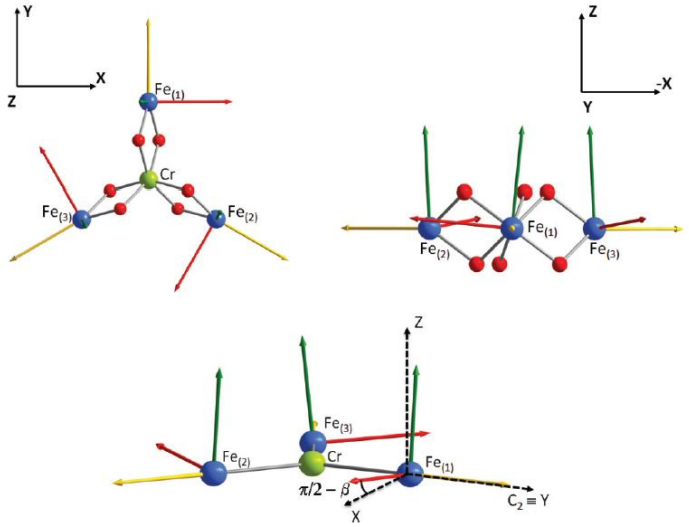

Figure 3.10: Arrangement of single-ion anisotropy tensors for the iron(III) ions in Fe_3Cr with respect to the molecular reference frame (XYZ). The single-ion tensors are related by a threefold rotation along Z and have a principal axis along the Cr-Fe direction, which is a C_2 symmetry axis. Red arrow: hard axis; yellow arrow: intermediate axis; green arrow: easy axis.

The direct simulation of EPR spectra using the last MSH equation was found quite demanding. To reduce the complexity of the problem, the analysis was then restricted to the levels involved in the experimentally observed resonances. These levels were identified by a preliminary analysis of the field-dependent energy pattern using anisotropy parameters from previous works. The axial (D_{Cr}, D_{Fe}) and rhombic (E_{Fe}) single-ion anisotropy parameters were set to the values found in an isostructural Ga_4 derivative doped with chromium(III) and iron(III) ions.[2] D_{Cr}, D_{Fe} and E_{Fe} with g_{Fe} and g_{Fe} are set from [11].

Noticeably, since all constituent ions have a hard-axis type anisotropy (D > 0), the observed easy-axis molecular anisotropy requires highly noncollinear $\boldsymbol{D}_{Fe(i)}$ tensors. Because of the aforementioned restrictions imposed by symmetry, the line joining Cr with Fe(i) can correspond either to the *hard* (z), to the *easy* (y), or to the *intermediate* (x) axis of the $\boldsymbol{D}_{Fe(i)}$ tensor. The first possibility was ruled out as it results in a 30° phase mismatch with respect to the observed resonance field modulation in the ***xy***

plane (*i.e.* $B_6^6 < 0$ in the GSA). This conclusion, which fully supports previous studies,[2,14,15] implies that the hard axis (z) of each $\boldsymbol{D}_{Fe(i)}$ tensor is normal to the corresponding Cr-Fe(i) direction, with no symmetry-imposed restriction on the angle β between z and Z.

However, γ can have only two possible values, 0° or 90°, depending on whether y or x is found along Cr-Fe(i). Additional guidance in better defining the orientation of $\boldsymbol{D}_{Fe(i)}$ tensors is provided by projection formulae. The observed D parameter in the $S = 6$ state requires the ZZ-component of $\boldsymbol{D}_{Fe(i)}$ to take the value $D_{ZZ} \simeq -0.30$ cm^{-1}.[2] This is very close to the largest negative component that can be reached with the adopted $D_{Fe(i)}$ and $E_{Fe(i)}$ values ($D_{ZZ} = -0.31$ cm^{-1}), suggesting that the local easy-axis y is roughly parallel to Z (*i.e.* $\beta \simeq 90°$ and $\gamma = 90°$). It is however apparent that the same molecular D can also be retrieved by setting $\beta \simeq 90°$ and $\gamma = 0°$, provided $D_{Fe(i)}$ and $E_{Fe(i)}$ are adjusted so as to afford the required D_{ZZ}. We could resolve this ambiguity by examining the angular variation of resonance fields in the hard plane predicted by the two arrangements. Indeed, if D_{ZZ} is kept constant to allow a correct reproduction of parallel spectra, for $\gamma = 90°$, the modulation amplitudes become larger as rhombicity is reduced, while the reverse holds for $\gamma = 0°$. This clearly indicates that the angular dependence of resonance fields in the $\boldsymbol{xy}$ plane, and thus the magnitude of the transverse trigonal anisotropy, is directly related to differences in the components of $\boldsymbol{D}_{Fe(i)}$ along X and Y. The arrangement with the *easy* axis y along Cr-Fe(i) invariably results in modulation amplitudes larger than observed, thereby ruling out the $\gamma = 0°$ option. It is on that basis that a very good reproduction of the hard-plane resonance fields, both compared with the experimental data and with GSA (Figure 3.9, dotted lines), was obtained.

3.5 Conclusions

The innovative synthetic strategy discussed in the previous chapter was used to prepare a heterometallic star-shaped cluster with crystallographically imposed trigonal symmetry. Indeed the complex Fe_3CrL^{Me} has a C_3 symmetry axis and crystallises in a trigonal space group. This feature, together with the chemical purity and absence of co-formation of homometallic species in the preparation, allows a single crystal EPR investigation. We could determine accurately the axial zero-field splitting terms of the molecule. Furthermore, spectra recorded by applying the magnetic field perpendicular to the trigonal axis showed a $\pi/6$ angular modulation. This behaviour is a signature of the presence of trigonal transverse magnetic anisotropy terms, whose values has been only theorised or calculate, but not determined in any SMM. Such in-plane anisotropy could only be justified by dropping the so-called “giant spin approach” and by considering a complete multispin approach. From a detailed analysis of experimental data with the two models, it emerged that the observed trigonal anisotropy directly reflects the structural features of the cluster, *i.e.* the relative orientation of single-ion anisotropy tensors and the angular modulation of single-ion anisotropy components in the hard plane of the cluster. Therefore, this places the easy axis component of anisotropy along the three-fold magnetic axis of the molecule and brings to an increasing of the total axial anisotropy.

(1) Cornia, A.; Fabretti, A. C.; Garrisi, P.; Mortalò, C.; Bonacchi, D.; Gatteschi, D.; Sessoli, R.; Sorace, L.; Wernsdorfer, W.; Barra, A.-L. *Angew. Chemie (International ed.)* **2004**, *43*, 1136–1139.

(2) Tancini, E.; Rodriguez-Douton, M. J.; Sorace, L.; Barra, A.-L.; Sessoli, R.; Cornia, A. *Chem. Eur. J.* **2010**, *16*, 10482–10493.

(3) Barra, A. L.; Gatteschi, D.; Sessoli, R. *Chem. Eur. J.* **2000**, *2*, 1608–1614.

(4) Stevens, K. W. H. *Proc. Phys. Soc. A* **1952**, *209*, 209.

(5) Carretta, S.; Liviotti, E.; Magnani, N.; Santini, P.; Amoretti, G. *Phys. Rev. Lett.* **2004**, *92*, 207205.

(6) Carretta, S.; van Slageren, J.; Guidi, T.; Liviotti, E.; Mondelli, C.; Rovai, D.; Cornia, a.; Dearden, a.; Carsughi, F.; Affronte, M.; Frost, C.; Winpenny, R.; Gatteschi, D.; Amoretti, G.; Caciuffo, R. *Phys. Rev. B* **2003**, *67*, 094405.

(7) Barra, A.-L.; Caneschi, A.; Cornia, A.; Gatteschi, D.; Gorini, L.; Heiniger, L.-P.; Sessoli, R.; Sorace, L. *J. Am. Chem. Soc.* **2007**, *129*, 10754–10762.

(8) Wilson, a.; Lawrence, J.; Yang, E.-C.; Nakano, M.; Hendrickson, D.; Hill, S. *Phys. Rev. B* **2006**, *74*, 140403.

(9) Liu, J.; del Barco, E.; Hill, S. *Phys. Rev. B* **2012**, *85*, 012406.

(10) Cornia, A.; Goovaerts, E. In *4th EFEPR Groups Conference Proceedings*; **2003**.

(11) Abragam, A.; Bleaney, B. *Electron Paramagnetic Resonance of Transition Ions*; Dover Publications: New York, **1986**.

(12) Bencini, A.; Gatteschi, D. *Electron Paramagnetic Resonance of Exchange Coupled Systems*; Springer-Verlag: Berlin, **1990**; p. 287.

(13) Stoll, S.; Schweiger, A. *J. Magn. Reson.* **2006**, *178*, 42–55.

(14) Gregoli, L.; Danieli, C.; Barra, A.-L.; Neugebauer, P.; Pellegrino, G.; Poneti, G.; Sessoli, R.; Cornia, A. *Chem. Eur. J.* **2009**, *15*, 6456–6467.

(15) Accorsi, S.; Barra, A. L.; Caneschi, A.; Chastanet, G.; Cornia, A.; Fabretti, A. C.; Gatteschi, D.; Mortalo, C.; Olivieri, E.; Parenti, F.; Rosa, P.; Sessoli, R.; Sorace, L.; Wernsdorfer, W.; Zobbi, L. *J. Am. Chem. Soc.* **2006**, *128*, 4742–4755.

Chapter 4

Fe_3V star-shaped SMMs

4.1 Vanadium-centred star-shaped cluster

As we have seen in the case of Fe_4 clusters, such single molecule magnets work in a very low temperature range. The blocking of the magnetisation, in tetrairon(III) systems, occurs below 1 K, making experiments extremely demanding. For this reason the synthetic work has focused on isostructural derivatives, trying to find a general and flexible route to allow the preparation of different heterometallic complexes. In fact, selective substitution of the central Fe^{III} ion with a different ion M may allow to tune the total spin value and the magnetic anisotropy of the cluster, thereby offering a viable route to increase the blocking temperature.

In the previous sections we have shown that a successful strategy has been developed with chromium(III) as its chemical inertness and stability support the formation of the oxygen hexacoordinated core adduct. This led to a Fe_3Cr cluster with an increased S value, with respect to tetrairon(III) analogue, but a reduced anisotropy D value. The balance of these two parameters brings to a tidy decrease of the energy barrier.

A way to improve the magnetic features of the star-shaped complexes is to substitute by the same modular synthetic approach the central position, with a different tripositive metal ion, characterised by a lower spin value that is antiferromagnetic coupled to the peripheral spins and by a larger magnetic anisotropy. More reactive vanadium(III) represents a good choice with its $S = 1$ and d^2 electronic configuration, which allows a significant orbital contribution.

The antiferromagnetic coupling of the $S = 1$ of V^{III} with the $S = 5/2$ each peripheral iron(III) leads to a semi integer S_{TOT} for the cluster Fe_3V ($S_{Fe3V} = 13/2$). Kramers theorem affirms that for a semi-integer spin the zero-field quantum tunnelling is prohibited.[1] The latter would be a great advantage for the magnetic dynamics, because it would slow down the relaxation process of such a molecule.

This part of the work was conducted primarily by the group of Prof Jaísa Fernandes Soares of Universidade Federal do Paraná (Curitiba, Brazil) and her PhD Student Kátia Molgero Westrup, who spent her research period abroad in our laboratories, collaborating with me, under the supervision of Prof Sessoli.

4.2 Synthetic strategy for Fe_3VL^{Et}

The synthetic route described in section 2.2 was exactly extended to the centred vanadium(III) cluster and is resumed in Scheme 4.1. The difference, in this case, depends on the higher reactivity of V^{III} ion with respect to Cr^{III}. The exclusion of moisture and, above all, air has to be strictly maintained for the entire synthetic process, to avoid oxidation of V^{III}.

Step I

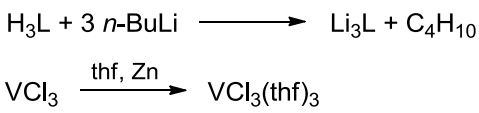

Step II

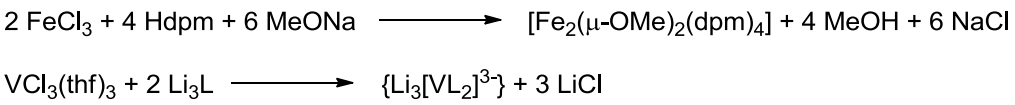

Step III

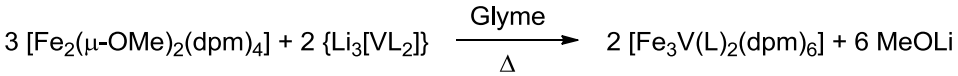

Scheme 4.1: Synthetic scheme for Fe_3VL^{Et}.

The preparation of Fe_3VL^{Et} produces also a Fe_4 impurity in the crystal of the product. Generally Fe_4:Fe_3V ratio in the final product varies depending on reaction and recrystallisation conditions, because the formation of tetrairon(III) complex takes place only during the crystallisation phase.

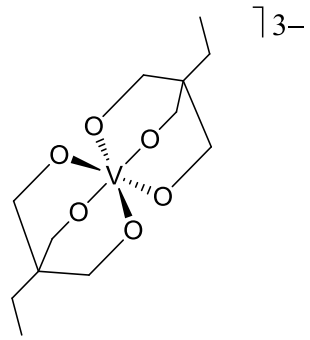

Figure 4.1: Representation of $[V(L^{Et})_2]^{3-}$ core. Only H_3L^{Et} ligand was used.

In order to determine the magnetic parameters of such cluster, from AC and DC magnetic measurements, the contribution of Fe_4L^{Et} has to be subtracted. For this reason the latter complex has also been synthesised as reported below.

4.3.1 Syntheses

The $[Fe_3V(L^{Et})_2(dpm)_6]$ can be handled in air in the solid state for several days without detectable change, but it is air-sensitive in solution. Accordingly, its synthesis and some of the spectroscopic analyses (FTIR and ^1H NMR) were carried out under high purity N_2 atmosphere.

Anhydrous vanadium(III) chloride and iron(III) chloride, dipivaloylmethane and *n*-butyllithium (1.6 M solution in hexanes) were purchased from Aldrich and used without additional purification. H_3L^{Et} (2-ethyl-2-(hydroxymethyl)-propane-1,3-diol), also supplied by Aldrich, was recrystallised in high yield from 1:1 dry mixture thf/toluene, solvents (Aldrich and Vetec) were dried by standard procedures[2] and distilled under N_2 prior to use. $[VCl_3(thf)_3]$[3] and $[Fe_2(OMe)_2(dpm)_4]$[4] were prepared by published methods.

$[Fe_3V(L^{Et})_2(dpm)_6]$

Step 1 A solution of H_3L^{Et} (265 mg, 1.98 mmol) in 30 ml of cold thf (0°C) received the dropwise addition of 5.93 mmol of n-butyl-lithium (3.70 ml, 1.6 M in hexanes). The resulting white suspension was kept stirring at 0°C for 5h and then filtered to give a quantitative yield of the tripodal lithium alkoxide Li_3L^{Et}. The white solid was dried under vacuum and immediately used in the following reaction step. **Step 2** Solid $[VCl_3(thf)_3]$ (369 mg, 0.989 mmol) was slowly extracted over a period of 40h into a boiling suspension of Li_3L^{Et} (300 mg, 1.98 mmol) in 120 ml of glyme. This produced a beige/light-brown suspension that was added, in **Step 3** To an orange suspension of $[Fe_2(OMe)_2(dpm)_4]$ (1.33 g, 1.46 mmol) in 50 ml of glyme. A greenish-brown solution was obtained as soon as the resulting mixture was heated to the boiling point, and it was then kept under reflux for 5h. After this period the hot reaction mixture was filtered, producing 0.64 g of an olive-green microcrystalline solid mixed with a white contaminant (possibly LiCl and LiOMe). The filtrate was cooled down to -20°C to give a second crop (0.12 g) of olive-green crystals (Fe_3VL^{Et}[c]) with a small amount of white powder.

The first mass of solid (0.64 g) was extracted with 175 ml of hexanes in a glove-box. The dark green extract was submitted to vapour diffusion of glyme over a period of three weeks. From the crystallisation chambers, 0.41g of olive-green crystals (Fe_3VL^{Et}[b]) were isolated by filtration and dried under vacuum. Total yield (Fe_3VL^{Et}[b]+ Fe_3VL^{Et}[c]): 0.53 g (*ca.* 34 %). Found for Fe_3VL^{Et}[b]: C, 59.28; H, 8.68; V, 2.41; Fe, 11.77%. Calc. for $C_{78}H_{136}O_{18}VFe_3$: C, 59.58; H, 8.67; V, 3.22; Fe, 10.60 %. Fe:V = 4.45 (mol/mol) ⇒ 73.3 w% of Fe_3V in Fe_3VL^{Et}[b].

An identical procedure with reaction time halved to 20h in Step 2 gave crystals of Fe_3VL^{Et}[b] with only a slightly lower content of V (70.5 w% of Fe_3V; yield = 32%). However, when recrystallisation was carried out in air, sample Fe_3VL^{Et}[a], the content of Fe_3V dropped to 46.3 w%; yield =15%.

$[Fe_4(L^{Et})_2(dpm)_6]$

The complex was prepared from 498 mg (0.55 mmol) of $[Fe_2(OMe)_2(dpm)_4]$ dissolved in 30 ml of a 1:2 methanol/diethyl ether mixture. Anhydrous $FeCl_3$ (60 mg, 0.37 mmol) was then added to this solution, which changed colour from yellow-orange to dark red. After 10min, the mixture received the addition of 1.1 mmol of MeONa (methanolic solution) and, after further 30min, of a solution of H_3L^{Et} (99 mg, 0.74 mmol) in 90 ml of methanol/diethyl ether (1:5). The mixture was left stirring at 25°C for 17h, then the orange precipitate was collected by filtration and washed with 5 ml of *n*-hexane. The solid was then redissolved in 40 ml of diethyl ether, filtered and submitted to vapour diffusion of methanol (400 ml). After five days, small red crystals were isolated. The powder x-ray diffraction pattern (Figure 4.2) confirmed that Fe_4L^{Et} is isomorphous to Fe_3VL^{Et}**.** Final yield of Fe_4L^{Et}: 280 mg, 48%.

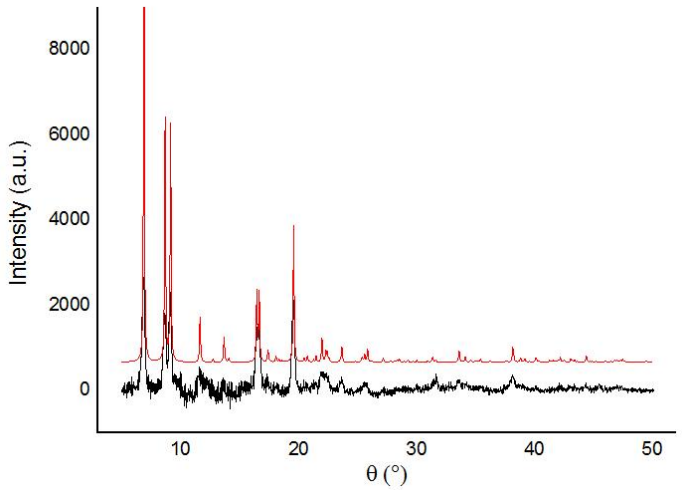

Figure 4.2: Comparison of the powder X-ray diffractograms of Fe_4L^{Et} (black line) and Fe_3VL^{Et}[a] (red line). The latter was calculated from the respective Crystallographic Data File (cif) deposited with the Cambridge Crystallographic Data Centre (CCDC) under the reference number 968842

4.4 Characterisations

4.4.1 Stability in solution

Recrystallisation of the olive-green, microcrystalline solid Fe_3VL^{Et}[c] precipitated after step 3, was necessary to provide analytically pure $[Fe_3V(L^{Et})_2(dpm)_6]$, because of the observed contamination with LiCl and LiOMe. However, despite the fairly high resistance of this olive-green product to manipulation in air in the solid state, it has proven highly labile in solution, giving an irreversible elimination of V^{III} from the tetranuclear aggregate, as discussed below.

Sample	**Fe_3VL^{Et} : $Fe_{4L}{}^{Et}$ (w%)**	**Preparation / recrystallisation conditions**
Fe_3VL^{Et}[a]	46.3:53.7	N_2, 20h (step 2) / air
Fe_3VL^{Et}[b]	73.3:26.7	N_2, 40h (step 2) / N_2
Fe_3VL^{Et}[c]	ND[(a)]	N_2, 40h (step 2) / *not recrystallised*
Fe_4L^{Et}	0:100	Air / air

Table 4.1: [a)] Not determined. The sample was not analysed for metal contents because of small contamination with LiCl and LiOMe. ^{1}H-NMR and AC susceptibility measurements indicate pure Fe_3VL^{Et}.

Recrystallisations were initially performed in air, giving homogeneous crops of clean rhombohedral prisms of which product Fe_3VL^{Et}[a] is an example (Table 4.1). Despite the typical FTIR spectra (Figure 4.3), which confirmed the propeller-like topology,[5] ^{1}H-NMR spectroscopy, metal content determination and magnetic susceptibility measurements indicated the presence of variable levels of co-crystallisation with the homometallic analogue. The relative proportion of the Fe_3V and Fe_4 complexes in the crystal lattice was found to depend on the effective molar ratio of iron(III) ions to the vanadium core in step 3 and on recrystallisation conditions.

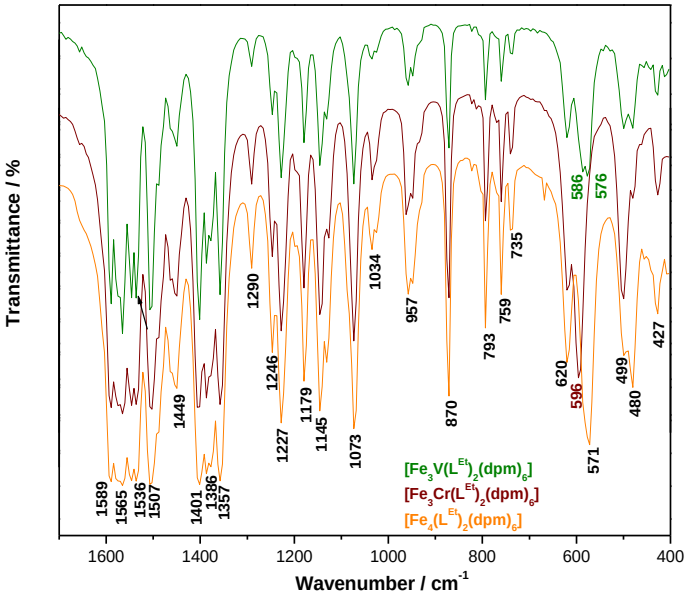

Figure 4.3: Comparison of the FTIR spectra (KBr pellets) registered for products Fe_3VL^{Et}[a] (green line), Fe_4L^{Et} (orange line) and Fe_3CrL^{Et} (brown-reddish line), in the 400-1700 cm^{-1} region.

In an attempt to gain further insight, recrystallisations were then performed under N_2, giving samples Fe_3VL^{Et}[b] with a much higher Fe_3V content (Table 4.1 and Table 4.2).

Product	**Element**	**C**	**H**	**Fe**	**V**	**Fe_3VL^{Et}:Fe_4L^{Et} (w%)**
	% Expected for Fe_3VL^{Et}	59.28	8.67	10.60	3.22	-------
Fe_3VL^{Et}[a]	% Found	59.47	8.70	12.05	1.44	46.3 : 53.7
Fe_3VL^{Et}[b] (20h reaction, step 2)	% Found	58.62	9.23	11.52	2.25	70.5 : 29.5
Fe_3VL^{Et}[b] (40h reaction, step 2)	% Found	59.28	8.68	11.77	2.41	73.3 : 26.7

Table 4.2

^{1}H-NMR spectra registered in air on freshly-prepared C_6D_6 solutions of Fe_3VL^{Et}[b] evidenced the presence of signals at 11.2 and 10.3 ppm, assigned to vanadium(III)-centred Fe_3V and Fe_4, respectively (Figure 4.4). In fact, the observed chemical shifts are in the range expected for *tert*-butyl hydrogens of iron(III)-bound dpm ligands. Such nuclei were found to resonate around 12.7, 10.3 and 8.8 ppm in diethylether solution of $[Fe(dpm)_3]$, $[Fe_4(OMe)_6(dpm)_6]$ and $[Fe_2(OMe)_2(dpm)_4]$, reflecting the

decreasing unpaired spin density on the iron(III) centres (data from ^{2}H NMR).[6] As reported earlier,[2–4,7–10] the identity of the paramagnetic transition metal ion has a strong influence on the chemical shift of β-diketonate hydrogen atoms, due to different degrees of spin delocalisation into ligand orbitals and dipolar contributions to the paramagnetic ^{1}H-NMR shifts.

Indeed, *tert*-butyl hydrogen nucleii resonate at 2.6 ppm in the dimer $[V_2(OMe)_2(dpm)_4]$ (Figure 4.5). As no signal attributable to vanadium(III)-bound dpm could be found in any of the ^{1}H-NMR spectra registered in this work, we conclude that the heterometallic complex is exclusively vanadium(III)-centred.

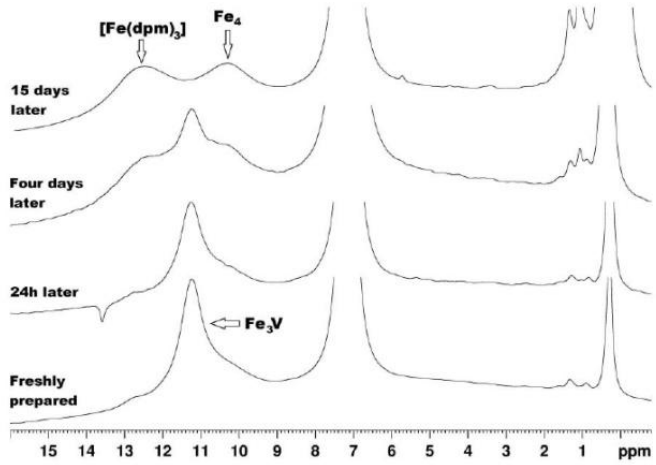

Figure 4.4: ^{1}H-NMR spectra (400.13 MHz) recorded on a C_6D_6 solution of Fe_3VL^{Et}[b] (*ca.* 2.5 mmol l^{-1}) at 303 K. The NMR sample was prepared and kept in air. The addition of tms to the solution was carried out after the fourth day of analysis. Peaks in the low frequency region are due to free Hdpm (1.07 ppm), silicone grease (0.29 ppm), tms (0 ppm)and a small amount of hexane from the recrystallisation mixture (0.89 and 1.40 ppm). The folded peak at *ca.* 13.7 ppm is a quadrature detection artefact. The top two spectra were vertically expanded to improve visualisation of the broad, high frequency signals.

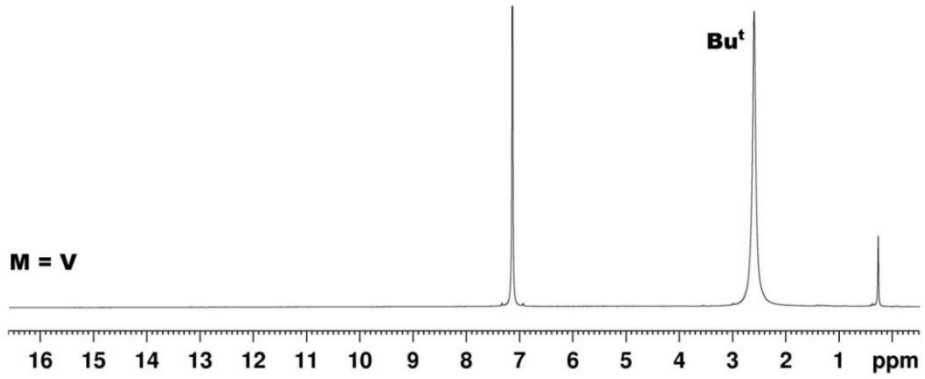

Figure 4.5: ^{1}H-NMR spectra (400.13 MHz) recorded from a freshly prepared C_6D_6 solution of $[V_2(\mu\text{-OMe})_2(dpm)_4]$ at 303 K.

Noticeably, according to the ^{1}H-NMR spectra of its C_6D_6 solutions freshly-prepared under nitrogen, crude reaction product Fe_3VL^{Et}[c] contains virtually no Fe_4 species (Figure 4.6). This result is fully corroborated by AC magnetic susceptibility measurements (see section 4.4.4). Unfortunately, solubility constraints still led to the precipitation of diamagnetic Li-containing contaminants, so Fe_3VL^{Et}[c] cannot be considered a 100% pure product.

Stability studies were carried out by allowing solutions of Fe_3VL^{Et}[b] and Fe_3VL^{Et}[c] to age at room temperature for several days. The time evolution of the ^{1}H-NMR spectrum of Fe_3VL^{Et}[b] in air consists in a slight enhancement of the signal at 10.3 ppm, with concomitant disappearance of the peak at 11.2 ppm, which is progressively replaced by a new signal at 12.5 ppm (Figure 4.6). The latter is assigned to $[Fe(dpm)_3]$.[10] The final intensity ratio of the $[Fe(dpm)_3]$ and Fe_4 signals, together with the much faster intensity increase for the former, suggest that the tris(diketonate)iron(III) complex is the main decomposition product of Fe_3VL^{Et}. The observed, gradual loss of the heterometallic component is probably responsible for the relatively low vanadium content in Fe_3VL^{Et}[a], which was isolated after recrystallisation in air (Table 4.1).

Time-dependent ^{1}H-NMR studies on C_6D_6 solutions of Fe_3VL^{Et}[c] kept in screw-cap tubes under N_2, revealed again the progressive decrease in concentration of Fe_3V,with concomitant formation of $[Fe(dpm)_3]$ and of smaller amounts of Fe_4 (Figure 4.6). However, in these inert atmosphere conditions, the decomposition of the heterometallic complex was not complete, even after seven weeks of analysis. The unrelenting but slow loss of vanadium from the once-formed heterometallic Fe_3VL^{Et} can be related to contamination of the solutions by traces of O_2 and/or moisture during the

long storage, combined with the high oxophilicity and sensitivity of vanadium(III) to hydrolysis.[11–13] This is compatible with other findings on ligand redistribution and formation of homometallic products from mixed-metal alkoxide/β-diketonate complexes upon (micro)hydrolysis.[14]

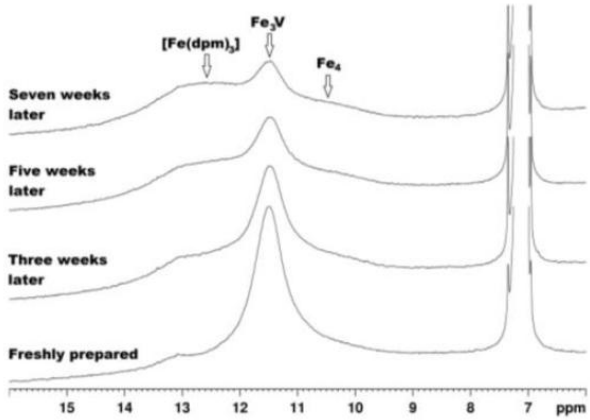

Figure 4.6: ^{1}H-NMR spectra (400.13 MHz) recorded on a C_6D_6 solution of Fe_3VL^{Et}[c] (*ca.* 2.5 mmol l^{-1}) at 303 K. The NMR sample was prepared and kept under N_2 during the whole period of analysis.

A similar decomposition to $[Fe(dpm)_3]$ is known for $[Fe_4(OMe)_6(dpm)_6]$, but Fe_4 and Fe_3Cr species supported by tripodal alkoxides are stable in solution.[6,15] Our observations agree with general kinetic data on the lability of metal(III) ions towards ligand substitution reactions (generally V^{III}> Fe^{III}>>> Cr^{III}),[16–19] and with the lower affinity of vanadium(III) for the hard tripodal alkoxide donors.

4.4.2 X-ray diffraction analysis

Similarly to chromium(III)-centred complex Fe_3CrL^{Et}, crystals of Fe_3VL^{Et} diffract only weakly, particularly at high angle. Such a result is presumably related to the crystallographic disorder affecting both the (dpm) *tert*-butyl groups and the ethyl substituent on the tripodal alkoxide. The molecular structure, shown in Figure 4.7, was determined on a batch of olive-green crystals of Fe_3VL^{Et}[a]. Distances and angles for Fe_3VL^{Et}[a] have thus to be regarded as weighted averages of the corresponding structural parameters for Fe_3V and Fe_4 species.

The comparison of structural data for the isomorphic crystals Fe_3VL^{Et}[a] and Fe_3CrL^{Et} (Table 4.3 and Table 4.4), collected at the same temperature, reveals that all distances (bonding or non-bonding) involving the central metal ion are larger in Fe_3VL^{Et}[a] than in its chromium(III) analogue, as could be anticipated from the larger effective ionic radii of six-coordinate V^{III} and Fe^{III} as compared to Cr^{III} (64.0, 64.5 and 61.5 pm respectively).[20,21]

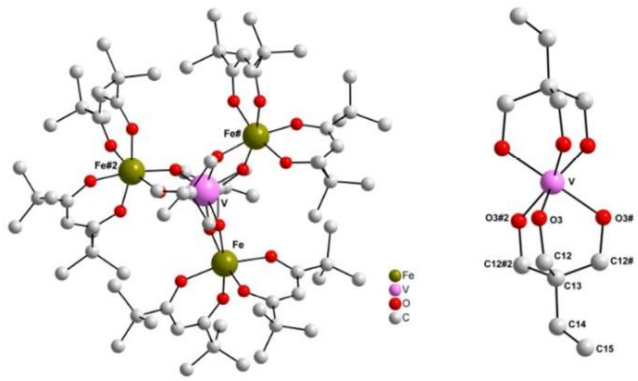

Figure 4.7: Representations of the molecular structure of $[Fe_3M(L^{Et})_2(dpm)_6]$ (M = V or Fe) in Fe_3VL^{Et}[a], with a simplified view of the M coordination sphere on the right. Trigonal, space group *R-3c:h*, a = B = 16.5321(4) Å, c = 58.0515(9) Å.

Bonding and non-bonding distances / Å	**Fe_3VL^{Et}[a] (M = V, Fe) (293K)**		**Fe_3CrL^{Et}(293K)**[15]	
$M_{central}$–$O_{tripodal}$	M–O(3)	1.977(2)	Cr–O(3)	1.949(3)
$M_{peripheral}$–$O_{tripodal}$	Fe–O(3)	1.963(2)	Fe–O(3)	1.963(3)
$M_{peripheral}$–$O_{diketonate}$	Fe–O^{dk} (av)	1.993(2)	Fe–O^{dk} (av)	1.996(3)
$M_{central}\cdots C_{central}$ [(a)]	M···C(13)	3.029	Cr···C(13)	2.986
$M_{central}\cdots M_{peripheral}$	M···Fe	3.075	Cr···Fe	3.023
$M_{peripheral}\cdots M_{peripheral}$	Fe···Fe	5.326	Fe···Fe	5.237
Helical pitch angle [(b)]/°	69.8		63.4	
Space group	*R*-3*c:h* (Trigonal)		*R*-3*c:h* (Trigonal)	
***D* / cm^{-1}**	-0.314 (Fe_3V); -0.432 (Fe_4)		-0.174	

Table 4.3: Abbreviations: av = average; O^{dk}= oxygen atom from β-diketonate; [(a)] $C_{central}$ = Central carbon atom in the tripodal alkoxide ligand, $[R\underline{C}(CH_2O)_3]^{3-}$; [(b)] Average dihedral angle between the planes defined by the $M_{central}(O)_2M_{peripheral}$ units and the four metal ions.

Bond lengths or non-bonding distances / Å		**Fe_3VL^{Et}[a] (M' = V, Fe)**	**Fe_3CrL^{Et}** [15]
$M_{central}\cdots M_{peripheral}$	M···Fe	3.075	3.023
$M_{peripheral}\cdots M_{peripheral}$	Fe···Fe	5.326	5.237
$M_{central}–O_{tripodal}$	M–O(3)	1.977(2)	1.949(3)
$M_{peripheral}–O_{tripodal}$	Fe–O(3)	1.963(2)	1.963(3)
$M_{peripheral}–O_{diketonate}$	Fe–O(1)	1.992(3)	1.996(3)
	Fe–O(2)	1.994(3)	1.986(4)
Angles / °		**Fe_3VL^{Et}[a] (M' = V, Fe)**	**Fe_3CrL^{Et}** [15]
$M_{peripheral}\cdots M_{central}\cdots M_{peripheral}$	Fe···M···Fe	120.00	120.00
$M_{peripheral}\cdots M_{peripheral}\cdots M_{peripheral}$	Fe···Fe···Fe	60.00	60.00
$O_{tripodal}–M_{central}–O_{tripodal}$	O(3)#1-M-O(3)#3	89.28(9)	90.80(11)
	O(3)#1-M-O(3)	77.05(13)	79.13(17)
	O(3)#1-M-O(3)#4	109.46(14)	101.46(17)
	O(3)#1-M-O(3)#5	156.35(14)	164.14(18)
$M_{central}–O_{tripodal}–M_{peripheral}$	M–O(3)–Fe	102.62(10)	101.20(12)
$O_{tripodal}–M_{peripheral}–O_{diketonate}$	O(3)–Fe–O(1)#1	93.03(10)	93.50(13)
	O(3)–Fe–O(2)#1	168.99(11)	170.93(14)
	O(3)–Fe–O(1)	100.22(11)	97.36(14)
	O(3)–Fe–O(2)	90.13(10)	92.58(13)
$O_{tripodal}–M_{peripheral}–O_{tripodal}$	O(3)#1–Fe–O(3)	77.72(13)	78.46(16)
$O_{diketonate}–M_{peripheral}–O_{diketonate}$	O(2)#1-Fe-O(1)	85.59(11)	84.47(15)
	O(2)#1-Fe-O(1)#1	85.62(11)	86.19(15)
	O(2)#1-Fe-O(2)	96.75(16)	96.4(2)
	O(1)Fe–O(1)#1	166.75(16)	166.0(2)

Table 4.4: Selected bond lengths and angles for $[Fe_3M'(L^{Et})_2(dpm)_6]$ (Fe_3VL^{Et}[a], M' = V, Fe) and for Fe_3CrL^{Et}.

4.4.3 Static magnetic characterisation

The temperature dependence of the product of the molar magnetic susceptibility with temperature, χT, for samples Fe_3VL^{Et}[b] and Fe_4L^{Et} are reported below.

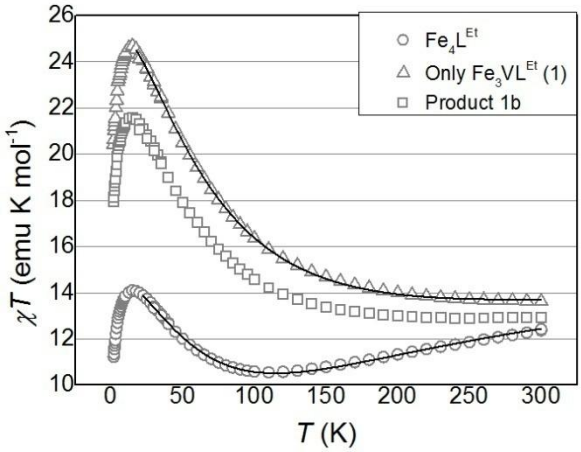

Figure 4.8: Plot of the temperature dependence of the molar magnetic susceptibility multiplied by T for compounds Fe_3VL^{Et}[b] and Fe_4L^{Et}, along with data for the Fe_3V species obtained by subtraction of the Fe_4 contribute. Solid curves provide the best fit to the data, as described in the text.

As Fe_3VL^{Et}[b] contains *ca.* 25% of Fe_4 in the crystal lattice, the data have been corrected based on the measured susceptibility of Fe_4L^{Et} and are reported in Figure 4.8 as open triangles. The room temperature value thus obtained is slightly smaller than that expected for three S = 5/2 and one S = 1 uncorrelated spins, 14.125 emu mol^{-1}, and thus suggests that also for V^{III} the coupling is antiferromagnetic. χT increases significantly below 150 K reaching 24.7 emu K mol^{-1}, which is not far from the expectation for S = 13/2 and g = 2 (24.375 emu K mol^{-1}).The χT vs T curves for Fe_3VL^{Et} and Fe_4L^{Et} were simulated assuming trigonal symmetry and using the Spin Hamiltonian:

$$\hat{H}_{ex} = J_1(\mathbf{S_M} \cdot \mathbf{S_{Fe1}} + \mathbf{S_M} \cdot \mathbf{S_{Fe2}} + \mathbf{S_M} \cdot \mathbf{S_{Fe3}}) + J_2(\mathbf{S_{Fe1}} \cdot \mathbf{S_{Fe2}} + \mathbf{S_{Fe1}} \cdot \mathbf{S_{Fe3}} + \mathbf{S_{Fe2}} \cdot \mathbf{S_{Fe3}})$$

Equation 4.1

where $\boldsymbol{S_M}$ labels the spin of the central ion. The resulting best fit parameters are reported in Table 4.5. It is to be stressed that the values obtained for Fe_3VL^{Et}[b], especially J_2, have to be considered with caution, since they are highly correlated to the percentage of Fe_4 species used to correct data for Fe_3VL^{Et}[b]. In any case, to the best of our knowledge these

are the only data hitherto reported on the coupling between V^{III} and Fe^{III} in molecular complexes. In this respect, while the exchange constant is significantly larger for the V^{III}-Fe^{III} pairs than for Fe^{III}-Fe^{III} pairs, the energies involved are comparable: the first excited states (S = 11/2 for Fe_3VL^{Et}, S = 4 for Fe_4L^{Et}) are indeed lying 44 cm^{-1} and 43 cm^{-1} above the ground state, respectively. On the contrary, a significant reduction of the exchange energy was observed in the case of Cr^{III}, see Table 4.5.[15]

	S	J_1 (cm^{-1})	J_2 (cm^{-1})	$g^{(a)}$	$D^{(a)}$ (cm^{-1})	$\Delta E^{(b)}$ (cm^{-1})
Fe_3V	13/2	25.7(4)	-2.45(7)	2.043(2)	-0.30	43
Fe_4	5	16.3(4)	-0.3(4)	2.003(1)	-0.42	44
Fe_3Cr[15]	6	13.4(4)	-0.4(2)	2.011(1)	-0.19	23

Table 4.5: Results of the fit of the static magnetic data.
(a) From EPR measurements; (b) Separation between the ground and first excited spin state.

For both Fe_3VL^{Et} and Fe_4L^{Et}, the decrease of χT at low temperature suggests the presence of zero-field splitting of the ground spin multiplet. For this reason, the isothermal magnetisation vs. field data at T = 1.9 K, 2.5 K and 4.5 K were measured and the curves (Figure 4.9 and Figure 4.10) reproduced assuming that only the ground state is populated and split by axial anisotropy according to:

$$\hat{H}_{zfs} = D\hat{S}_z^2 + \mu_B g\hat{\mathbf{S}}\cdot\hat{\mathbf{H}}$$

Equation 4.2

Also in this case the data for Fe_3VL^{Et}[b] have been corrected to account for the contribution of Fe_4 species in the crystal lattice. The best fit parameters are: g = 2.06(2) and D = -0.30(2) cm^{-1} for Fe_3VL^{Et}; g =1.927(9) and D = -0.43(2) cm^{-1} for Fe_4L^{Et}. Although the best-fit D value for Fe_3VL^{Et} correlates with the percentage of Fe_4 used for correction, our results evidence a sizeable negative zero field splitting, suggesting that Fe_3VL^{Et} could be a new heterometallic SMM.

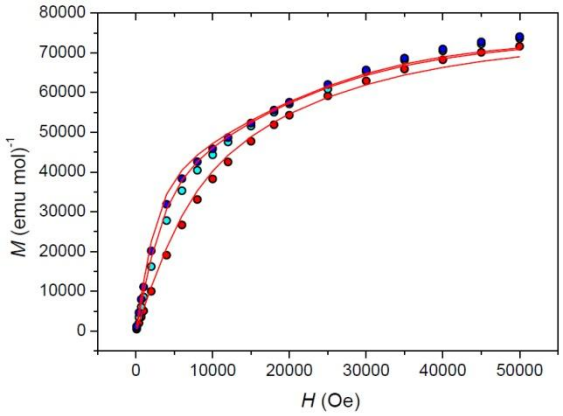

Figure 4.9: Experimental magnetisation *versus* magnetic field curves and corresponding fits at 1.9 K (blue), 2.5 K (cyan) and 4.5 K (red) for Fe_3VL^{Et}.

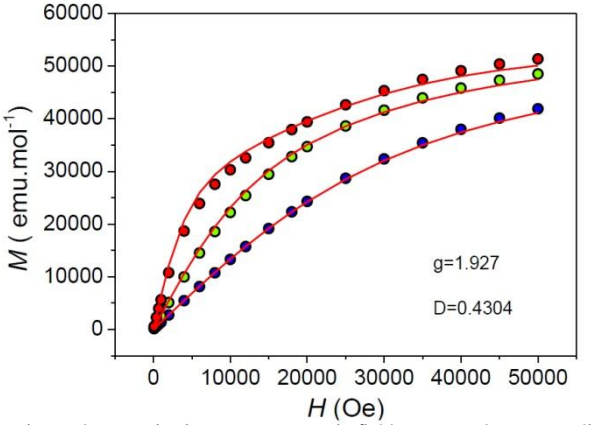

Figure 4.10: Experimental magnetisation *versus* magnetic field curves and corresponding fits at 2 K (red), 5 K (green) and 10 K (blue) for Fe_4L^{Et}.

4.4.4 Dynamic magnetic characterisation

The real and imaginary components of the susceptibility in alternating current (AC) for all investigated samples are reported in Figure 4.11 and Figre 4.12, respectively. An estimation of the anisotropy barrier Δ based on the D values extracted from static magnetisation data gives $\Delta/k_B = (|D|/k_B)(S^2\text{-}1/4)$= 18.1(12) K for Fe_3VL^{Et} and $\Delta/k_B = (|D|/k_B)S^2$= 15.5(7) K for Fe_4L^{Et}, thereby suggesting longer relaxation times for Fe_3VL^{Et} and thus the possibility to easily distinguish between the two species. This is well evident in the magnetically pure sample Fe_3VL^{Et}[c], which shows peaks when plotting the imaginary component χ'' vs the frequency of the AC field (see Figure 4.12) at much lower frequencies than Fe_4L^{Et}. The recrystallised samples Fe_3VL^{Et}[b] shows instead two well resolved peaks which coincide with those observed for the two magnetically pure samples. The analysis of the data was performed using the extended Debye model[22] to take into account a narrow distribution of relaxation times, and assuming two different relaxing species. The weight of the two species is well in agreement with the estimated Fe_3V:Fe_4 ratio, thus confirming the hypothesis of a co-crystallisation of the two species without any metal scrambling.

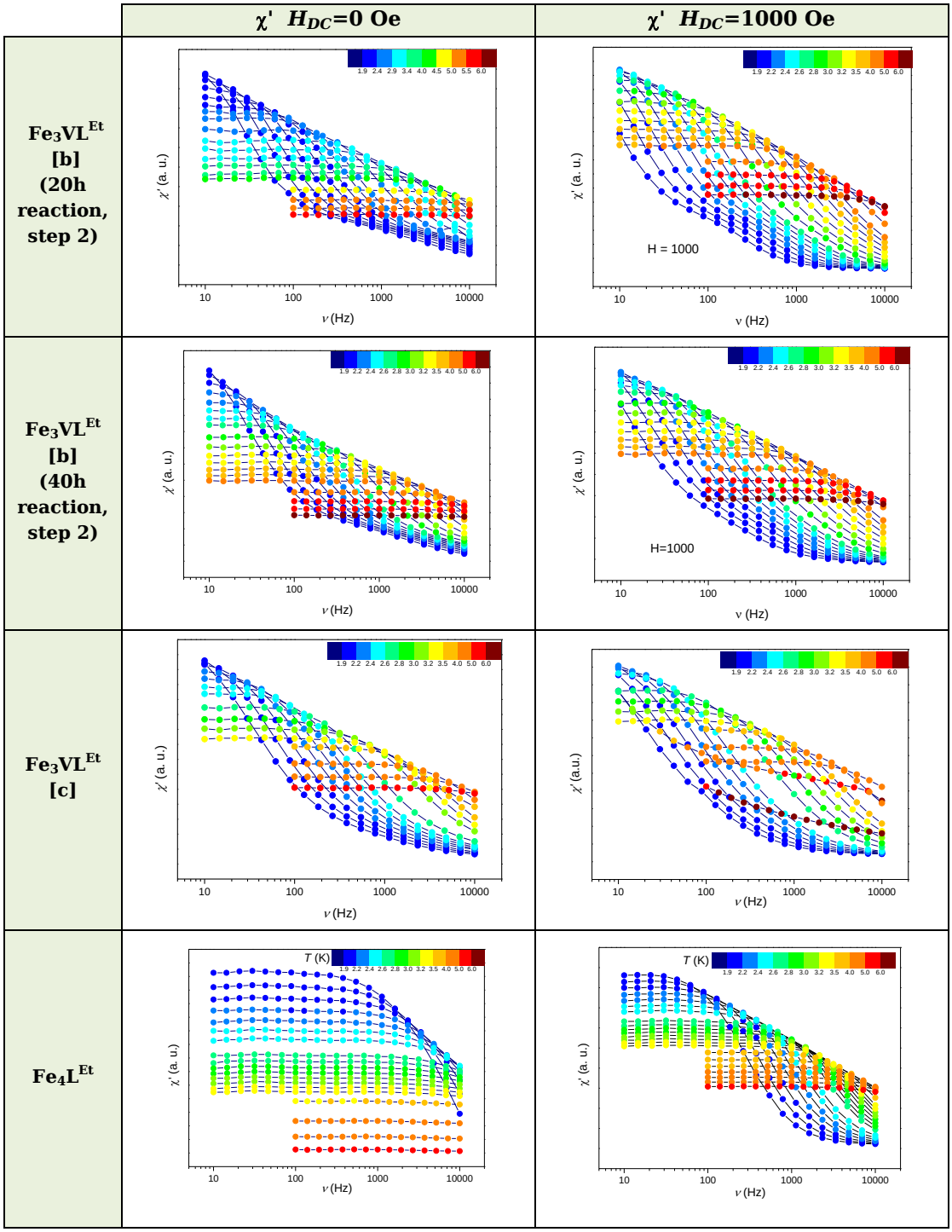

Figure 4.11: Real component of the susceptibility (χ') as a function of frequency in different temperatures (color code in the insets) for all the studied compounds without and with an applied DC field.

	χ'' H_{DC}=0 Oe	χ'' H_{DC}=1000 Oe
Fe_3VL^{Et} [b] (20h reaction, step 2)	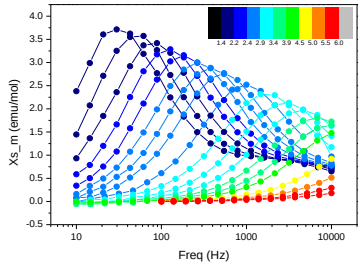	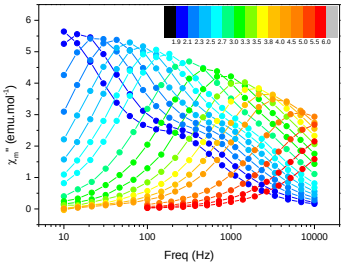
Fe_3VL^{Et} [b] (40h reaction, step 2)	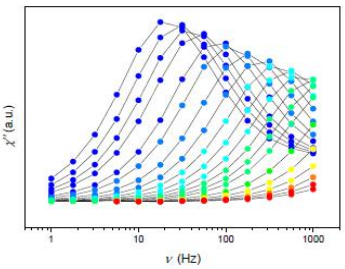	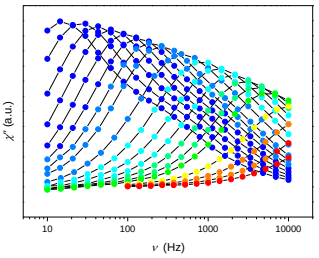
Fe_3VL^{Et} [c]	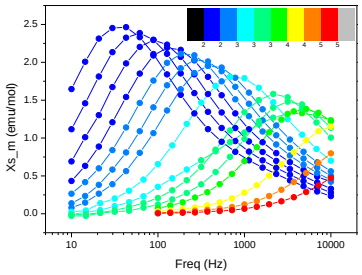	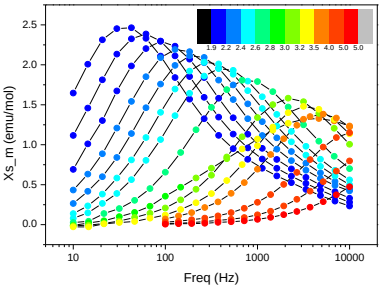
Fe_4L^{Et}	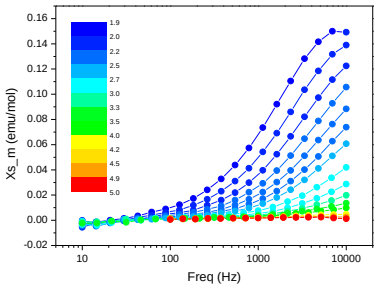	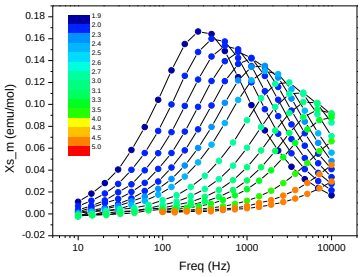

Figure 4.12: Imaginary component of the susceptibility (χ") as a function of frequency in different temperatures (colour code in the insets) for all the studied compounds without and with an applied DC field.

It is interesting to notice that the two species exhibit also a different effect of the application of a static magnetic field. While a significant shift of the peaks to lower frequencies is observed for Fe_4L^{Et} when a 1 kOe static field is applied, almost no effect is visible for the Fe_3VL^{Et} species.

The extracted relaxation times, τ, in both zero and static magnetic field, are reported in Figure 4.13. A substantially linear behaviour is observed in all cases when plotting the data as $\ln(\tau)$ vs $1/T$, *i.e.* the relaxation time follows Arrhenius law $\tau = \tau_0 \exp(\Delta/k_BT)$. The tetrairon(III) complex Fe_4L^{Et} exhibits a more pronounced effect of the static applied field, with Δ/k_B= 8.75(1) K and τ_0 = 2.12(4) 10^{-7} s at H_{DC} = 0, but Δ/k_B= 14.22(5) K and τ_0 = 2.96(7)10^{-7} s at H_{DC} = 1 kOe. The latter value of Δ agrees well with the estimated anisotropy barrier and the efficient suppression of the tunnel mechanism when applying a static field. In contrast, compound Fe_3VL^{Et}[c] shows an enhanced anisotropy barrier in both zero and applied field, with Δ/k_B = 20.6(2) K and τ_0 = 0.9(1) 10^{-7} s at H_{DC} = 0, and Δ/k_B = 20.8(4) K and τ_0 = 1.2(2) 10^{-7} s at H_{DC} = 1 kOe. Furthermore, the height of the anisotropy barrier agrees well with the estimate based on static magnetisation data.

The AC susceptibility of solid solution Fe_3VL^{Et}[b] was analysed taking into account the presence of two species and also a distribution of relaxation times. To reduce the number of parameters, a unique α value was used to describe the width of the distribution for the two species. Fe_3V complexes in Fe_3VL^{Et}[b] were found to relax at a slightly increased rate than in Fe_3VL^{Et}[c], with Δ/k_B = 19.3 K, and τ_0 = 1.910^{-7} s in zero field. These small differences can either be due to the different simulation processes or to the presence of the fast relaxing Fe_4 spins, whose fluctuating magnetic moments can promote a faster relaxation of the heterometallic species.

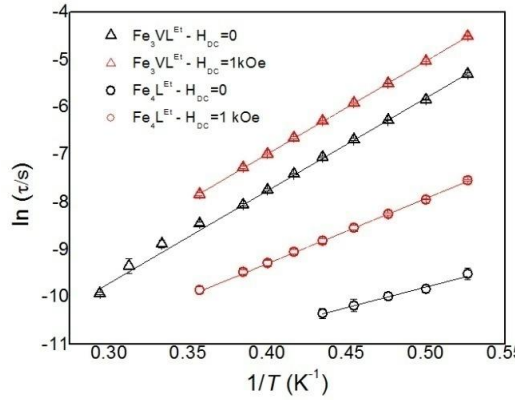

Figure 4.13: Temperature dependence of the relaxation time for Fe_3VL^{Et}[c] and Fe_4L^{Et} in zero and 1 kOe static field and corresponding Arrhenius fit.

4.4.5 Low temperature magnetic characterisation

The significantly different magnetic relaxation found in Fe_3VL^{Et} and Fe_4L^{Et}, and in particular the strongly reduced tunnelling efficiency in Fe_3VL^{Et}, prompted us to further investigate magnetic behaviour at sub-kelvin temperatures. In this case the solid solution Fe_3VL^{Et}[b] was employed to directly compare the magnetisation dynamics in the same conditions. All the measurements were carried out by Dr. Martin Jackson and Prof. Carley Paulsen of the Institut Néel CNRS & Université J. Fourier, in Grenoble.

First, AC susceptibility was measured collecting data at a restricted number of frequencies in the low temperature regime. The data, presented in Figure 4.14, confirmed the presence of two different relaxing species. The extracted relaxation times (Figure 4.15) evidence Arrhenius behaviour for Fe_3V species, with a barrier only slightly reduced compared to high temperature data, Δ/k_B = 19.3 (1) K. Instead, a more pronounced effect of tunnelling is detected for Fe_4 species, as the estimated energy barrier is reduced to Δ/k_B = 4.9(1) K.

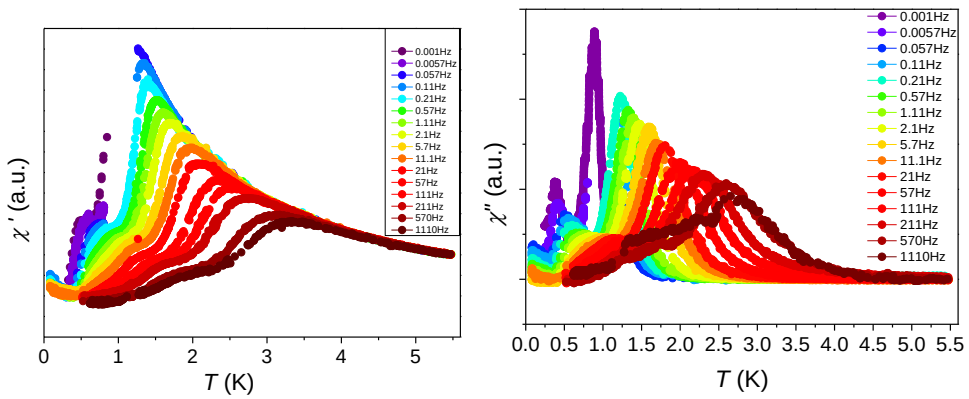

Figure 4.14: Real (left) and imaginary (right) parts of the magnetic susceptibility as a function of the temperature for frequencies from 0.001 to 1110 Hz, measured on product Fe_3VL^{Et}[b].

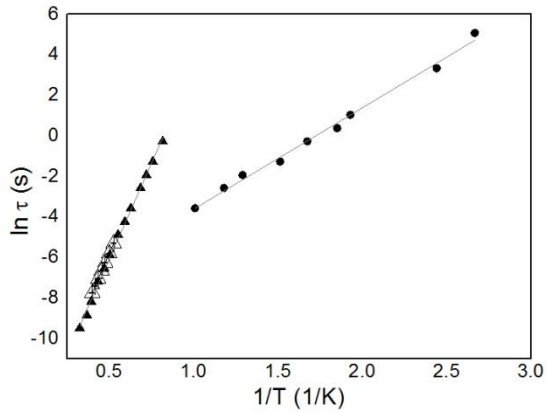

Figure 4.15: Arrhenius plot of the relaxation time τ versus $1/T$ for product Fe_3VL^{Et}[b] containing Fe_3VL^{Et} (triangles) and Fe_4L^{Et} (circles) from PPMS (empty dots) and low temperature SQUID measurements (full dots).

Thermomagnetic as well as magnetic hysteresis data were collected to explore relaxation times longer than those detectable by AC susceptibility studies. In the first case, the blocking temperature T_B is determined by measuring the temperature dependence of the magnetisation as the sample is cooled in zero field (ZFC) or in an applied static field (FC). T_B is then assumed to correspond to the cusp in the ZFC curve, which for SMMs is almost coincident with the temperature at which the two curves bifurcate due to the irreversible behaviour. T_B is not a univocally defined parameter as it depends on the cooling rate, which is however the same here for Fe_3V and Fe_4 species in the solid solution Fe_3VL^{Et}[b].

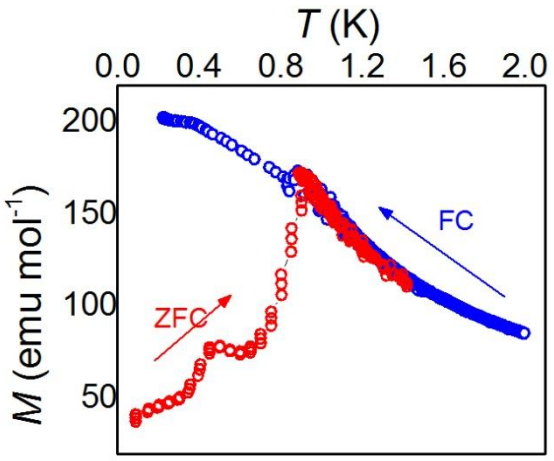

Figure 4.16: Magnetisation as a function of temperature, measured in heating mode after a zero field cooling (ZFC) or in cooling mode with applied field (FC). All measurements were performed in a 10 Oe magnetic field.

The ZFC curve of Fe_3VL^{Et}[b] (Figure 4.16) shows a distinct maximum around 0.92 K and a less pronounced peak at 0.47 K. The two blocking temperatures agree well with those expected on the basis of the Arrhenius parameters extracted from AC data, which yield T_B = 0.99 K and 0.44 K for Fe_3VL^{Et} and Fe_4L^{Et}, respectively, assuming an experimental characteristic time of 100 s.

Magnetic hysteresis cycles were also recorded for the same sample at variable temperature and the results are shown in Figure 4.17. The hysteresis loops become practically temperature independent below 0.35 K. More relevant for our investigation is that a significant remnant magnetisation, amounting to ca. 75% of the magnetisation extrapolated to zero field, is observed at low temperatures, with a coercive field of ca. 5 kOe. It is interesting to notice that powder samples of Fe_4 SMMs are characterised by a butterfly-shaped hysteresis with almost no remnant magnetisation, as a consequence of the fast tunnelling in zero field.[23,24] The small step observed in Figure 4.17 in zero field thus well accounts for the amount of Fe_4 species contained in Fe_3VL^{Et}[b]. The observation of a large remnant magnetisation for Fe_3V confirms that zero field tunnelling is dramatically reduced, as already suggested by the AC susceptibility data, in agreement with Kramers degeneracy of this half-integer spin state.[22,25]

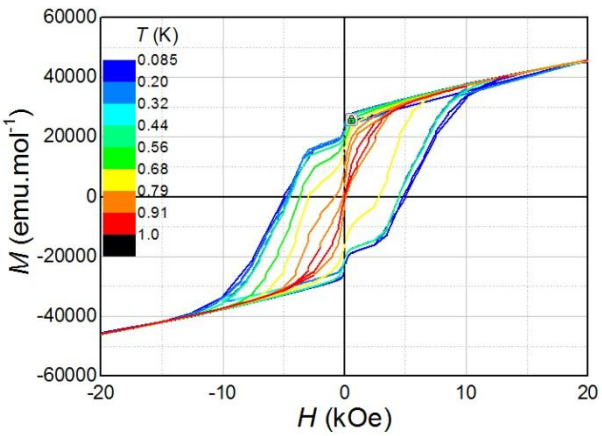

Figure 4.17: Magnetic hysteresis curves recorded on Fe_3VL^{Et}[b] at different temperatures.

4.4.6 Electron Paramagnetic Resonance

The anisotropy barrier observed in Fe_3VL^{Et} is the highest so far reported for tetranuclear, propeller-like clusters of formula Fe_3M (where M = Fe^{III}, Cr^{III}, V^{III}).[6,7,15,26,27] The increase in the barrier height from Fe_4L^{Et} to Fe_3VL^{Et} is accompanied by a reduction of the *D* parameter (Table 4.5), which is more than counterbalanced by the higher ground spin value. At variance with this, the *D* parameter and the barrier height are both reduced in chromium(III)-centred complex Fe_3CrL^{Et}.[7]

To shed light on the role played by the orbitally degenerate d^2 configuration of the V^{III} central ion, thanks to Dr Sorace, we recorded W-band EPR spectra at ν= 94.13 GHz, which proved to be, as we saw in chapter 3, an excellent technique for the characterisation of homo- and heterometallic tetranuclear SMMs.[5,7,28] Since both chemical and magnetic characterisation (as discussed previously in this chapter) have unequivocally demonstrated the presence of both Fe_4 and Fe_3V species in Fe_3VL^{Et}[b] we sought a simplification of the EPR spectra by recording pseudo single-crystal patterns (Figure 4.18 and Figure 4.19) working on loose powders and exploiting the magnetic torque produced by the easy axis magnetic anisotropy.[29,30] While this approach precludes the determination of transverse terms in the Hamiltonian, it provides accurate determination of the zero-field splitting axial parameter, on which detailed magnetostructural correlations exist for this family of molecules.[11,12,14]

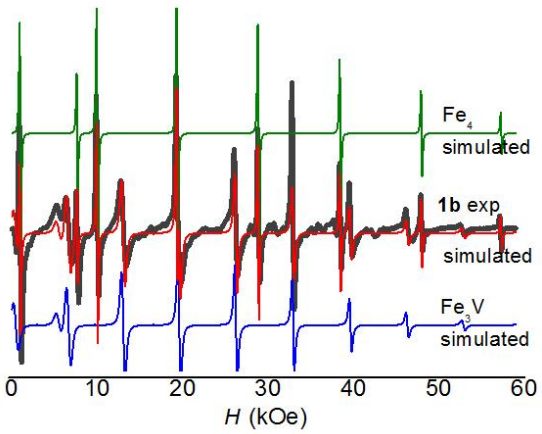

Figure 4.18: W-band EPR spectrum of sample Fe_3VL^{Et}[b] recorded at 20K (black line) along with simulated spectra of Fe_4 and Fe_3V. The red trace superimposed on the experimental spectrum is the best simulation with a 2.5:1 ratio between the two species.

Inspection of the spectra evidences two series of almost evenly spaced lines (with the exception of the structured line around 7 KOe) at all the investigated temperatures.

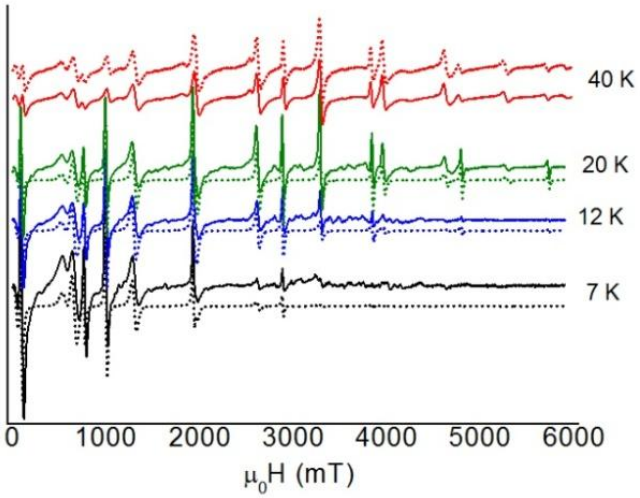

Figure 4.19: Oriented powder EPR spectra(W-band), measured on sample Fe_3VL^{Et}[b] at different temperatures. Dotted lines correspond to the simulated spectra considering a ratio of Fe_3V to Fe_4Et equal to 2.5:1 (71.5%:28.5% in weight).

The first series comprises lines spaced by 6700 Oe, with a transition occurring at g slightly higher than 2.00, and is then assigned to the ground S = 13/2 state of Fe_3V complex. The line spacing between consecutive lines, which is $\Delta H = 2D/g\mu_B$ for H applied parallel to the easy axis,[31,32] and the observation of a zero field resonance which can be assigned to the M_s = -11/2→-9/2 transition, provide for this cluster an estimate of D = -0.31 cm^{-1}, g_z = 2.04. In much the same way, the second series, for which consecutive lines are spaced by 9400 Oe, is attributed to the ground S = 5 state of Fe_4 species, with g_z = 2.00 and D = -0.44 cm^{-1}. These values were used as starting parameters for a complete simulation of the spectra, on the basis of the following spin Hamiltonian for the two species:

$$\hat{H}_{EPR} = g_z \mu_B \mu_0 \hat{H}_z \hat{S}_z + D\left[\hat{S}_z^2 - \frac{1}{3}S(S+1)\right] + B_4^0 \hat{O}_4^0$$

Equation 4.3

The best simulations of spectra at 7, 12, 20 and 40 K (Figure 4.19) resulted from the following parameters: S=13/2, D = (-0.314 ± 0.001) cm^{-1}, B_4^0 = (6 ± 1)×10^{-6} cm^{-1}, g_z= (2.043 ± 0.002) for Fe_3V; S=5, D= (-0.4320 ± 0.0002) cm^{-1}, B_4^0 = (8 ± 1)×10^{-6} cm^{-1} and g_z= (2.003 ± 0.001) for Fe_4. A satisfactory reproduction of the relative intensities required a 2.5:1 molar

ratio between Fe_3V and Fe_4 species, corresponding to *ca.* 70% of Fe_3V, in good agreement with chemical and magnetic characterisations of the same sample.

Our analysis of EPR spectra points to an anisotropy barrier of 19.0 K for Fe_3V, which compares well with the results of AC characterisation.

4.5 Origin of the magnetic anisotropy in Fe_3V cluster

To understand the role played by V^{III} in the magnetic anisotropy of the heteronuclear SMM it is necessary to deconvolute the different contributions to the zero field splitting tensor **D** of the cluster. In the strong exchange approximation the zero-field splitting of a tetranuclear Fe_3M cluster with spin state S is related to the microscopic anisotropic parameters (*i.e.* single-ion and pairwise - dipolar and anisotropic exchange - interactions) through eq.

$$\boldsymbol{D}_S = d_{Fe}\left(\boldsymbol{D}_{Fe(1)} + \boldsymbol{D}_{Fe(2)} + \boldsymbol{D}_{Fe(3)}\right) + d_M\boldsymbol{D}_M + d_{Fe,Fe}\sum_{i=1}^{3,j>i}\boldsymbol{D}_{Fe(i),Fe(j)} + d_{Fe,M}\sum_{i=1}^{3,j>i}\boldsymbol{D}_{Fe(i),M}$$

Equation 4.4

where $\boldsymbol{D}_{Fe(i)}$ and $\boldsymbol{D}_M$ are the single-ion anisotropy tensors, $\boldsymbol{D}_{Fe(i),Fe(j)}$ and $\boldsymbol{D}_{Fe(i),M}$ are the sum of dipolar and anisotropic exchange ones, while d_i and $d_{i,j}$ are projection coefficients calculated according to recursive relations.[33] The D_3 symmetry of the cluster imposes a number of constraints on the orientation of the tensors appearing in the last equation. In detail, $\boldsymbol{D}_M$ must be axial with its anisotropy axis oriented along the threefold symmetry axis. In addition, one of the principal directions of $\boldsymbol{D}_{Fe(i)}$ and of $\boldsymbol{D}_{Fe(i),M}$ must lie along the twofold axis joining *Fe(i)* with *M*.

Finally, the three tensors comprised in each $\boldsymbol{D}_{Fe(i)}$, $\boldsymbol{D}_{Fe(i),Fe(j)}$ and $\boldsymbol{D}_{Fe(i),M}$ set are symmetry related by a threefold rotation around the trigonal axis. On these bases, the latter tensorial relationship can be rewritten in scalar form:

$$D_S = \frac{3}{2}d_{Fe}\left[D_{Fe}(3\cos^2\beta - 1) + 3E_{Fe}\sin^2\beta\ \cos 2\gamma\right] + d_M D_M + D^{pair}$$

Equation 4.5

Here, the Euler angles α, β, γ (*zyz* convention) define the orientation of each local tensor eigenframe (*xyz*) with regard to the molecular reference frame (*XYZ*), defined with *Z* along the threefold symmetry axis, *Y* along the M-Fe(1) direction and *X* orthogonal to *Y* and *Z* (Figure 4.20). D_{Fe}, E_{Fe} are the anisotropy parameters of the peripheral ions, D_M is the axial zfs of the central ion and $D^{pair} = D^{dip} + D^{exc}$ is the sum of dipolar and anisotropic exchange contributions. There is now a large body of evidence that the single-ion anisotropy of Fe^{III} ions in these systems is of hard axis type with substantial rhombicity ($D_{Fe} \approx +0.7$ cm^{-1}, $E_{Fe} \approx 0.08$ cm^{-1}).

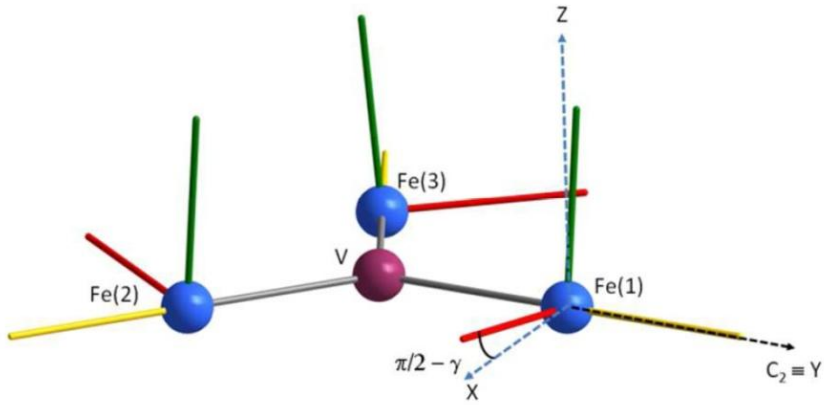

Figure 4.20: Assumed orientation of the anisotropy axes of the peripheral Fe^{III} ions with respect to the molecular *XYZ* frame (green: easy axis; red: hard axis; yellow: intermediate axis).

Moreover, the Fe^{III} site symmetry restrains γ to assume only two values, 0 or 90°, depending on whether the principal or the intermediate direction of $\boldsymbol{D}_{Fe(i),M}$ is found along M-Fe(*i*). On the other hand, there is no symmetry-imposed restriction on the angle β between *z* and *Z*; however, multiple evidences indicate that β has to be close to 90° and γ = 90°.[5,7,34]

When these values and the dipolar contribution calculated in the point dipole approximation (Table 4.6) are substituted in the last scalar equation, the combined contributions from vanadium(III) single ion anisotropy and anisotropic exchange to D_S are estimated to be *ca.* -0.14 cm^{-1}. If one neglects, as is often done, the anisotropic exchange contribution, a D_M value as large as -17 cm^{-1} is required to justify the observed anisotropy of the ground state, due to the low value of the projection coefficient d_M (Table 4.6).

Thanks to the seminal work of Tregenna-Piggott and co-workers[35,36] we can conclude that this is however an unreasonable value. In fact, the combined effect of spin-orbit coupling and trigonal distortion results for vanadium(III) either in a ground $^3A_2$ state with $D > 0$, or in an orbitally degenerate ground doublet when the ^3E state lies lowest (Figure 4.20). An easy-axis type anisotropy can arise only in the latter case, as a consequence of a marked rhombic distortion of the ligand field. This tends to group the six spinors of the ^3E state into two $S = 1$ orbital singlets, which can then be modelled by a rhombic zero field splitting Hamiltonian.[37,38] Such a scenario is however not consistent with the axial crystal symmetry nor with the magnetic properties of Fe_3VL^{Et}, which could be modelled with the assumption of an orbitally non-degenerate state for vanadium(III).

Finally, we note that the antisymmetric part of the exchange may also in principle contribute to the global zero field splitting of the cluster. The relevant term is proportional to $|\mathbf{d_{12}}|^2/J$, where $\mathbf{d_{12}}$ is the vector containing the antisymmetric contribution and J is the isotropic part of the exchange.[33] However, for each Fe^{III}-V^{III} pair, the combination of the antisymmetric and isotropic antiferromagnetic exchange would provide an axial tensor with $D_{Fe\text{-}V} > 0$ and principal axis oriented along the Fe-V direction, due to the C_2 symmetry of the Fe^{III}-V^{III} pair.[39] This would finally result in an additional contribution of hard axis type along the C_3 axis of the molecule when considering the negative sign of the projection coefficient $d_{Fe\text{-}V}$ (Table 4.6).

	$\mathbf{V^{III}}$	$\mathbf{Cr^{III}}$	$\mathbf{Fe^{III}}$
d_{Fe}	0.121429	0.138776	0.186813
d_{M}	0.008333	0.028571	0.128205
$d_{\mathrm{Fe,Fe}}$	0.151786	0.173469	0.233517
$d_{\mathrm{Fe,M}}$	-0.047222	-0.080952	-0.181624
c_{Fe}	0.37778	0.40476	0.47222
c_{M}	-0.13333	-0.21429	-0.41667
$D^{\mathrm{dip}}/\mathrm{cm}^{-1}$	-0.005	-0.0132	-0.0365

Table 4.6: Projection coefficients and calculated dipolar contribution to the anisotropy of the ground state in Fe_3M star-shaped molecules (M = V^{III}, Cr^{III}, Fe^{III}).

We are then left with a major role of the exchange contribution to the easy-axis anisotropy: on the basis of the projection coefficient $d_{Fe,V}$ and assuming $0 < D_{\mathrm{M}} < 10\ \mathrm{cm}^{-1}$, the exchange anisotropy is estimated to be of the order of 1-3 cm^{-1}. This is quite a large value when compared to other molecular systems for which anisotropic exchange has been reported,[40,41] and requires some discussion.

The magnitude of the anisotropic exchange contribution is inversely dependent on the square of the energy difference between the ground and first excited states, *e.g.* the trigonal splitting discussed above in the case of V^{III}. Thus the anisotropic exchange contribution to the diagonal terms of the $\boldsymbol{J}$ tensor can be evaluated as:[33]

$$J_{AB}^{\alpha\alpha} = \lambda_A^2 \frac{\left|\langle\varphi_A^0|\hat{L}_A^\alpha|\varphi_A^1\rangle\right|^2}{\Delta E_A^2}\langle\varphi_A^1\varphi_B^0|\hat{H}_{exc}|\varphi_A^1\varphi_B^0\rangle + \lambda_B^2 \frac{\left|\langle\varphi_B^0|\hat{L}_B^\alpha|\varphi_B^1\rangle\right|^2}{\Delta E_B^2}\langle\varphi_A^0\varphi_B^1|\hat{H}_{exc}|\varphi_A^0\varphi_B^1\rangle$$

Equation 4.6

where α = *x*, *y*, or *z*, A and B denote the two centres, *i.e.* V and Fe here, λ is the spin-orbit coupling constant, φ^0 and φ^1 are the ground and first excited state for a given centre, respectively. The matrix $\langle\varphi_A^1\varphi_B^0|\hat{H}_{exc}|\varphi_A^1\varphi_B^0\rangle$ represents the exchange interaction between the ground state of one centre and the excited state of the other one. An estimate of ΔE can be obtained by using the following relation:

$$g_z - g_e = -\lambda(2 + kP)\frac{P}{\Delta \mathrm{E}}$$

Equation 4.7

Here, P is a parameter ranging from 1 to 1.5, describing the strength of the ligand field and k is the orbital reduction factor. Fe^{III} is not expected to contribute much to exchange anisotropy, and its g values can be safely considered isotropic and close to 2. Thus equation for $J_{AB}^{\alpha\alpha}$ reduces to one term. The g_z value of V^{III} can be estimated by the experimentally determined g_z values for Fe_4 and Fe_3V molecules, on the basis of strong exchange approximation. Using next equation with the appropriate projection coefficients (Table 4.6).

$$g_S^z = 3c_{Fe}g_{Fe} + c_V g_V^z$$

Equation 4.8

This provides $g_V^z \approx 1.71$, which is at the lowest end of the reported literature values for vanadium(III)[41] (The quite small value for g_z may suggest a non-negligible role of the vibronic coupling,[42] which has been demonstrated to lead to a decrease of $g_{//}$ and to an increase of $g_\perp$ compared to the static case). Substituting in the last equation standard values of P = 1.25, k = 0.8 and λ = 75 cm^{-1} gives an estimated trigonal splitting for the vanadium ion of about 300 cm^{-1}, thus extremely small.

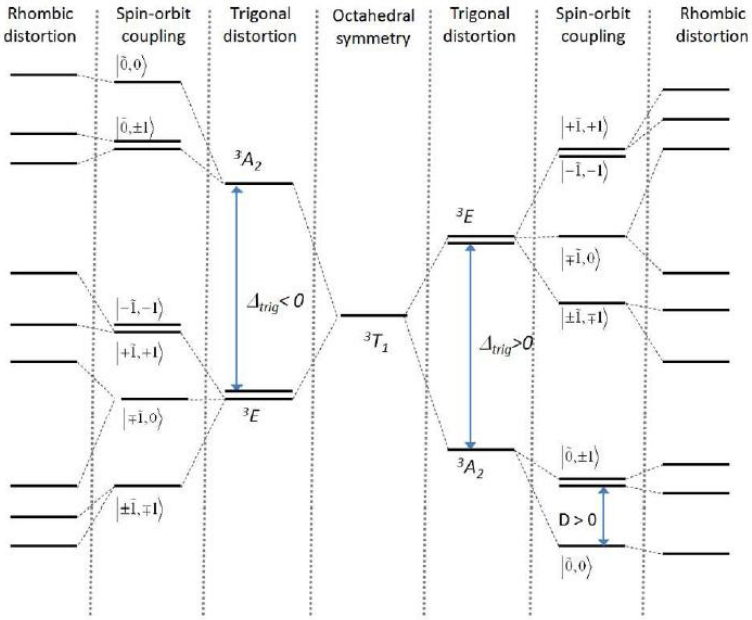

Figure 4.21: Effect of different perturbations over the ground $^3T_{1g}$ state of vanadium(III) in octahedral coordination.

Finally, despite the purely qualitative nature of these calculations and the complexity in obtaining an appropriate estimation of $\langle\varphi_A^1\varphi_B^0|\hat{H}_{exc}|\varphi_A^1\varphi_B^0\rangle$[43,44] these results suggest for the latter term a quite reasonable value of the order of 10 cm^{-1}, of opposite sign compared to the exchange in the ground state.

4.6 Conclusions

The extension of our novel synthetic route, developed to obtain heterometallic chromium centred star-shaped cluster, to vanadium(III) analogues was not straightforward due the limited stability of Fe_3V species in solution and their tendency to crystallise as solid solutions with Fe_4 complexes. These difficulties were overcome by an educated choice of reaction conditions and recrystallisation procedures. The incorporation of V^{III} results in a further increase of the ground spin value (S = 13/2), compared to achievement with Cr(III) (S = 6). Although V^{III} is expected to experience a single ion anisotropy as large as a few Kelvin, its contribution to the total anisotropy of the polynuclear system becomes negligible as the corresponding projection coefficient is close to zero. However, this effect is counterbalanced by exchange anisotropy which arises from the peculiar electronic structure of V^{III} in distorted octahedral coordination, thus affording an anisotropy barrier exceeding that of Fe_4 complexes, and resulting in the highest energy barrier for of Fe_3M single molecule magnets.

The SMM behaviour is further improved compared to both Fe_4 and Fe_3Cr families as the larger and half-integer spin value strongly reduces tunneling effects in zero field, yielding a significant remnant magnetisation. The latter is particularly appealing to further investigate these vanadium centred star-shaped derivatives, in particular when embedded in nanostructure.

At the same time this new synthetic strategy revealed to be of great potential for a rational chemical design of SMMs, and we plan to extend the same approach to other combinations of transition metal ions.

(1) Abragam, A.; Bleaney, B. *Electron Paramagnetic Resonance of Transition Ions*; Dover Publications: New York, **1986**.

(2) Armarego, W. L. .; Perrin, D. . *Purification of Laboratory Chemicals*; 4th ed.; Butterworth-Heinemann, **1997**; p. 544.

(3) L. E. Manzer, Joe Deaton, Paul Sharp, R. R. S. *Inorg. Synth.* **1982**, *21*, 135–140.

(4) Pearson, R. G. *J. Chem. Educ.* **1968**, *45*, 581–587.

(5) Sorace, L.; Boulon, M.-E.; Totaro, P.; Cornia, a.; Fernandes-Soares, J.; Sessoli, R. *Phys. Rev. B* **2013**, *88*, 104407.

(6) Accorsi, S.; Barra, A.-L.; Caneschi, A.; Chastanet, G.; Cornia, A.; Fabretti, A. C.; Gatteschi, D.; Mortalo, C.; Olivieri, E.; Parenti, F.; Rosa, P.; Sessoli, R.; Sorace, L.; Wernsdorfer, W.; Zobbi, L. *J. Am. Chem. Soc.* **2006**, *128*, 4742–4755.

(7) Tancini, E.; Rodriguez-Douton, M. J.; Sorace, L.; Barra, A.-L.; Sessoli, R.; Cornia, A. *Chem. Eur. J.* **2010**, *16*, 10482–10493.

(8) Mannini, M.; Tancini, E.; Sorace, L.; Sainctavit, P.; Arrio, M.-A.; Qian, Y.; Otero, E.; Chiappe, D.; Margheriti, L.; Cezar, J. C.; Sessoli, R.; Cornia, A. *Inorg. Chem.* **2011**, *50*, 2911–2917.

(9) Stoll, S.; Schweiger, A. *J. Magn. Reson.* **2006**, *178*, 42–55.

(10) Douglas Kissler, K.; Sheppard, S. K.; Eaton, G. R.; Eaton, S. S. *J. Magn. Reson.* **1985**, *63*, 74–87.

(11) Crans, D. C.; Smee, J. J.; Gaidamauskas, E.; Yang, L. *Chem. Rev.* **2004**, *104*, 849–902.

(12) Tidmarsh, I. S.; Scales, E.; Brearley, P. R.; Wolowska, J.; Sorace, L.; Caneschi, A.; Laye, R. H.; McInnes, E. J. L. *Inorg. Chem.* **2007**, *46*, 9743–9753.

(13) Slebodnick, C.; Hamstra, B. J.; Pecoraro, V. L. *Metal Sites in Proteins and Models: Phosphatases, Lewis Acids and Vanadium*; Hill, H. A. O.; Sadler, P. J.; Thomson, A. J., Eds.; Springer Berlin Heidelberg, **1997**; Vol. 89, pp. 51–108.

(14) Werndrup, P.; Verdenelli, M.; Chassagneux, F.; Parola, S.; Kessler, V. G. *J. Mater. Chem.* **2004**, *14*, 344–350.

(15) Totaro, P.; Westrup, K. C. M.; Boulon, M.-E.; Nunes, G. G.; Back, D. F.; Barison, A.; Ciattini, S.; Mannini, M.; Sorace, L.; Soares, J. F.; Cornia, A.; Sessoli, R. *Dalt. Trans.* **2013**, *42*, 4416–4426.

(16) Van Eldik, R. *Inorganic high pressure chemistry: kinetics and mechanisms*; Elsevier: Amsterdam, **1986**; p. 448.

(17) Langford, C. H.; Gray, H. B. *Ligand substitution processes*; New York, **1966**; p. 111.

(18) Hugi, A. D.; Helm, L.; Merbach, A. E. *Helv. Chim. Acta* **1985**, *68*, 508–521.

(19) Kazuo Saito, HIroaki Kido, A. N. *Coord. Chem. Rev.* **1990**, *100*, 427–452.

(20) Shannon, R. D.; Prewitt, C. T. *Acta Crystallogr. Sect. B Struct. Crystallogr. Cryst. Chem.* **1969**, *25*, 925–946.

(21) Shannon, R. D. *Acta Crystallogr. Sect. A* **1976**, *32*, 751–767.

(22) Gatteschi, D.; Sessoli, R.; Villain, J. *Molecular Nanomagnets*; Oxford University Press: Oxford, **2006**; p. 361.

(23) Mannini, M.; Pineider, F.; Danieli, C.; Totti, F.; Sorace, L.; Sainctavit, P.; Arrio, M.; Otero, E.; Joly, L.; Cezar, J. C.; Cornia, A.; Sessoli, R. *Nature* **2010**, *468*, 417–421.

(24) Mannini, M.; Pineider, F.; Sainctavit, P.; Joly, L.; Fraile-Rodríguez, A.; Arrio, M.-A.; Cartier dit Moulin, C.; Wernsdorfer, W.; Cornia, A.; Gatteschi, D.; Sessoli, R. *Adv. Mater.* **2009**, *21*, 167–171.

(25) Wernsdorfer, W.; Chakov, N.; Christou, G. *Phys. Rev. Lett.* **2005**, *95*, 037203.

(26) Gregoli, L.; Danieli, C.; Barra, A.-L.; Neugebauer, P.; Pellegrino, G.; Poneti, G.; Sessoli, R.; Cornia, A. *Chem. Eur. J.* **2009**, *15*, 6456–6467.

(27) Saalfrank, R. W.; Scheurer, A.; Bernt, I.; Heinemann, F. W.; Postnikov, A. V; Schünemann, V.; Trautwein, A. X.; Alam, M. S.; Rupp, H.; Müller, P. *Dalt. Trans.* **2006**, 2865–2874.

(28) Bouwen, A.; Caneschi, A.; Gatteschi, D.; Goovaerts, E.; Schoemaker, D.; Sorace, L.; Stefan, M. *J. Phys. Chem. B* **2001**, *105*, 2658–2663.

(29) Barra, A. L.; Caneschi, A.; Gatteschi, D.; Sessoli, R. *J. Am. Chem. Soc.* **1995**, *117*, 8855–8856.

(30) Aubin, S. M. J.; Sun, Z.; Pardi, L.; Krzystek, J.; Folting, K.; Brunel, L.; Rheingold, A. L.; Christou, G.; Hendrickson, D. N. *Inorg. Chem.* **1999**, *38*, 5329–5340.

(31) Barra, A.-L.; Brunel, L.-C.; Gatteschi, D.; Pardi, L.; Sessoli, R. *Acc. Chem. Res.* **1998**, *31*, 460–466.

(32) Gatteschi, D.; Barra, A. L.; Caneschi, A.; Cornia, A.; Sessoli, R.; Lorenzo, S. *Coord. Chem. Rev.* **2006**, *250*, 1514–1529.

(33) Bencini, A.; Gatteschi, D. *Electron Paramagnetic Resonance of Exchange Coupled Systems*; Springer-Verlag: Berlin, **1990**; p. 287.

(34) Vergnani, L.; Barra, A. L.; Neugebauer, P.; Rodriguez-Douton, M. J.; Sessoli, R.; Sorace, L.; Wernsdorfer, W.; Cornia, A. *Chem. Eur. J.* **2012**, *18*, 3390–3398.

(35) Tregenna-Piggott, P. L. W.; Weihe, H.; Bendix, J.; Barra, A.-L.; Güdel, H.-U. *Inorg. Chem.* **1999**, *38*, 5928–5929.

(36) Tregenna-Piggott, P. L. W.; Carver, G. *Inorg. Chem.* **2004**, *43*, 8061–8071.

(37) Kittilstved, K. R.; Sorgho, L. A.; Amstutz, N.; Tregenna-Piggott, P. L. W.; Hauser, A. *Inorg. Chem.* **2009**, *48*, 7750–7764.

(38) Kittilstved, K. R.; Hauser, A. *Coord. Chem. Rev.* **2010**, *254*, 2663–2676.

(39) Buckingham, A. D.; Pyykkö, P.; Robert, J. B. *Mol. Phys.* **1982**, *46*, 177–182.

(40) Piligkos, S.; Bill, E.; Collison, D.; McInnes, E. J. L.; Timco, G. a; Weihe, H.; Winpenny, R. E. P.; Neese, F. *J. Am. Chem. Soc.* **2007**, *129*, 760–761.

(41) Ter Heerdt, P.; Stefan, M.; Goovaerts, E.; Caneschi, A.; Cornia, A. *J. Magn. Reson.* **2006**, *179*, 29–37.

(42) Ayers, P. W.; Parr, R. G.; Pearson, R. G. *J. Chem. Phys.* **2006**, *124*, 194107.

(43) Kessler, E. M. V.; Schmitt, S.; van Wüllen, C. *J. Chem. Phys.* **2013**, *139*, 184110.

(44) Maurice, R.; Sivalingam, K.; Ganyushin, D.; Guihéry, N.; de Graaf, C.; Neese, F. *Inorg. Chem.* **2011**, *50*, 6229–6236.

Chapter 5

Substituting the peripheral metal(III) ions in star-shaped complexes

5.1 Introduction

As we have discussed in previous chapters, even nowadays all known SMMs work only at temperatures close to zero Kelvin.[1] For this reason, many efforts have been made in the last decades to raise up blocking temperatures of the magnetisation.[2–4] Such an objective could be reached by a rational synthetic effort to change the scaffold, in our case, of the star-shaped metal complex, playing, first of all, with the metal ions that build the molecule. The new synthetic route was refined using chromium(III) in the central position of the tetranuclear complex and, thanks to its inertness, the experimental operations are affordable and quite easy, as compared, for instance, to the use of vanadium(III). The new modular synthesis developed in the previous chapters gives an additional opportunity, which is to substitute the external iron(III) ions with, potentially, any other tripositive metal ion, thus allowing a modulation of the spin value and of the magnetic anisotropy.

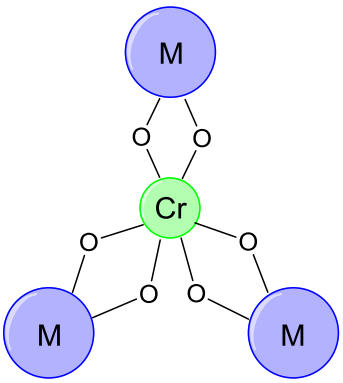

Figure 5.1: Schematic representation of a chromium centred star-shaped complex scaffold. M is a tripositive metal ion.

During my sojourn at the *Laboratório de Bioinorgânica* of *Universidade Federal do Paraná* in Curitiba (Brazil), where I worked under the supervision of Prof. Jaísa Fernandes Soares, the research program focused on the introduction of different tripositive metal ions (M^{III}) to build a CrM_3 star-shaped complex. In particular, the idea was to employ manganese(III) and terbium(III) in the external positions and a brief description of preliminary results will be the subject of this chapter.

Manganese(III) ($S = 2$) ions represent an interesting choice because the Jahn-Teller elongation of the octahedral geometry, typical of high spin d^4 ions, could promote an increase in molecular anisotropy, although it should be kept in mind that the overall anisotropy depends on the orientation of

the elongation axis of each Mn^{III} ion with respect to the three-fold symmetry axis of the cluster.

In the case of lanthanide ions, it would be possible to exploit their large spin-orbit coupling and large total angular momentum (J) to try and build highly anisotropic SMMs. However, differently from transition metal ions, which frequently have a maximum coordination number equal to 6, the lanthanides are characterised by a more extended coordination sphere, usually presenting 8- or 9-coordination for late lanthanide ions. In this case dpm ligands are not suitable, because three of them are likely to coordinate the lanthanide(III) ions forming a neutral species, while the star-shaped M_4 complexes usually employ $M(LL)_2^+$ peripheral units (LL = bidentate β-diketonates) to form a neutral complex with the central metal(III) ion. Although the +III oxidation state for all metal ions in these tetranuclear complexes is not mandatory, in any case the incorporation of lanthanide ions requires the entire synthetic strategy to be revisited, starting from changing the type of ligands for the external ions.

5.2 Synthesis of the manganese(III) dimeric starting material

If we consider the synthetic strategy usually employed to arrive at a star-shaped M_4 complex, the peripheral ions are introduced into the structure through a dimeric metal(III) starting material.[5–7] For a Fe_3ML complex (M: Cr^{III}, V^{III}; L: generic tripodal ligand) synthesised by the modular approach (as discussed in chapters 2 and 4), the star-shaped topology is achieved by reaction of the molecular core with $[Fe_2(\mu\text{-}OMe)_2(dpm)_4]$ (Scheme 5.1a). Alternatively, the same iron(III) dimer or its gallium(III) analogue $[Ga_2(\mu\text{-}OMe)_2(dpm)_4]$ have been used to place the respective metal ions at the external positions of the tetranuclear complex by reaction with $FeCl_3$,[5] $[CrCl_3(thf)_3]$ or $GaCl_3$[6] (Scheme 5.1b and c).

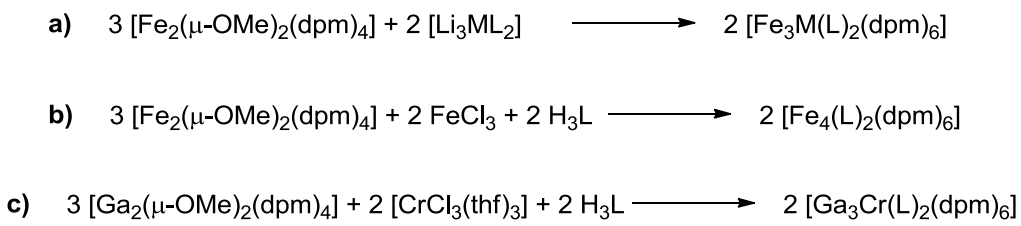

Scheme 5.1: Reaction scheme for different star-shaped compounds. Only the main products are emphasised.

In analogy to the cases exemplified above, we thought of building a similar synthetic route to place manganese(III) ions in the peripheral positions of the M_4 star-shaped complex. In order to do that, a Mn^{III} dimer had to be prepared. But, differently from the observed for iron, chromium and gallium, manganese trichloride ($MnCl_3$) is not commercially available. One of the most common Mn^{III} starting materials is $[Mn(dpm)_3]$, which is not suitable for our purposes because of its high stability and therefore low reactivity.[8–10] The easiest reported procedure to produce manganese(III) complexes is to start from a manganese(II) salt, $MnCl_2$ for example, and let it be oxidised by atmospheric oxygen during the reaction to prepare the desired complex.[11]

After numerous attempts, proper reaction conditions for the preparation of the manganese(III) diketonate dimer were determined.

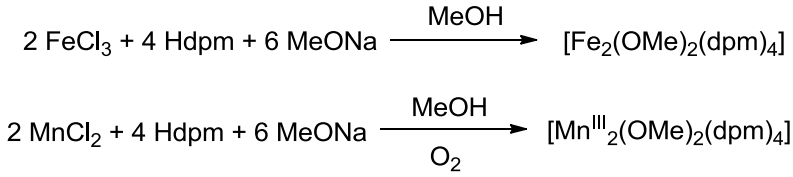

Scheme 5.2

As discussed above and shown in Scheme 5.2, differently from the case of iron(III), the starting material for the manganese(III) dimer was $MnCl_2$ and the reaction was carried out in air instead of inert atmosphere, in order to allow the oxidation of the metal ion. In the case of the iron dimer, MeONa is added with a 20% excess,[12] while, with regard to the manganese dimer, it has to be strictly stoichiometric. In fact such a reaction, for manganese, is very sensitive to the amount of methoxide and to the order and addition rate of the reagents. A solution of both NaOMe and Na(dpm) in methanol has to be added very slowly (dropwise) to a Mn^{II} solution. If these conditions are not met, two parallel side-reactions can occur. A small excess of methoxide or the addition of the manganese salt solution to the ligands solution favour the formation of insoluble, linear polymeric structures in which methoxide acts as a bridge between manganese ions. On the other hand, if the addition of the ligands is too quick, $[Mn(dpm)_3]$ is formed.

Figure 5.2 presents the FTIR spectra registered for the solid products of various reaction attempts. The most diagnostic absorption band for the dimer is the one at 1048 cm^{-1}, corresponding to a C-O bond stretching in the methoxide ligand, tracked by the black dotted line. In all other products, the shape and position of this band are different and indicate a different chemical environment for the methoxide ligand. The green and the red spectra are assigned to polymeric or oligomeric chain products because of their insolubility in any organic solvent. The blue line, in its turn, is completely superimposable to the one registered for commercial $[Mn(dpm)_3]$ (pink line).

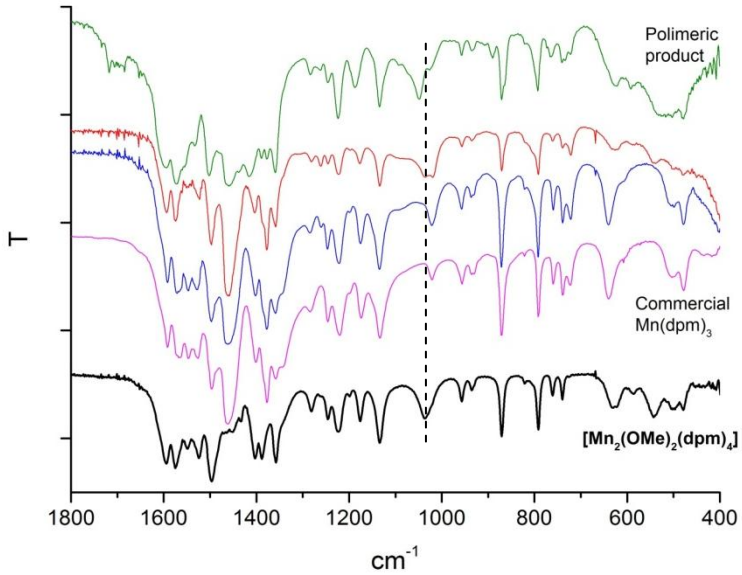

Figure 5.2: FTIR spectra recorded in the region of 1800-400 cm^{-1} for some products of the Mn^{III} dimer preparation. In the first two attempts (green and red lines) a polymeric product was probably formed. In the third spectrum (blue line) the product is the Mn^{III} tris-chelate, compared with the commercial solid (pink line). The last spectrum was registered for the desired product.

In order to confirm the complete oxidation of Mn^{II} to Mn^{III}, an EPR investigation was carried out, exploiting the fact that Mn^{III} is EPR-silent at room temperature[13] in contrast with Mn^{II}-containing complexes, which give intense signals. The absence of EPR spectra for manganese(III) species is due to the fact that its zero field splitting is larger than the EPR microwave quantum, also in high frequency EPR.

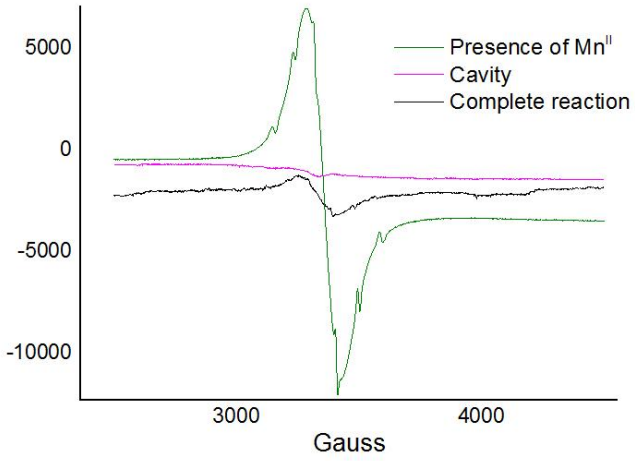

Figure 5.3: Room temperature, W-band EPR spectra registered for two different solid samples obtained during the preparation of the Mn^{III} dimer. Black line: solid isolated after 20h of reaction; green line: after 5h. The pink line comes from the resonant cavity.

Figure 5.3 shows the W-band EPR spectra given by two samples prepared with different reaction times. The black line indicates a practically complete oxidation of the manganese(II) ions during the formation of the dimer. In this case the EPR signal intensity is rather low, particularly considering that the cavity itself has a similar, although weaker, signal (pink line). For a description of the experimental apparatus, see chapter 3. For a shorter reaction, the oxidation seems to be incomplete as a much stronger signal attributable to Mn^{II} is observed (green line). Unfortunately, nothing can be affirmed about the Mn^{III}/Mn^{II} ratio in the solids.

5.2.1 Characterisation

Manganese(III) dimer hexagonal-prismatic crystals, obtained with a well-timed reaction, were obtained by vapour diffusion of methanol into a thf solution. Crystallographic data were collected at RT on a Bruker Kappa X8 APEX II CCD diffractometer with graphite monochromatised Mo-K_α (λ = 0.71073 Å) radiation.

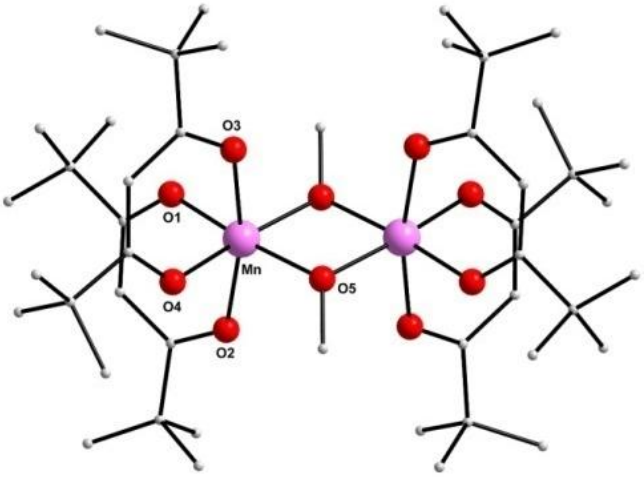

Figure 5.4: Representation of the molecular structure of $[Mn_2(OMe)_2(dpm)_4]$. Pink: manganese; red: oxygen; grey: carbon

$[Mn_2(\mu\text{-}OMe)_2(dpm)_4]$ crystallises in a monoclinic space group, as its iron(III) analogue.[12]

	$[Mn_2(OMe)_2(dpm)_4]$
Empirical formula	$C_{46}\ H_{82}\ Mn_2\ O_{10}$
Formula weight / g mol^{-1}	905.01
Temperature / K	293(2)
Crystal system	Monoclinic
Space group	P21/n
a / Å	15.6260(6)
b / Å	10.9248(5)
c / Å	16.6629(7)
α / °	90
β / °	111.768(2)
γ / °	90
V / $Å^3$	2641.70(19)
F(000)	976
Z	4
ρ_{calcd} / Mg m^{-3}	1.138
μ / mm^{-1}	0.526
θ range / °	2.25 to 27.23
Reflections collected	69135
Independent reflections	5889 [R(int) = 0.0416]
Reflections with $I > 2\sigma_I$	4375
Parameters refined	262
Completeness to θ_{max} /%	99.7
Goodness-of-fit on F^2	1.045
R_1, wR_2 $(I > 2\sigma_I)^a$	$R_1 = 0.0518$, $wR_2 = 0.1430$
R_1, wR_2 (all data)^a	$R_1 = 0.0745$, $wR_2 = 0.1623$
Largest diff peak / hole (e/$Å^3$)	0.591 and -0.266

Table 5.1: Crystal and structure refinement data for $[Mn_2(\mu\text{-}OMe)_2(dpm)_4]$
^{a} As defined by the SHELXL-97 program.[14]

Looking at the bond distances in Table 5.2 it is easy to see that Jahn-Teller distortion occurs along Mn-O directions of two different β-diketonate ligands (Mn-O(2) and Mn-O(3)), with distances equal to 2.092(3) Å and 2.076(2) Å, as compared to *ca.* 1.9 Å of the other Mn-O bonds.

Bond Lengths / Å		$[Mn_2(OMe)_2(dpm)_4]$
M···M	Mn···Mn	3.0397(10)
$M\text{-}O_{methoxide}$	Mn-O(5)	1.934(3)
	Mn-O(5)	1.976(2)
$M\text{–}O_{\beta\text{-diketonate}}$	Mn–O(1)	1.923(3)
	Mn–O(2)	2.092(3)
	Mn-O(3)	2.076(2)
	Mn-O(4)	1.956(3)
Bond Angles / º		$[Mn_2(OMe)_2(dpm)_4]$
$M\text{-}O_{methoxide}\text{-}M$	Mn-O(5)-Mn	102.04(11)
$O_{methoxide}\text{-}M\text{-}O_{methoxide}$	O(5)-Mn-O(5)	77.96(11)
$O_{\beta\text{-diketonate}}\#1\text{-}M\text{-}O_{\beta\text{-diketonate}}\#1$	O(1)-Mn-O(2)	86.78(13)
$O_{\beta\text{-diketonate}}\#2\text{-}M\text{-}O_{\beta\text{-diketonate}}\#2$	O(3)-Mn-O(4)	85.97(11)
$O_{\beta\text{-diketonate}}\#1\text{-}M\text{-}O_{\beta\text{-diketonate}}\#2$	O(1)-Mn-O(3)	85.88(12)
	O(1)-Mn-O(4)	94.31(14)
	O(2)-Mn-O(3)	167.70(11)
	O(2)-Mn-O(4)	84.75(12)
$O_{methoxide}\text{-}M\text{-}O_{\beta\text{-diketonate}}$	O(5)-Mn-O(1)	171.35(12)
		93.56(12)
	O(5)-Mn-O(2)	92.77(11)
		98.49(10)
	O(5)-Mn-O(3)	95.96(11)
		91.81(10)
	O(5)-Mn-O(4)	94.25(13)
		171.65(13)

Table 5.2: Selected bond lengths (Å) and angles (deg) for $[Mn_2(\mu\text{-}OMe)_2(dpm)_4]$.

An additional evidence in favour of the manganese ion in the structure being manganese(III) comes from bond valence sum calculation[15] done on the basis of distances from the structure, by the formulas:

$$s = 10^{[(r-r_0)/B]}$$

$$V_i = \sum_j s_{ij}$$

Equation 5.1

where s is the bond valence for each coordination bond, r_0 and B are empirically determined tabulated parameters[15] and r is the measured distance between the metal ion and the donor atoms of its coordination sphere. The sum of the s values obtained from all M-donor atom distances gives V_i, which should match the assumed oxidation state of the metal ion. The results of this analysis are summarised in Table 5.3.

$[Mn_2(OMe)_2(dpm)_4]$			B = 0.37			
		r (Å)	r_0 Mn^{III} (Å)	s (Mn^{III})	r_0 Mn^{II} (Å)	s (Mn^{II})
Mn	O(1)	1.923(3)	1.760	0.64(1)	1.790	0.70(1)
	O(2)	2.092(3)	1.760	0.407(7)	1.790	0.442(8)
	O(3)	2.076(2)	1.760	0.425(5)	1.790	0.462(6)
	O(4)	1.956(3)	1.760	0.58(1)	1.790	0.64(1)
	O(5)	1.934(3)	1.760	0.62(1)	1.790	0.68(1)
	O(5)	1.976(2)	1.760	0.557(7)	1.790	0.605(7)
				$V_{Mn(III)}$ = 3.24(5)		**$V_{Mn(II)}$ = 3.52(6)**

Table 5.3: Bond valence sum calculations for $[Mn_2(\mu\text{-}OMe)_2(dpm)_4]$.

Considering as acceptable an error limit of ± 0.25,[16] we can assume that the manganese ions in the $[Mn_2(\mu\text{-}OMe)_2(dpm)_4]$ molecule are in the +III oxidation state.

5.2.2 Synthesis

Syntheses were carried out under N_2 with the use of Schlenk techniques. Solvents (Aldrich) were dried by standard procedures[17] and distilled under N_2 prior to use. Anhydrous chromium(III) chloride, anhydrous iron(III) chloride, *n*-butyllithium (1.6 M solution in hexanes) and anhydrous $MnCl_2$ were supplied by Aldrich and used without further purification. 2-Hydroxymethyl-2-ethyl-propane-1,3-diol (H_3L^{Et}, Aldrich) was recrystallised from a hot 1:1 mixture of dry thf and toluene, which gave 87% yield of colourless crystals after standing overnight at –20°C. $[CrCl_3(thf)_3]$,[18] 2-hydroxymethyl-2-phenylpropane-1,3-diol (H_3L^{Ph}) were prepared in high yields by published methods.[19] H_3L^{Ph} was recrystallised from a 3:1 toluene:thf mixture, with nearly quantitative yield.

$[Mn_2(\mu\text{-}OMe)_4(dpm)_4]$

A solution of NaOMe (1.67 M, 14.3 ml, 23.85 mmol) in methanol was added dropwise, for 10min, to a colourless solution of Hdpm (2.93 g, 15.90 mmol) in 20 ml of methanol, previously cooled to 0°C. The obtained solution was let stir for 15 min, then transferred into an isobaric addition funnel, mounted on a two necked round-bottomed flask that contained a solution of $MnCl_2$ (1.00 g, 7.95 mmol) in 50 ml of methanol, also cooled to 0°C. The system was then opened to the air and the addition of the ligands solution was carried out for 2h 30min. When the first drops of the methoxide/β-diketonate solution fell into the very light pink manganese solution, a yellowish-brown product was formed and after 20min it became a heavy brown precipitate. Once the addition of the ligands was completed, the addition funnel was washed twice with 5 ml of methanol. Air was then bubbled into the brown suspension for 5min, which was then let stir overnight. The stirring was stopped to allow the suspension to decant. The deep brown product was then filtered and dried under vacuum (2.59 g). The mother liquor was concentrated under vacuum and left at -20°C for several days, producing additional 470 mg of product. A third batch of powder was isolated after further concentration/cooling steps.

Crystals of $[Mn_2(\mu\text{-}OMe)_2(dpm)_4]$ were obtained as reddish-brown hexagonal prisms after various weeks under N_2 by vapour diffusion of methanol into a thf solution of the brown powder. The product is insoluble in methanol and acetonitrile, very soluble in toluene and ethers and exhibits low solubility in hexane. Total yield: 3.27 g, 0.36 mmol, 92%. Found for $[Mn_2(\mu\text{-}OMe)_2(dpm)_4]$: C, 61.05; H, 9.13. Calc. for $C_{46}H_{82}Mn_2O_{10}$: C, 60.45; H, 9.88.

5.3 Synthesis of a chromium(III)-centred Mn_6Cr aggregate

The structure of the manganese dimer is very similar to the one of its iron analogue, which is used for the preparation of the heterometallic Fe_3Cr or Fe_3V complexes. Therefore the same reaction conditions employed in step III of the modular synthetic procedure (see sections 2.2 or 4.2) could probably be used to synthesise a chromium(III)-centred Mn_3Cr complex. The strategy we used, illustrated in Scheme 5.3, is completed with the reaction of the hexacoordinated chromium core with the manganese(III) dimer in 3:2 molar proportion, as in the case of Fe_3Cr and Fe_3V.

Step I

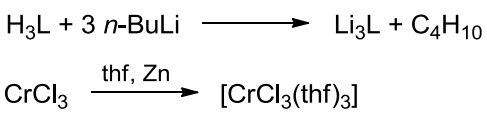

Step II

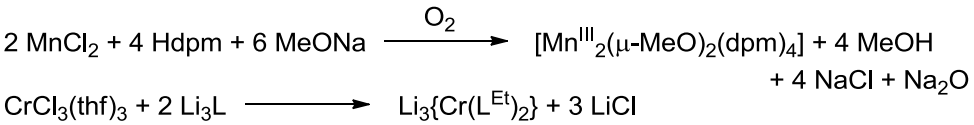

Step III

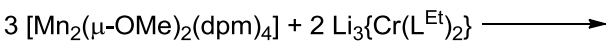

Scheme 5.3: Synthetic strategy for the preparation of a Mn/Cr complex.

As described in chapter 2, the chromium starting material is converted into monomeric $[CrCl_3(thf)_3]$ and then allowed to react with the tripodal alkoxide to produce the chromium core, $[Cr(L)_2]^{3-}$. In this case two tripodal ligands have been used: H_3L^{Et} and H_3L^{Ph}.

With manganese(III), the reaction represented in step III behaved differently from that observed for the iron dimer. After the reflux in glyme was stopped, a dark grey/brown powder precipitated from the reaction solution. FTIR analysis of this first solid indicated the absence of bands relative to dpm ligands (for example at *ca.* 1750 cm^{-1}, due to C=O stretching), while the product presented signals, in the low energy region, due to metal-oxygen bond stretchings.

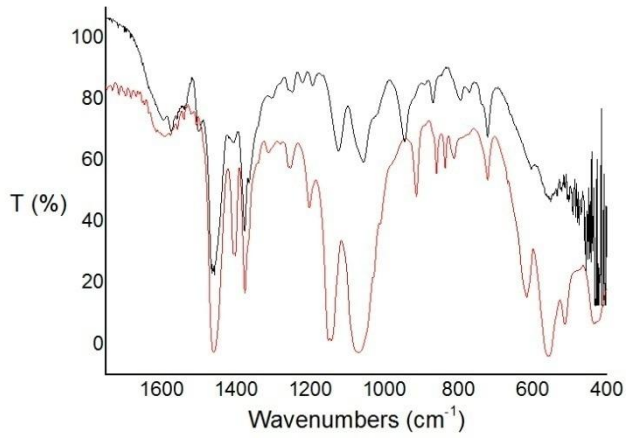

Figure 5.5: FTIR spectrum (Nujol mulls), registered in the 1700-400 cm^{-1} region, for the first solid obtained after step III (Scheme 5.3) using $(L^{Et})^{3-}$ as the tripodal alkoxide (black line) and for the chromium core, $Li_3\{Cr(L^{Et})_2\}$ (purple line).

Figure 5.5 compares the spectra of this first solid to the one recorded for the chromium core, using the same $(L^{Et})^{3-}$ ligand. It is possible to see that the two are very similar. This led to the suggestion that an excess of the chromium core precipitated from the reaction mixture.

The mother liquor of this reaction did not form any other precipitate when placed at -20°C, even after being concentrated several times under vacuum. The only way to isolate the product was to evaporate the solvent to dryness, a procedure that gave a reddish-brown raw solid that was employed for a preliminary characterisation. It resulted soluble in almost all tried organic solvents, *i.e.* hexane, toluene and ethers; it just did not dissolve in methanol and had a very low solubility in acetonitrile. Among all the attempts we run to crystallise this product (see next section 5.3.1), crystals were only obtained from an ether (glyme or thf) solution, using methanol as non-solvent in a closed vapour diffusion crystallisation chamber. It is important to stress that the same approach employing acetonitrile in the place of methanol did not produce crystals but only a powder.

The crystals obtained in this procedure (and also the powder obtained from acetonitrile) were covered by the silicone grease used with the Schlenk glassware, which precipitates after the use of methanol as non-solvent. All attempts to remove this contamination by employing a solvent able to dissolve the grease ended up with the solubilisation of the product. The impossibility to clean these crystals represented a big limitation for further characterisation.

Figure 5.6 shows the comparison of FTIR spectra obtained from the raw solid of the reaction and its crystalline form, obtained from methanol.

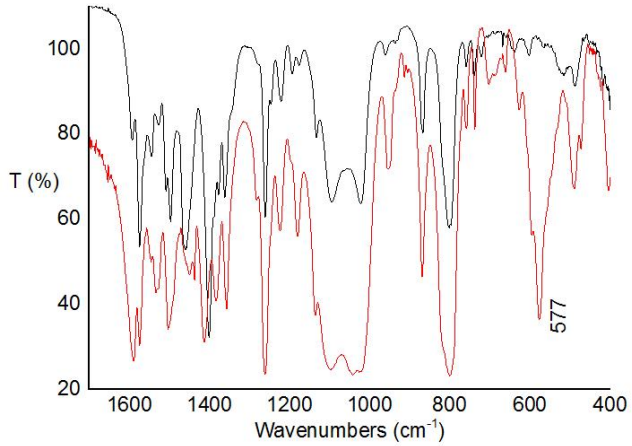

Figure 5.6: FTIR spectra (1700-400 cm^{-1} region) of the raw product (black line) and the reddish-brown crystals (red line). The main difference is the new, intense band at 577 cm^{-1} recorded for the crystals.

The most important change observed when the two spectra in Figure 5.6 are compared is that a new band in the region of metal-oxygen bond stretching (577 cm^{-1}) appears in the sample crystallised from MeOH. This suggests that methanol plays a crucial role in crystal formation, being indeed the only solvent that provides crystals of the product. In fact, MeOH also plays an important role in the chemical composition of the crystallised product, as discussed hereafter.

From a crystallographic point of view, the obtained crystals had a very low diffraction quality, besides losing crystallisation solvent once removed from their mother liquid. Despite all difficulties, a preliminary, partial, molecular structure was obtained by single-crystal X-ray diffraction analysis and it is displayed in Figure 5.7 for both tripodal ligands used: H_3L^{Et} and H_3L^{Ph}.

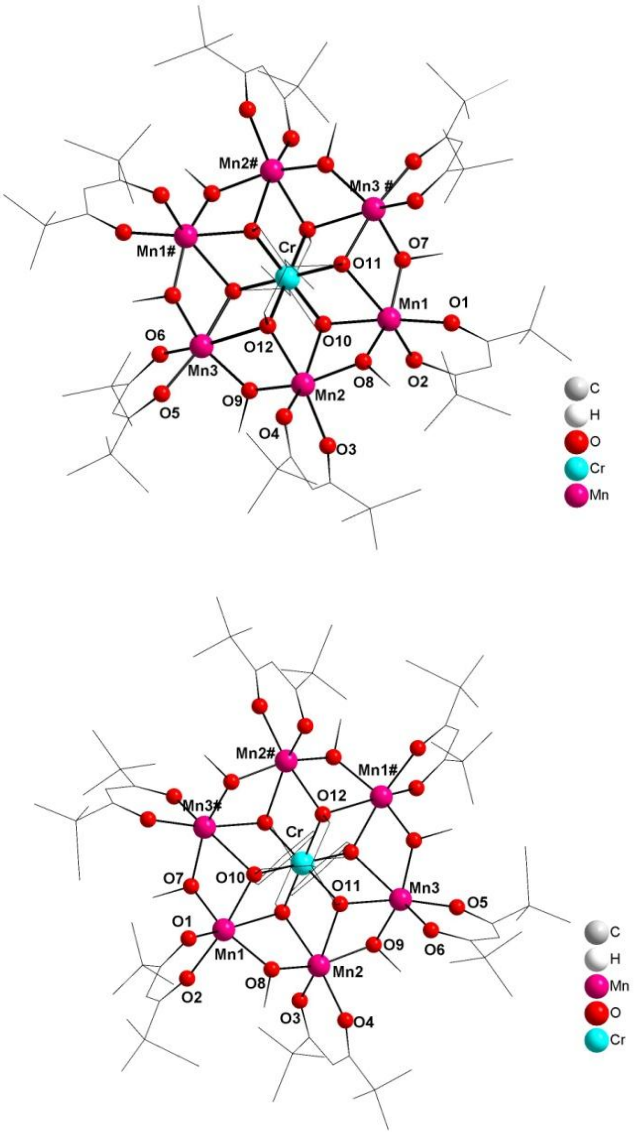

Figure 5.7: Representations of the molecular structures of the heptanuclear complexes $[M_7(L^{Et})_2(\mu\text{-}OMe)_6(dpm)_6]$ (top) and $[M_7Cr(L^{Ph})_2(\mu\text{-}OMe)_6(dpm)_6]$ (bottom).

The resulting structures reveal heptanuclear complexes $[M_7L_2(\mu\text{-}OMe)_6(dpm)_6]$ (tentatively called Mn_6CrL^{Et} and Mn_6CrL^{Ph}) in which the chromium(III) ion is reasonably believed to occupy the central position of the molecule due to its inertness towards substitution reactions. This central ion holds around itself the six oxygen atoms of the two tripodal ligands and is in turn surrounded by six manganese ions. Each peripheral centre, most likely manganese, presents only one dpm ligand in comparison

with the tetranuclear Fe_3M stars, the second dpm being replaced by two bridging methoxide groups. The fact that a negatively charged dpm ligand is removed suggests that the ingoing group is a methoxide and not just a coordinated methanol molecule. Again based on the assumption that the central ions is Cr^{III}, if all peripheral ions are three-positive and all bridging groups are methoxides, the whole coordination entity should possess a +3 charge. In this case counterions such as chlorides should be present in the unit cell. However, no significant residual electron density has been found in the difference map after solving the structure (Table 5.4), therefore preventing the identification of any counterion. This aspect will be analysed in-depth below, in the text. As a consequence, the possibility of mixed-valence for the metal ions has to be considered for these heptanuclear products.

	Mn_6CrL^{Et}	Mn_6CrL^{Ph}
Empirical formula	C_{84} H_{154} Cr Mn_6 O_{24}	C_{92} H_{164} Cr Mn_6 O_{24}
Formula weight / g mol^{-1}	1929.72	2025.80
Temperature / K	293(2)	293(2)
Crystal system	Triclinic	Monoclinic
Space group	*P-1* (No. 2)	*P*21/*n* (No. 14)
a / Å	14.0931(8)	14.2591(6)
b / Å	14.1325(8)	22.9976(9)
c / Å	14.2339(3)	16.7022(7)
α / °	106.989(4)	90
β / °	100.099(4)	97.710(3)
γ / °	93.568(3)	90
V / $Å^3$	2649.6(3)	5427.6(4)
F(000)	1024	2144
Z	2	4
ρ_{calcd} / Mg m^{-3}	1.209	1.240
μ / mm^{-1}	0.851	0.834
θ range / °	1.48 to 27.30	1.69 to 24.90
Reflections collected	78044	56815
Independent reflections	11715 [R(int) = 0.1045]	9252 [R(int)=0.1395]
Reflections with $I > 2\sigma_I$	5194	3556
Parameters refined	350	495
Completeness to θ_{max} /%	98.0	99.0
Goodness-of-fit on F^2	0.995	0.953
R_1, wR_2 ($I > 2\sigma_I$)[a]	R_1=0.0791, wR_2=0.2093	R_1=0.0845, wR_2=0.2083
R_1, wR_2 (all data)[a]	R_1=0.1814, wR_2=0.2660	R_1=0.2129, wR_2=0.2871
Largest diff peak / hole (e/$Å^3$)	1.024 and -0.511	0.662 and -0.331

Table 5.4: Crystal and structure refinement data for $[Mn_6Cr(L^{Et})_2(\mu\text{-}OMe)_6(dpm)_6]$ and $[Mn_6Cr(L^{Ph})_2(\mu\text{-}OMe)_6(dpm)_6]$

[a] As defined by the SHELXL-97 program.[14]

Bond Lengths / Å		**Mn_6CrL^{Et}**	**Mn_6CrL^{Ph}**
$Mn\text{-}O_{methoxide}$	Mn(1)-O(7)	1.97658(10)	1.988(7)
	Mn(1)-O(8)	1.98293(11)	1.976(6)
	Mn(2)-O(8)	1.98525(11)	1.993(8)
	Mn(2)-O(9)	1.98117(12)	1.965(7)
	Mn(3)-O(9)	1.99094(13)	1.992(8)
	Mn(3)-O(7)#1	1.99532(11)	1.972(7)
$Mn–O_{tripodal}$	Mn(1)-O(11)	2.43594(14)	2.434(6)
	Mn(1)-O(10)	2.10659(13)	2.096(5)
	Mn(2)-O(10)	2.42425(12)	2.443(6)
	Mn(2)-O(12)	2.11002(13)	2.105(5)
	Mn(3)-O(11)#1	2.11337(10)	2.111(5)
	Mn(3)-O(12)	2.40958(14)	2.438(5)
$Mn–O_{\beta\text{-diketonate}}$	Mn(1)-O(1)	2.00006(12)	2.073(6)
	Mn(1)-O(2)	2.07982(10)	2.023(10)
	Mn(2)-O(3)	2.01822(12)	1.989(8)
	Mn(2)-O(4)	2.10329(11)	2.077(7)
	Mn(3)-O(5)	2.01603(11)	2.017(9)
	Mn(3)-O(6)	2.08876(11)	2.082(6)
$Cr–O_{tripodal}$	Cr-O(10)	1.95528(12)	1.958(5)
	Cr-O(11)	1.95389(11)	1.957(5)
	Cr-O(12)	1.9587	1.961(5)
Bond Angles / º			
$O_{methoxide}\text{-}Mn\text{-}O_{methoxide}$	O(7)-Mn(1)-O(8)	156.721(2)	157.6(4)
	O(9)-Mn(2)-O(8)	156.846(2)	155.5(4)
	O(9)-Mn(3)-O(7)#1	157.330(2)	156.7(3)
$Mn\text{-}O_{tripodal}\text{-}Cr$	Mn(1)-O(10)-Cr	105.729(5)	105.4(2)
	Mn(1)-O(11)-Cr	94.473(5)	94.0(2)
	Mn(2)-O(10)-Cr	95.014(4)	94.1(2)
	Mn(2)-O(12)-Cr	105.724(4)	105.7(2)
	Mn(3)-O(11)-Cr	105.649(4)	105.3(2)
	Mn(3)-O(12)-Cr	95.284(4)	94.1(2)
$Mn\text{-}O_{tripodal}\text{-}Mn$	Mn(3)-O(12)-Mn(2)	92.571(4)	92.0(2)
	Mn(2)-O(10)-Mn(1)	92.216(5)	92.0(2)
	Mn(1)-O(11)-Mn(3)#1	92.070(4)	91.78(19)
$O_{\beta\text{-diketonate}}\text{-}Mn\text{-}O_{\beta\text{-diketonate}}$	O(1)-Mn(1)-O(2)	85.971(5)	84.8(3)
	O(3)-Mn(2)-O(4)	85.200(3)	86.0(3)
	O(5)-Mn(3)-O(6)	84.905(4)	85.2(3)
$Mn\text{-}O_{methoxide}\text{-}Mn$	Mn(1)-O(7)-Mn(3)#1	111.446(4)	111.1(3)
	Mn(1)-O(8)-Mn(2)	111.116(4)	111.1(4)
	Mn(2)-O(9)-Mn(3)	110.988(4)	112.2(3)

Table 5.5: Selected bond lengths (Å) and angles (deg) for Mn_6CrL^{Et} and Mn_6CrL^{Ph}.

The bond distances concerning the manganese ions, in the two complexes Mn_6CrL^{Et} and Mn_6CrL^{Ph} (Table 5.5), are slightly longer than in the dimer (Table 5.2). Furthermore, only one of the six coordination bonds for each metal undergoes to an elongation. In particular the $Mn\text{-}O_{tripodal}$ bound is *ca.* 2.4 Å (Mn(1)-O(11); Mn(2)-O(10); Mn(3)-O(12)), against an average of 2 Å for the other distances. Just to recall, in the manganese dimer, the Jahn-Teller distortion occurs along Mn-O directions of two different β-diketonate ligands (Mn-O(2) 2.092(3) Å and Mn-O(3) 2.076(2) Å), while the other Mn-O bonds are *ca.* 1.9 Å.

The isolation of the heptanuclear complexes obtained in this work is in agreement with the results of the FTIR analysis of the first solids precipitated from both reaction mixtures, which apparently contained only chromium bound to the tripodal ligand (Figure 5.5). This is because the 2:3 ratio between the chromium core and the manganese dimer, employed in step III of the synthetic route (Scheme 5.3), leaves the chromium core in excess as far as the preparation of Mn_6CrL^R is concerned. Furthermore, the appearance, with respect to the raw product, of the new IR band in the crystalline sample, attributed to methoxide groups bridging two metal ions, suggests that the recrystallisation from methanol plays a crucial role in the formation of the heptanuclear structure.

The molecular metallacrown geometry of Figure 5.7 is not new for manganese.[20,21] It seems that this kind of topology represents a thermodynamic minimum to which the formation of the molecule tends to converge in the presence of methanol. Cornia and co-workers synthesised two similar metallacrown complexes, that is, Mn_6Na[21] (in which the sodium ion is placed in the centre of the structure) and Mn_7[20] clusters. In both cases the starting material was $MnCl_2$, handled in aerobic condition as in the present work. Mn_6Na resulted to be a complete oxidation product, having all manganese ions as Mn^{III}, while Mn_7 is a mixed-valence compound. On the contrary, in our case, the dimeric starting material $[Mn_2(OMe)_2(dpm)_4]$ was demonstrated to be a manganese(III) product. What is the oxidation state of the manganese ions in our structure remains an unanswered question. First of all, the contamination with grease of the crystalline product, although not affecting the crystal structure resolution, did not allow a reliable elemental analysis to be performed on the samples to reveal or eliminate the possibility of the presence of counterions. Furthermore, in this case, an EPR investigation would not have been decisive in identifying the presence of Mn^{II}, because of the spin coupling among the ions, which would not allow, together with the presence of Cr^{III}, a straightforward interpretation of the spectrum. Also, the valence bond sum calculation performed for these compounds, using bond distances coming from the partially solved crystallographic structures, suggested the formation of mixed-valence complexes. They gave a V = 2.53(9) for Mn^{III} and V = 2.77(8) for Mn^{II} for Mn_6CrL^{Et} and V = 2.58(8) for Mn^{III} and V = 2.79(8) for Mn^{II} for Mn_6CrL^{Ph}. There are very close values to +2.5 average oxidation state, obtained modelling the Mn ions as ½ Mn^{III} and ½ Mn^{II}, which would give a neutral complex.

Checkcif routine was run for both compounds, in order to find solvent accessible voids (Platon type 601-606 alerts). The results indicated that Mn_6CrL^{Et} has solvent accessible voids of 67 $Å^3$, while Mn_6CrL^{Ph} has 37 $Å^3$

voids. According to IUCr (International Union of Crystallography), "this test reports the volume of the largest solvent accessible void in the structure. Voids of 40 $Å^3$ may accommodate H_2O. Small molecules such as tetrahydrofuran have typical volumes in the 100 to 200 $Å^3$ range."[22] So, in principle these voids could accommodate chloride (*ca.* 20 $Å^3$). Although there are voids large enough to accommodate counterions in both crystals, there is no residual electron density in the Fourier maps for counter ions (see the largest diff. peaks in Table 5.4). The possible absence of counterions could bring us to think to mixed-valence manganese compounds formation.

As a further attempt to characterise the system, a powder X-ray diffraction pattern (PXRD) was recorded on microcrystalline Mn_6CrL^{Ph} obtained after recrystallisation from MeOH. From the same batch of product, a few crystals were also isolated and then analysed by single crystal X-ray diffraction. The grease that affected such a sample did not interfere with the measurements. Results were compared with two other diffraction patterns: one calculated for the same compound from the single-crystal X-ray structure (as showed in Figure 5.7-bottom) and another obtained for the starting material (Mn^{III} dimer, also calculated from its single-crystal X-ray data). The results are shown in Figure 5.8.

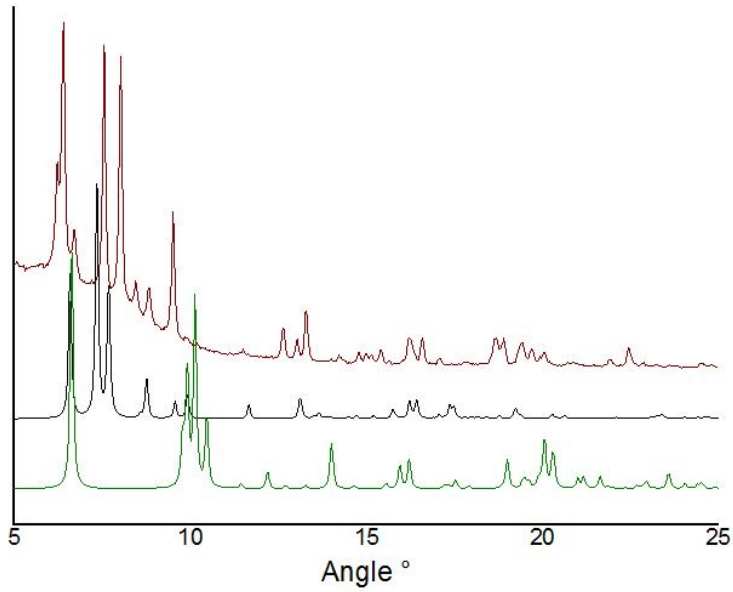

Figure 5.8: PXRD patterns (range 5-25 degrees) of Mn_6CrL^{Ph} (experimental, red); Mn_6CrL^{Ph} (calculated from the structure, black); manganese dimer (calculated, green). At higher angles, no significant peaks are present.

The experimental spectrum apparently indicates the presence of more than one component in the crystal, together with the absence of residual starting material. The first intense peak (at low diffraction angles) of the experimental pattern suggests that a second component presents a comparable cell dimension with respect to the one obtained from the single-crystal structure.

We do not have a clear explanation for these experimental evidences. As the single crystals only form after slow diffusion of methanol into the recrystallisation solution, it is possible that the microcrystalline material whose experimental PXRD pattern is shown in Figure 5.8 contains both the Mn_6CrL^{Ph} product and its precursor, obtained in the absence of methanol. The fact that no other solvent induces crystallisation, together with the impossibility of excluding grease from the reaction apparatus, made the complete investigation of these systems impracticable.

For this reason no magnetic characterisation was performed, also because such characterisation loses importance without the knowledge of the exact chemical structure of the product, which in its turn could allow the establishment of magnetostructural correlations.

5.3.1 Experimental

[$Mn_6Cr(L^{Et})_2(\mu\text{-}OMe)_6(dpm)_6$]

Synthetic steps I and II were the same as described in chapters 2 and 4. In this case, H_3L^{Et} (278 mg, 2.07 mmol), *n*-butyllithium 1.6 M (3.9 ml, 6.21 mmol) and [$CrCl_3(thf)_3$] (360 mg, 0.97 mmol) were used to produce the chromium core, which was subsequently employed in **Step III** Brown [$Mn_2(\mu\text{-}OMe)_2(dpm)_4$] (2.63 g, 2.91 mmol) was suspended in 90 ml of glyme and stirred at RT for *ca*. 15min, before receiving the slow addition of the light greyish-green suspension prepared in the previous step. The system was then heated under reflux for 5h, changing into a solution as soon as boiling started.

After reflux, the reaction mixture showed the presence of a grey powder. The system was cooled down to RT and filtered immediately. The precipitate was discarded (210 mg), while the filtrate was taken completely to dryness. The reddish brown solid, contaminated by white salts and grease from the glassware joints, was highly soluble in numerous different solvents, from hexane and toluene to more polar thf and diethyl ether, while it was not soluble in MeOH and CH_3CN. This solid product was then divided in several parts, in order to try different crystallisation conditions. In every attempt air and moisture were strictly excluded by the use of a glove-box. In some of these attempts, the solid was dissolved in glyme (*ca*. 5 mg/ml), stirred at RT for 30min and then filtered. In one case the clean filtrate (20 ml) was layered with the same amount of methanol. Alternatively, two cristallisation chambers were prepared with vapour diffusion of acetonitrile (50 ml) or methanol (50 ml) into the glyme solution (50 ml). Parallelepiped crystals were only obtained in the last conditions, but they underwent extremely rapid solvent loss when removed from the mother liquid, becoming a brown powder. Since the only working way to produce a crystalline material was to employ methanol as non-solvent, all crystals were contaminated by silicone grease, which has the same solubility and comes out from the reaction mixtures upon addition of methanol. As mentioned earlier, all attempts to dissolve the grease to separate it from the solids ended up with the dissolution of the product, due to its high solubility in the same solvents.

[$Mn_6Cr(L^{Ph})_2(\mu\text{-}OMe)_6(dpm)_6$]

The experimental procedures employed were the same as for Mn_6CrL^{Et}, using 110 mg (0.55 mmol) of H_3L^{Ph}, 1.65 mmol of *n*-butyllithium, 96 mg (0.28 mmol) of [$CrCl_3(thf)_3$] and 750 mg (0.83 mmol) of [$Mn_2(\mu\text{-}OMe)_2(dpm)_4$]. After the third reaction step a grey powder was

filtered off (70 mg) and the filtrate was concentrated and placed at -20°C, but no changes occurred. Also in this case several experimental conditions were tried in order to recrystallise the solid product after evaporating all the solvent from the mother liquor. As in the previous synthesis, only vapour diffusion of MeOH into thf produced the crystals that were used for X-ray powder diffraction.

5.4 Preliminary study on the incorporation of lanthanide(III) ions into the star-shaped molecular frame

As mentioned in section 5.1, an interesting and challenging idea could be the placement of lanthanide (Ln) ions in the external positions of a star-shaped complex. From a synthetic point of view, considering the most common +III oxidation state (which, however is not mandatory for our purposes) for this type of ions,[23] charge balance requirements would be satisfied within a $M^{III}L_2Ln_3$ framework (M = central ion; L = tripodal alkoxide; Ln = tripositive lanthanide centre), similar to the one in Fe_3Cr or Fe_3V. Furthermore, lanthanides can exhibit improved magnetic features because of a large magnetic moment and a large increase in the magnetisation reversal barrier.[24]

Lanthanides are characterised by high spin values and by the fact that their *f* electronic shell favours strong spin-orbit coupling and large unquenched orbital momentum.[25,26] The last two parameters frequently lead to high single ion anisotropy, which can be exploited for SMM purposes.[27]

Our aim was hence to prepare a tetranuclear star-shaped cluster Ln_3Cr, exploiting the modular synthetic strategy used so far. It should not be forgotten that if an Ln_3Cr system exhibited a significant higher blocking temperature than the complexes based on transition metals only, it would be then straightforward to change the tripodal ligand with one functionalised with a linking group for grafting onto a noble metal or oxide surface. This would allow to employ better performing SMMs in prototypes of SMM-based spintronic devices.

Although very appealing, the proposed strategy resulted not to be easily implemented. The first task to be attained was to find a suitable ligand for the lanthanide ions, which are usually characterised by an extended coordination sphere as compared to d-block transition metal ions.

5.4.1 Ligands for lanthanide ions in peripheral positions of star-shaped complexes

Considering a coordination number equal to eight for a lanthanide(III) ion,[28] a suitable ligand for the peripheral positions of a star-shaped cluster should lock six binding positions of the metal ions. This is because the remaining two coordination sites of each Ln^{3+} are supposed to host two oxygen donor atoms coming from the tripodal ligands, as schematised in Figure 5.9. Furthermore, thinking about charge balance in the molecular framework, for a tripositive lanthanide ion two charges have to be 'quenched' by the ligand, in order to confer electroneutrality to the molecule.

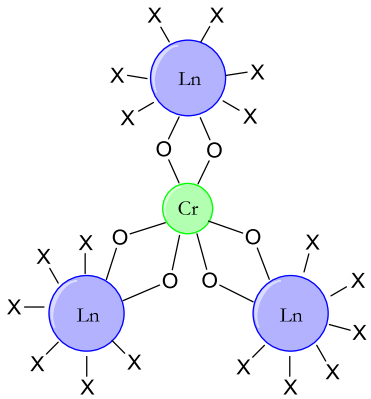

Figure 5.9: Schematic representation of a possible star-shaped Ln_3Cr cluster. X are coordination positions occupied by the lanthanide ligands.

Two proligands were identified as potentially suitable for our objectives; they are represented in Figure 5.10.

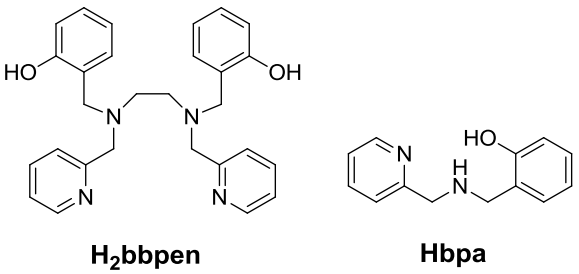

Figure 5.10: H_2bbpen - N,N'-Bis (2-hydroxybenzyl)-*N*,*N*'-bis (2-methylpyridyl) ethylenediamine; Hbpa - (2-hydroxybenzyl)(2-pyridylmethyl)amine.

The first possibility, H_2bbpen,[29–34] is an hexadentate dianionic ligand, known in literature to bind lanthanide ions.[35] The second, Hbpa,[36,37] a tridentate monoanionic ligand, has to be used in 2:1 ratio in combination

with the lanthanide(III) starting materials. Since the latter has only three donor atoms, it may be an interesting alternative in the case H_2bbpen reveals itself too tight in binding the metal, yielding rigid complexes that would not bind the chromium core. In this case a tridentate ligand could provide a more flexible, adjustable coordination sphere.

The syntheses of the two proligands followed literature methods and are summarised in Scheme 5.4 for H_2bbpen[30] and Scheme 5.5 for Hbpa.[36]

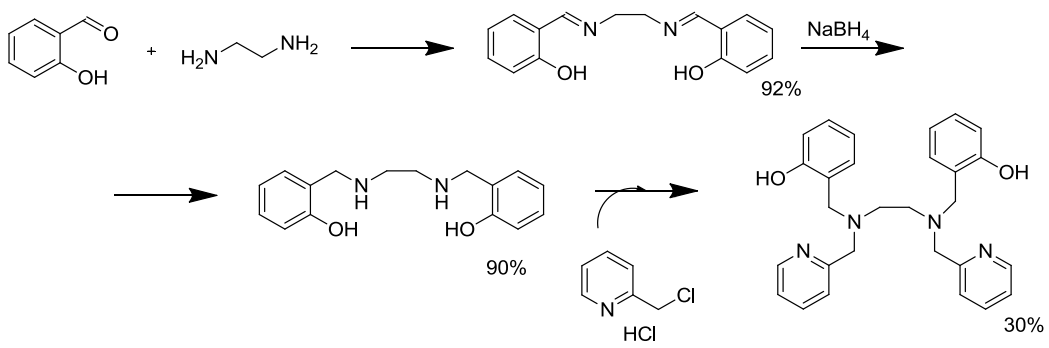

Scheme 5.4: Synthesis of H_2bbpen.

In the case of H_2bbpen, the starting materials were ethylenediamine and salicylaldehyde, which were made to condensate to produce H_2salen.[38] This was subsequently reduced in high yield by sodium borohydride. The last step was a nucleophilic substitution on the picolinic carbon by the phenolic oxygen.

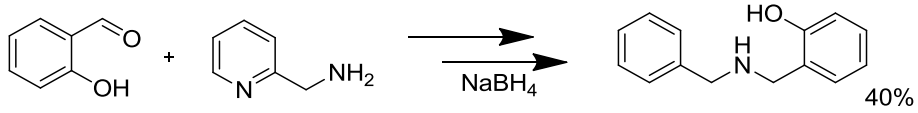

Scheme 5.5: Synthesis of Hbpa. The yield of 40% refers to the recrystallised product.

Hbpa was synthesised, as in the previous case, through condensation between salicylaldehyde and 2-aminomethylpyridine with subsequent reduction operated by sodium borohydride. The purification was carried out by recrystallisation from chloroform.

5.4.2 Synthesis of the ligands

H_2bbpen

A yellow solution of salicylaldehyde (8 ml, 75 mmol) in ethanol (30 ml) received the dropwise addition of ethylenediamine (2.5 ml, 37.4 mmol) under vigorous stirring. The reaction solution first became bright yellow and this was followed by the precipitation of a crystalline solid. At the end of the addition (10min), 5 ml of ethanol were added to facilitate the handling of the heavy suspension. After 30min the yellow solid was filtered, washed with 2 x 10 ml of ethanol and dried under vacuum. The mother liquor was then cooled down to -20°C and, after 24h, a second batch of yellow crystalline precipitated was filtered, washed and dried. Total yield: 9.24 g (92%). Subsequently the whole amount of solid (H_2salen, 34.5 mmol) was suspended in 300 ml of methanol in a 1 l round-bottomed flask and cooled down in an ice bath under N_2 flow. $NaBH_4$ (1.3 g, 34.5 mmol) was added in small portions (in 20min) to this suspension (caution, violent reaction!), which then changed colour to white. The solid was filtered, washed with water and cold methanol, and dried under vacuum. After 1h at 0°C, the mother liquor showed a precipitate, which was also collected by filtration. Total yield 8.46 g (90%). The resulting white solid (23.9 mmol) was added to a solution of 2-(chloromethyl)pyridine · HCl (7.84 g, 47.8 mmol) in 30 ml of water, previously neutralised with 3 M aqueous KOH. The mixture was then heated up till 70°C while its pH was often checked and controlled, to prevent it from rising above 10. A reddish solution was obtained, which was extracted with chloroform (15 ml x 10) after 2 h at room temperature; the organic layer was dried completely and the resulting dark red oil was recrystallised from 25 ml of hot distilled methanol.[17] Yield 3.26 g (30%). ^{1}H-NMR ($CDCl_3$, 400 MHz) δ ppm: 8.5-6.7 (m, 16 H, Ph and Py), 3.8-3.6 (d, 8H, N-CH_2-R), 2.8 (s, 4H, N-CH_2CH_2-N).

Hbpa

30 ml of methanol were cooled down to 0°C and received the dropwise addition of salicylaldehyde, forming a pale yellow solution. 2-aminomethylpyridine (3.99 g, 37 mmol) was added slowly and the solution became bright yellow. The reaction mixture was kept under stirring for 1h in an ice bath, after which $NaBH_4$ (1.4 g, 37 mmol) was added in numerous portions. After 30 min the addition was finished and the colourless solution was left to achieve RT. The solvent was then removed and the resulting pale yellow oil was dissolved in chloroform (30 ml) and washed with a brine solution (2.9 g $NaHCO_3$, 33 g NaCl in 300 ml H_2O). The organic layer was

dried over $MgSO_4$, the solvent was again removed and the obtained oil was recrystallised from hot chloroform. Yield 2.8 g (40%). ^{1}H-NMR ($CDCl_3$, 400 MHz) δ ppm: 8.5 (d, 1H, H_αPy), 7.8-6.3 (m, 7H, Ph and Py), 4.2 (s, 2H, CH_2-Py), 3.8 (s, 2H, CH_2-Ph).

5.4.3 Attempts to prepare a star-shaped Ln_3Cr complex

Most of the syntheses of lanthanide(III) complexes use the anhydrous trichloride[39,40] or the hydrated trinitrate[35,41,42] as suitable starting materials. Although in our case water was best to be avoided in the synthetic procedures, the use of the hydrated terbium nitrate to prepare complexes with $bbpen^{2-}$ or bpa^{-} as ligands was not supposed to compromise the subsequent preparation of the star-shaped complex. This is because the chelation of a hexadentate or of two tridentate ligands to the Ln^{3+} ion is supposed to remove all the coordinating water molecules, as already reported by Yamada *et al.* for a methyl derivative of H_2bbpen.[35]

The first synthetic aim of this part of the work was to build a terbium(III) dimer with $bbpen^{2-}$ and bridging chlorides or methoxides, similar to the Fe^{III} or Mn^{III} dimers, for further reaction with the chromium core. Some attempts were made, employing both $TbCl_3$ and $Tb(NO_3)_3{\cdot}5H_2O$ with the two ligands, $bbpen^{2-}$ or bpa^{-} (Figure 5.10). The major problem encountered in these reactions came from a sudden precipitation of a massive white powder, probably an oligo- or polymeric structure) from the reaction mixtures as soon as methoxide was added into the reaction flask, according to a general Scheme 5.6:

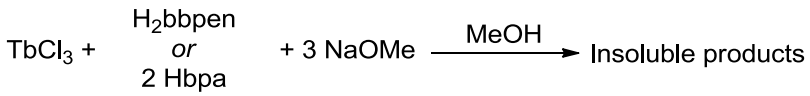

Scheme 5.6

The use of 3 equivalents of methoxide were used in order to create a MeO^{-} bridge in a dimeric structure.

Unfortunately we did not have better results using $Tb(NO_3)_3$, starting material, as shown in Scheme 5.7:

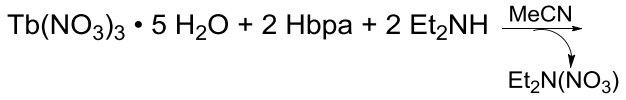

Scheme 5.7

In this case we avoided the use of methoxide and the deprotonation of the proligand Hbpa was carried out with diethanolamine. It's clear that, in this case, methanol could not be compatible with such a base, because of the Et_2NH_2OMe formation, thus acetonitrile was employed as reaction solvent. The problem, for this reaction, was the opposite of the previous ones, because the reaction product was so soluble that no precipitation occurred

after various concentration/cooling steps. Unluckily, for problems due to time limitation, this aspect was not investigated as it would have deserved.

Only once we managed to isolate a monomeric product, employing methoxide in a slightly defect, as shown in Scheme 5.8:

$$TbCl_3 + H_2bbpen + 2.8\ NaOMe \xrightarrow{MeOH} [Tb(bbpen)Cl] + 2\ NaCl$$

Scheme 5.8

It clearly emerges that the methoxide plays a relevant role in the formation of an insoluble product, when added in excess to the quantity necessary to deprotonate the proligand.

The reaction displayed in Scheme 5.8 was carried out under N_2 atmosphere, at RT, adding dropwise a solution of $bbpen^-$ to the terbium chloride solution. At the end of the reaction (overnight) no solids appeared. When the solution was completely dried, a first pale yellow solid was obtained. This solid revealed to be insoluble in thf, hexane, and isopropanol. Prismatic crystal were obtained after a vapour diffusion of thf in a methanol solution of the product. Their crystallographic structure, shown in Figure 5.11, revealed the formation of a monomeric heptacoordinated complex in which the terbium is bound to the six donor atoms of $bbpen^-$ ligand and to one chloride.

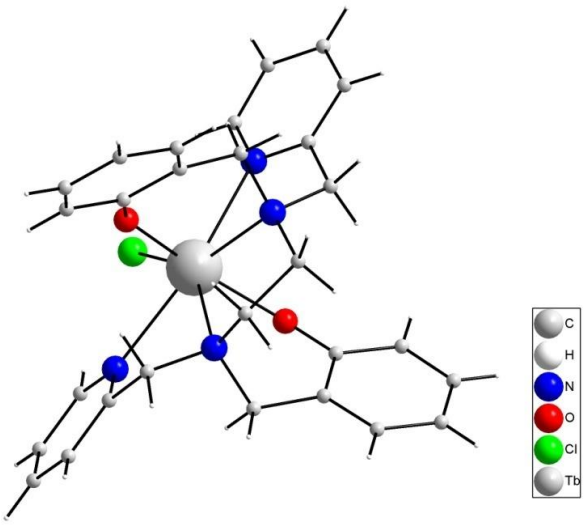

Figure 5.11: Representations of the molecular structures of the complexes [Tb(bbpen)Cl].

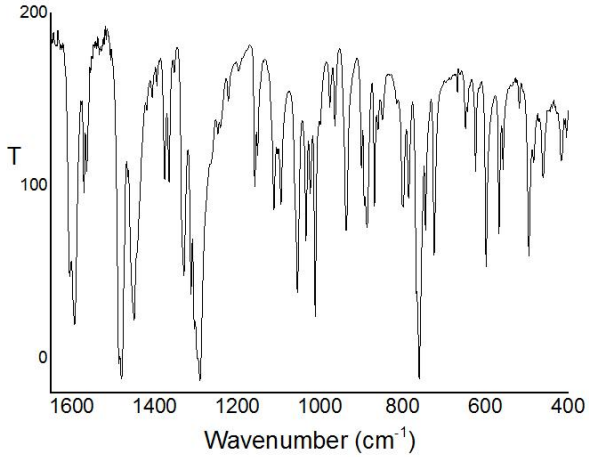

Figure 5.12 FTIR spectra (1650-400 cm^{-1} region) of the crystalline [Tb(bbpen)Cl].

	[Tb(bbpen)Cl]
Empirical formula	C_{28} H_{28} Cl N_4 O_2 Tb
Formula weight / g mol^{-1}	645.91
Temperature / K	293(2)
Crystal system	Orthorombic
Space group	C2221
a / Å	8.7305(3)
b / Å	17.2019(7)
c / Å	17.0427(5)
α / °	90
β / °	90
γ / °	90
V / $Å^3$	2559.49(16)
F(000)	1288
Z	4
ρ_{calcd} / Mg m^{-3}	1.679
μ / mm^{-1}	2.901
θ range / °	2.37 to 27.23
Reflections collected	18044
Independent reflections	2852 [R(int) = 0.0180]
Reflections with $I > 2\sigma_I$	2790
Parameters refined	162
Completeness to θ_{max} /%	99.1
Goodness-of-fit on F^2	1.078
R_1, wR_2 ($I > 2\sigma_I$)[a]	R_1 = 0.0115, wR_2 = 0.0289
R_1, wR_2 (all data)[a]	R_1 = 0.0121, wR_2 = 0.291
Largest diff peak / hole (e/$Å^3$)	0.355 and -0.218

Table 5.6: Crystal and structure refinement data for [Tb(bbpen)(Cl)].

[a] As defined by the SHELXL-97 program.[14]

Bond Lengths / Å		[Tb(bbpen)Cl]
Tb-Cl	Tb-Cl	2.6774(11)
Tb-O	Tb-O	2.174(3)
$Tb-N_{py}$	Tb-N(1)	2.571(3)
$Tb-N_{alk}$	Tb-N(2)	2.594(3)
Bond Angles / °		[Tb(bbpen)Cl]
O-Tb-O	O-Tb-O#1	153.58(14)
N_{py}-Tb-N_{py}	N(1)-Tb-N(1)#1	160.91(15)
N_{alk}-Tb-N_{alk}	N(2)#1-Tb-N(2)	69.51(13)
O-Tb-N_{py}	O-Tb-N(1)	86.72(11)
	O-Tb-N(1)#1	97.64(11)
O-Tb-N_{alk}	O-Tb-N(2)#1	75.84(9)
	O-Tb-N(2)	82.47(10)
N_{py}-Tb-N_{alk}	N(1)-Tb-N(2)#1	133.39(10)
	N(1)-Tb-N(2)	65.51(10)
Cl-Tb-O	Cl-Tb-O	103.21(7)
Cl-Tb-N_{py}	Cl-Tb-N(1)	80.46(8)
Cl-Tb-N_{alk}	Cl-Tb-N(2)	145.25(7)

Table 5.7: Selected bond lengths (Å) and angles (deg) for [Tb(bbpen)(Cl)].

[Tb(bbpen)Cl] was employed in the reaction with the chromium core (step III of the synthetic procedure for Fe_3M compounds, M: Cr^{III}, V^{III}), in order to prepare the desired chromium-centred complex, as shown in Scheme 5.9, but only the starting materials were recovered at the end of the process.

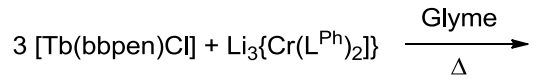

Scheme 5.9

Probably the lack of reactivity between the terbium complex and the chromium core is due to the fact that the $bbpen^-$ ligand has a big steric hindrance, as suggested by the coordination number for [Tb(bbpen)Cl] limited to seven. This may not allow the replacement of the chlorine ion by the oxygen atoms of the triol ligand.

An interesting attempt would have been the employment of the smaller and more flexible tridentate Hbpa proligand, but because of the time limitation of my stay at the *Laboratório de Bioinorgânica* of *Universidade Federal do Paraná*, the topic was not further investigated, although it would have deserved additional efforts due to the appealing magnetic properties that lanthanide-containing, mixed metal star-shaped complex could present.

Synthesis of [Tb(bbpen)Cl]

A solution of NaOMe (0.435 M, 7.8 ml, 3.39 mmol) in methanol was added dropwise to a suspension of H_2bbpen (548 mg, 1.21 mmol) in 25 ml of methanol, previously cooled to 0°C, obtaining a very pale yellow solution. This was let stir for 20min, then added very slowly to a solution of anhydrous $TbCl_3$ (320 mg, 1.21 mmol) in 10 ml of methanol. Once the addition of the ligands was completed, the obtained solution was then let stir overnight. After 16h reaction no evidences of changing were observable. The solution was dried under vacuum, obtaining a pale yellow solid, mixed with salt. Solubilisation tests revealed that the solid is insoluble in apolar (hexanes), medium polar (thf, acetonitrile, isopropanol) solvents, but is soluble only in the strongly polar methanol. Various attempts of recystallisation were carried out (with 5mg/ml solid:solvent ratio), ranging from slow evaporation of the solvent to vapour diffusion of thf in the product methanol solution, in inert atmosphere or in air. In one case (vapour diffusion under inert conditions) colourless prismatic crystals of [Tb(bbpen)Cl] were obtained. Theoric yield: 782 mg, 1.21 mmol, Found for [Tb(bbpen)Cl]: C, 50.94; H, 4.83; N 8.24. Calc. for $C_{28}H_{28}ClN_4O_2Tb$: C, 51.98; H, 4.36; N, 8.66.

(1) Gatteschi, D.; Sessoli, R. *Angew. Chemie Int. Ed.* **2003**, *42*, 268–297.

(2) Glaser, T. *Chem. Commun.* **2011**, *47*, 116–130.

(3) Cirera, J.; Ruiz, E.; Alvarez, S.; Neese, F.; Kortus, J. *Chem. Eur. J.* **2009**, *15*, 4078–4087.

(4) Cornia, A.; Fabretti, A. C.; Garrisi, P.; Mortalò, C.; Bonacchi, D.; Gatteschi, D.; Sessoli, R.; Sorace, L.; Wernsdorfer, W.; Barra, A.-L. *Angew. Chemie Int. Ed.* **2004**, *43*, 1136–1139.

(5) Accorsi, S.; Barra, A. L.; Caneschi, A.; Chastanet, G.; Cornia, A.; Fabretti, A. C.; Gatteschi, D.; Mortalo, C.; Olivieri, E.; Parenti, F.; Rosa, P.; Sessoli, R.; Sorace, L.; Wernsdorfer, W.; Zobbi, L. *J. Am. Chem. Soc.* **2006**, *128*, 4742–4755.

(6) Tancini, E.; Rodriguez-Douton, M. J.; Sorace, L.; Barra, A.-L.; Sessoli, R.; Cornia, A. *Chem. Eur. J.* **2010**, *16*, 10482–10493.

(7) Totaro, P.; Westrup, K. C. M.; Boulon, M.-E.; Nunes, G. G.; Back, D. F.; Barison, A.; Ciattini, S.; Mannini, M.; Sorace, L.; Soares, J. F.; Cornia, A.; Sessoli, R. *Dalt. Trans.* **2013**, *42*, 4416–4426.

(8) Sharpe, P.; Richardson, D. E. *J. Am. Chem. Soc.* **1991**, *113*, 8339–8346.

(9) Yan, R.; Huang, W.; Wang, Q.; Jiang, Y. *Ionics (Kiel).* **2009**, *15*, 627–633.

(10) Da Silva, M. A. V. R.; Ferrão, M. L. C. C. H. *Can. J. Chem.* **1988**, *66*, 651–654.

(11) Gohdes, J. W.; Armstrong, W. H. *Inorg. Chem.* **1992**, *31*, 368–373.

(12) Florence Le Gall, Fabrizia Fabrizi de Biani, Andrea Caneschi, Patrizia Cinelli, Andrea Cornia, Antonio C. Fabretti, D. G. *Inorganica Chim. Acta* **1997**, *262*, 123–132.

(13) Goldberg, D. P.; Telser, J.; Krzystek, J.; Montalban, A. G.; Brunel, L.-C.; Barrett, A. G. M.; Hoffman, B. M. *J. Am. Chem. Soc.* **1997**, *119*, 8722–8723.

(14) Sheldrick, G. M. SHELXS-97: Program for Crystal Structure Solution, University of Göttingen, Germany **1997**.

(15) Brown, I. D.; Altermatt, D. *Acta Cryst* **1985**, *244*, 244–247.

(16) Thorp, H. H. *Inorg. Chem.* **1992**, *31*, 1585–1588.

(17) Armarego, W. L. .; Perrin, D. . *Purification of Laboratory Chemicals*; 4th ed.; Butterworth-Heinemann, **1997**; p. 544.

(18) Herwig, W.; Zeiss, H. *J. Org. Chem.* **1958**, *23*, 1404.

(19) Viguier, R.; Serratrice, G. *Eur. J. Inorg. Chem.* **2001**, 1789–1795.

(20) Abbati, G. L.; Cornia, A.; Fabretti, A. C.; Caneschi, A.; Gatteschi, D. *Inorg. Chem.* **1998**, *37*, 3759–3766.

(21) Abbati, G. L.; Cornia, A.; Fabretti, A. C.; Caneschi, A.; Gatteschi, D. *Inorg. Chem.* **1998**, *37*, 1430–1431.

(22) IUCr PLAT601 http://journals.iucr.org/services/cif/checking/PLAT601.html.

(23) Rinehart, J. D.; Long, J. R. *Chem. Sci.* **2011**, *2*, 2078–2085.

(24) Chilton, N. F.; Langley, S. K.; Moubaraki, B.; Murray, K. S. *Chem. Commun.* **2010**, *46*, 7787–7789.

(25) Lin, P.-H.; Burchell, T. J.; Ungur, L.; Chibotaru, L. F.; Wernsdorfer, W.; Murugesu, M. *Angew. Chem. Int. Ed. Engl.* **2009**, *48*, 9489–9492.

(26) Sessoli, R.; Powell, A. *Coord. Chem. Rev.* **2009**, *253*, 2328–2341.

(27) Rinehart, J. D.; Fang, M.; Evans, W. J.; Long, J. R. *Nat. Chem.* **2011**, *3*, 538–542.

(28) Dehnicke, K.; Greiner, A. *Angew. Chem. Int. Ed.* **2003**, *42*, 1340–1354.

(29) Neves, A.; Brito, M. A. D. E.; Souzat, D. H. F.; Fisica, I. De; Carlos, D. S.; Paulo, U. D. S. *Polyhedron* **1995**, *14*, 1307–1314.

(30) Neves, A.; Erthal, S.; Vencato, I. *Inorg. Chem.* **1992**, *31*, 4749–4755.

(31) Adams, H.; Bradshaw, D.; Fenton, D. E. *Eur. J. Inorg. Chem.* **2001**, 859–864.

(32) Xu, L.; Setyawati, I. A.; Pierreroy, J.; Pink, M.; Jr, V. G. Y.; Patrick, B. O.; Rettig, S. J.; Orvig, C.; Mall, M.; Vt, B. C.; August, R. V; H, N. O.; Clbbpen, H. *Inorg. Chem.* **2000**, *39*, 5958–5963.

(33) Martínez-Sánchez, J.; Bastida, R.; Macías, A.; Adams, H.; Fenton, D. E.; Pérez-Lourido, P.; Valencia, L. *Polyhedron* **2010**, *29*, 2651–2656.

(34) Lee, B.-L.; Kärkäs, M. D.; Johnston, E. V.; Inge, A. K.; Tran, L.-H.; Xu, Y.; Hansson, Ö.; Zou, X.; Åkermark, B. *Eur. J. Inorg. Chem.* **2010**, 5462–5470.

(35) Yamada, Y.; Takenouchi, S.; Miyoshi, Y.; Okamoto, K. *J. Coord. Chem.* **2010**, *63*, 996–1012.

(36) Neves, A.; de Brito, M. a.; Vencato, I.; Drago, V.; Griesar, K.; Haase, W. *Inorg. Chem.* **1996**, *35*, 2360–2368.

(37) Viswanathan, R.; Palaniandavar, M.; Balasubramanian, T.; Muthiah, P. T. *Dalt. Trans.* **1996**, 2519–2525.

(38) Diehl, H.; Hach, C. C. *Inorg. Synth.* **1950**, *3*, 196–201.

(39) Petoud, S.; Muller, G.; Moore, E. G.; Xu, J.; Sokolnicki, J.; Riehl, J. P.; Le, U. N.; Cohen, S. M.; Raymond, K. N. *J. Am. Chem. Soc.* **2007**, *129*, 77–83.

(40) Samuel, A. P. S.; Lunkley, J. L.; Muller, G.; Raymond, K. N. *Eur. J. Inorg. Chem.* **2010**, *2010*, 3343–3347.

(41) Figuerola, A.; Diaz, C.; Ribas, J.; Tangoulis, V.; Granell, J.; Lloret, F.; Mahia, J.; Maestro, M. *Inorg. Chem.* **2003**, *42*, 641–649.

(42) Jones, P. L.; Amoroso, A. J.; Jeffery, J. C.; McCleverty, J. A.; Psillakis, E.; Rees, L. H.; Ward, M. D. *Inorg. Chem.* **1997**, *36*, 10–18.

Chapter 6

Tetrairon star-shaped complex organised on gold surface

6.1 Introduction

As already mentioned in the first chapter, in the last few years the field of organisation of SMMs on surfaces has been one of the most active of molecular magnetism. In fact, if the rich magnetic properties of this class of materials have to be exploited in devices,[1] the molecules need to be deposited on conducting substrates or inside nanogaps between electrodes.[2–4] We discussed the different ways to organise molecules, in particular SMMs, on surface. We saw that a wet-chemistry method, like the self assembling of monolayers (SAM) technique,[3–6] allows a good control of the parameters involved in the grafting operations by playing, through a rational synthesis, on the chemical design of the molecule. We have seen, in the following chapters, that the propeller-like architecture of Fe_4 SMM is very versatile as both spin and magnetic anisotropy can be tuned chemically by substitution of the central metal atom. An additional interesting feature of this SMMs family is the possibility to easily modify the residue on the tripodal ligand, without altering the magnetic properties. This has allowed the introduction of functional groups able to graft these SMMs to substrates like noble metals.

In this chapter we focus on the anchoring of Fe_4 molecules on gold surface, through a S-Au bond.[3,7] Previous studies of our group have shown that these SMMs retain their bulk magnetic properties when grafted on gold as a monolayer deposit.[8,9] The introduction of a linker group, promoting the grafting, can be done through a ligand substitution reaction on the standard $[Fe_4(\mu\text{-}OMe)_6(dpm)_6]$ with two tripodal ligands, each bringing the anchoring group.[7] In Figure 6.1 is schematically illustrated a grafting way to bind an opportunely modified Fe_4 complex on gold.

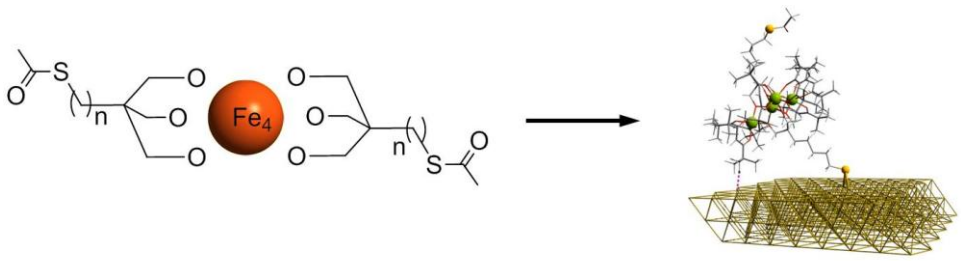

Figure 6.1: Schematic representation of a Fe_4 complex grafted on a gold surface. The R moieties contain a suitable anchor group.

6.2 SAM of tetrairon star-shaped complex on gold

Self Assembly of monolayer (SAM) on noble metal mainly exploits the great affinity of sulphur toward such metals. It is thus possible to deposit sulphur-functionalised molecules by immersing the gold substrate in their diluted solution, as described in chapter one.

Linear-chain alkanethiols, $-(CH_2)_nSH$, are extremely efficient linking units for SAM preparation on gold: the SH groups react with Au(111) surface and strong Au–S bonds are formed, while alkyl chains promote the 2D organisation of molecules into an ordered molecular array by intermolecular interactions.[5] Unfortunately Fe_4 core is not compatible with free S-H termination groups that can compete with and replace ligands present in the star-shaped structure, inducing significant structural modifications; thiols can also induce a reduction of the molecular system being thiols not compatible with higher oxidation states of metal ions.[10]

Variants over the described strategy involve the direct adsorption of acetyl-protected thiols promoted by the addition to the solution of specific deprotecting agents.[11–15] Also thioacetyl groups, without any deprotecting agent, have been directly used[11,16,17] to induce the formation of Au-S interaction with the spontaneous cleavage of the $S–(C=O)CH_3$ bond, as demonstrated also by theoretical evaluations.[18] This alternative clean strategy guarantees the best condition for the stability of Fe_4. On the other hand, the absence of cleavage-promoting agents reduces the quality of the SAM, affecting the rate of the monolayer formation.[19,20] This, anyway, does not compromise the success of the array formation.[16] Moreover, as the grafting procedure is performed without addition of deprotecting agents, covalent grafting, through spontaneous cleavage of the S-C (acetyl) bond, can compete with physisorption of intact thioacetylated derivatives.[19,21,22]

A Fe_4 derivative, specifically designed for grafting to gold surfaces, can be functionalised by two tripodal ligands with SAc-terminated alkyl chains, introduced by replacing the six methoxide groups.[23] These linkers have been already adopted in the realisation of graftable Fe_4 system.[8,9,23] In this case, acetyl-protected sulphur has been used without any deprotection by an exogenous base, in contrast to what commonly is done to generate SAMs.[16,21,22]

In order to shed light on the mechanism involved in the formation of SAM of SAc functionalised Fe_4, a multitechnique investigation was carried out by this group, at an earlier stage of this study, employing a particular derivative, with formula $[Fe_4(L)_2(dpm)_6]$[24] where H_3L is the sulphur-functionalised tripodal ligand 11-(acetylthio)-2,2-

bis(hydroxymethyl)undecan-1-ol.[23] This complex will be named here Fe_4C_9SAc and is showed, together with a scheme of the ligand, in Figure 6.2. The long alkyl chain was chosen as an insulating spacer, in order to minimise the interaction of free electrons of gold with the magnetic Fe_4 core.

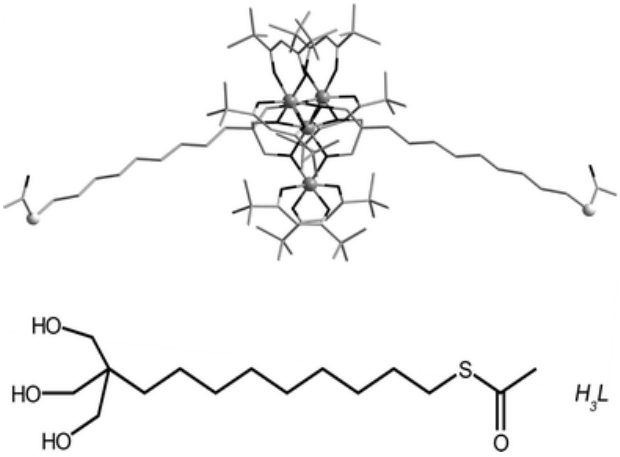

Figure 6.2: Top: molecular structure of the Fe_4C_9SAc complex with iron atoms drawn as large grey spheres, sulphur atoms as pale grey spheres, carbon as light grey sticks and oxygen as black sticks. Bottom: scheme of the sulphur-functionalised tripodal ligand H_3L.

Previous studies confirmed the intactness of tetrairon(III) on a conductive surface and clarified the morphology, composition and structure of Fe_4C_9SAc grafted of gold. The multitechnique approach, carried out by Scanning Tunnelling Microscopy (STM) to get information about the morphology of the assembled film and X-ray Photoelectron Spectroscopy (XPS), which provided semi-quantitative chemical composition of the Fe_4C_9SAc-based monolayer. Also surface sensitive mass spectrometry (*i.e.* Time of Fly Secondary Ion Mass Spectrometry, ToF-SIMS) was employed as powerful technique to provide chemical information about adsorbates present at the surface, but two questions concerning the grafting of thee molecules as schematised in Figure 6.3 have not been totally clarified.

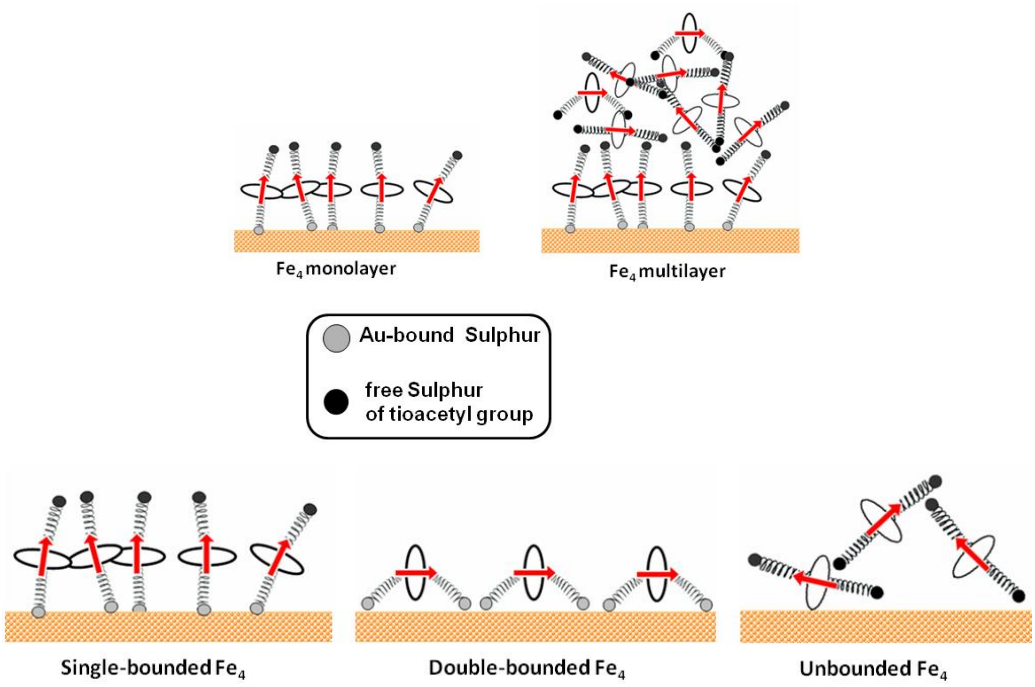

Figure 6.3: Top – schematic representation of the of grafting mode possibilities for the Fe_4C_9SAc SMM, organised as monolayer or multilayer.
Bottom - schematic view of the standing-up and lying-down grafting modes, with the relative orientation of the easy axis of magnetisation indicated by the red arrow. The sulphur atom not bound to gold of the standing-up configuration is depicted as a dark sphere.

The first (top of Figure 6.3) addresses the nature of the deposit of such a molecule on the gold substrate. A further confirmation has to be sought on the effective monolayer formation, consequent to a SAM methodology. For our purposes, a monolayer deposit is surely more appropriate than a multilayer, because a chemical grafting of a single layer can induces the SMMs organisation, which can be exploited to address individually single molecules.

The second (bottom in Figure 6.3) deals with the possibility for the molecule to binds the surface by a single or double grafting group. The actual mode of binding was not clear, previous XPS investigations are not, conclusive. Such a technique is based on the irradiation of, in our case, SMMs functionalised surface with x-rays. This causes a ionisation of the atoms deposited on the surface and the emission of electrons. The kinetic energy of these photoelectron depends on which inner orbital of which atom it comes from and on its chemical environment thus allowing an identification of the oxidation state. Moreover, the number of electrons

reaching the detector can be used for a semi-quantitative analysis. The XPS provides information about the presence of a given element and on its valence state and chemical environment, allowing the identification of the different chemical species present on surfaces. It investigates the first 10 nm layers of sample, therefore it is a suitable technique to investigate the composition of the sample surface. Electrons coming from internal, bulk, sample are in fact quenched before they reach the surface to leave the sample.

Unfortunately, in the case of Fe_4 SAMs XPS, as specified above, it does not supply definitive results, because it cannot distinguish, for instance, between a situation in which all the molecules are mono-grafted at the surface (left picture at the bottom in Figure 6.3) from a case in which half of the molecules are double-grafted and the other ones are just physically adsorbed (second and third pictures). Moreover another problem affects the XPS technique applied to these systems. Despite the high surface sensitivity of XPS, we experience a problem of sensitivity if we are interest, for instance, on the nature of the sulphur atoms, in order to distinguish between physisorbed or chemisorbed species. This occurs because Fe_4 molecules discoid diameter is about 16 Å, so, due to the large area occupied by the molecules on the surface, the ratio sulphur/gold is very low, as well as the signal ratio of the relative peaks. Because of this, the sensibility of the method dramatically decreases and it is difficult to have definitive responses.

During this PhD thesis we tried to shed lights on these aspects, related to the grafting mechanism of SMMs on surfaces, by using the knowledge acquired in previous studies[3,24] and employing a combined approach based on the selective deuteration of the thioacetyl protecting group and investigation of the formed SAM through surface specific mass spectrometry Time-of-Flight Secondary Ion Mass Spectrometry.

6.3 ToF SIMS investigation on a deuterated Fe_4 SMM

Time-of-Flight Secondary Ion Mass Spectrometry,[25] with its soft ionisation mechanism, is particularly suited for the desorption[22,24,26–29] of fragile molecules, such as the metal ion polynuclear systems under study here. Moreover, the technique is completely surface sensitive,[30] since only the first molecular layers of the sample are involved in the ionic bombardment and subsequent desorption.

The investigated sample is bombarded with pulsed primary ions beam (Ga^+, Cs^+, Au^+ or C_{60}^+) with energy in the range of 10-25 keV, producing fragmentation and bond breaking in the close proximity of the collision site. The obtained atomic particles, moving into the sample, partially lose energy and, thus, progressive collisions become less energetic producing a less efficient fragmentation and, then, the emission of molecular fragments that if originated on surface remains charged.

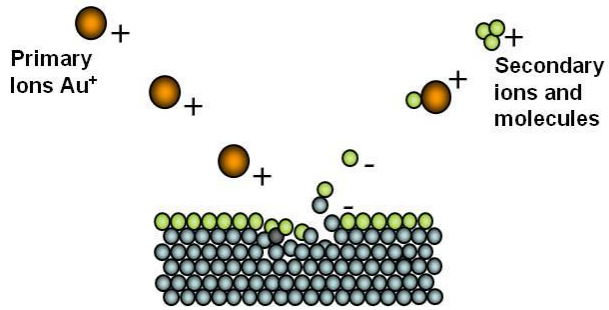

Figure 6.4: Scheme of the secondary particle emission mechanism.

Figure 6.4 illustrates the mechanism in which the secondary particle, neutral, positive or negative molecule and atoms are produced. Only the charged ones, are collected by the time of flight detector, revealed and analysed as a function of their *m/z* ratio. Due to the possibility of placing the detector far from the sample, which means that secondary ions have a long path to get to it (Figure 6.5), this technique provides an excellent mass resolution (often exceeding 10,000 $m/\Delta m$).[31]

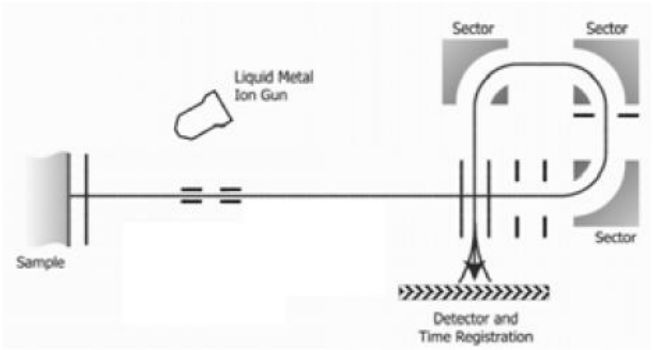

Figure 6.5: ToF-SIMS spectrometer simplified scheme.

Particles produced with this process come from the top 2–3 layers of the sample; only these molecules have sufficient energy to overcome the surface binding energy and can leave the sample. For this reason SIMS detects really only the composition of the surface.

In the light of what discussed above ToF-SIMS spectroscopy is able to give important exhaustive and conclusive answers to the problem described in previous section 6.2, that is, to clarify:

- how the grafting occurs: if there is a covalent bond S-Au, with cleavage of the acetyl moiety, or is just a physisorbtion on gold.
- if only a monolayer is forming or a thick layer, composed by bound (first layer) and unbound molecules.
- if the molecules are mono or double-grafted on the surface, employing one or both anchoring groups.

In order to achieve less ambiguous results we decided to introduce an isotopic label into the studied Fe_4 SMM to be deposited on gold surface.

6.4 Isotopic labelling in Fe_4 deposited on gold

Isotopic labelling is relatively common in mass spectrometry to get insights in the fragmentation process,[6,32–35] here associated to surface sensitive ToF-SIMS for the investigation of the structure of a monolayer by directly labelling the linker group involved in the chemisorption. The isotopic mark was introduced in the Fe_4C_9SAc molecule, described above, conveniently modified, in order to substitute the three hydrogen atoms of the thioacetyl CH_3 group with three deuterium ones.

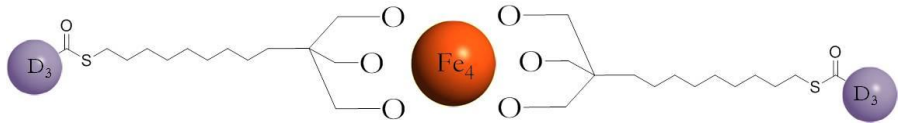

Figure 6.6: Scheme of the Fe_4C_9SAc-d_6. The deuterated positions are highlighted.

The synthesis to get to the modified Fe_4C_9SAc-d_6 was obtained through the ligand exchange reaction, typical for the introduction of the tripodal ligands in star-shaped systems.[23,36–38] The insertion of the deuterium label was performed on the ligand, following the reaction route sketched in Scheme 6.1 together with the ligand exchange reaction:

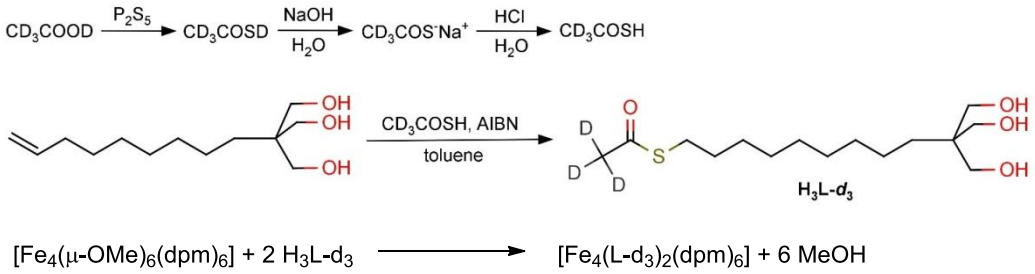

Scheme 6.1: Synthetic strategy for the tripodal ligand H_3L-d_3 and subsequent Fe_4C_9SAc-d_3.

Selective deuteration of the protecting group (-$SCOCD_3$) of 1-(acetylthio)-2,2-bis(hydroxymethyl)undecan-1-ol (H_3L) went through the formation of the thioacetic d_3-acid-d which was prepared following the Schiff and Tarugi method[39,40] for the non-deuterated variant. Reaction with 2,2-bis(hydroxymethyl)-10-undecen-1-ol lead to the formation of the H_3L-d_3 tripodal ligand. The deuterated complex $[Fe_4(L\text{-}d_3)_2(dpm)_6]$ (named Fe_4C_9SAc-d_6) was prepared as for the non-deuterated analogue and checked by x-ray diffraction.[38]

The deuterated and non-deuterated complexes have been used for the preparation of self assembled monolayers on gold. In Figure 6.7 are shown

both hypotheses for the grafting mode, evidencing that they differ in the number of residual deuterium atoms.

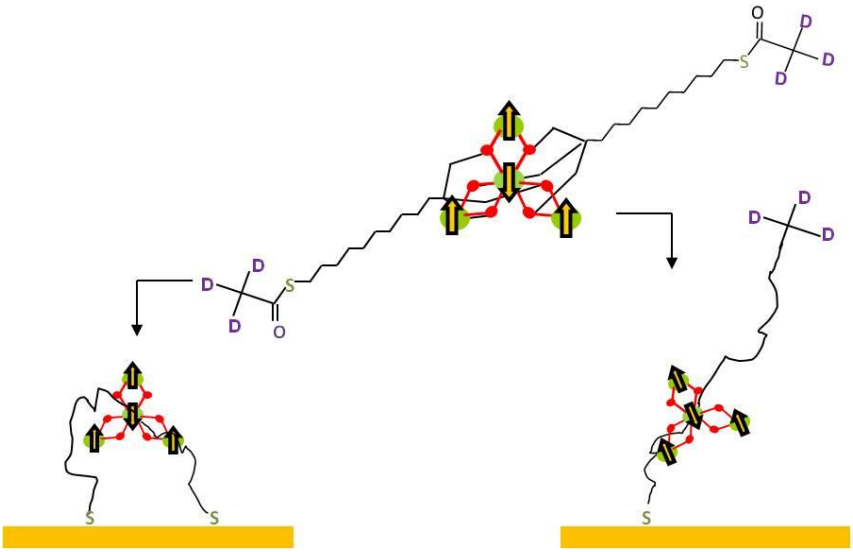

Figure 6.7: Schematic structure of the deutarated and graftable Fe_4 derivative and of the two possible grafting modes. The spin vectors or iron(III) ions are also shown.

6.4.1 Syntheses

2,2-Bis(hydroxymethyl)-10-undecen-1-ol was prepared by Tollens condensation of 10-undecenal with formaldehyde and CaO in an EtOH/water mixture.[41] Diethylether was distilled from its sodium benzophenone ketyl solution before use.[42] The deuterated complex [Fe_4(L-d_3)$_2$(dpm)$_6$] was prepared as described for the non-deuterated analogue.[38] Unless otherwise stated, all other chemicals were reagent grade and used as received.

Thiolacetic-d_3 acid-*d* Acetic-d_3 acid-*d* (20.0 ml, 0.349 mol, Armar, 99 %D), P_2S_5 (20.7 g, 0.0931 mol) and crushed glass (5 g) were introduced into a distillation apparatus equipped with a short Vigreux column, a thermometer and a $CaCl_2$ valve. The mixture was slowly heated to 50-75 °C over 30min using an oil bath. A further temperature increase to 85-90°C caused a vigorous reaction to start, with concomitant raise of distillation temperature to 100-105°C and distillation of a yellow-orange liquid (8.33 g). The liquid was carefully fractionated at ambient pressure with protection against moisture to give thiolacetic-d_3 acid-*d* as a colourless liquid (b.p. 84-87.5°, 4.39 g). According to ^{1}H NMR, the sample contains ca. 4.8 %mol of deuterated acetic acid. The higher boiling fractions contain a higher percentage of the starting acid. ^{1}H NMR ($CDCl_3$, 200 MHz) δ ppm: 4.65 (s, –S*H*), 2.36 (q, ^3J(H,D) = 2.2 Hz; CD_2H).

Thiolacetic-d_3 acid In a 25 ml separatory funnel thiolacetic-d_3 acid-*d* (1.00 ml, 13.3 mmol) was added to a solution of NaOH (13.3 mmol) in water (12 ml). The clear yellow solution was swirled, layered with diethylether (10 ml) and treated with 6.0 M HCl (2.25 ml) until acidic pH. The organic phase was separated and the aqueous phase was extracted with diethylether (2 × 10 ml). The combined organic phases were dried over $MgSO_4$ and heated to 70-75°C in a distillation apparatus equipped with a short Vigreux column and a $CaCl_2$ valve to remove most diethylether. According to ^{1}H NMR, the liquid residue so obtained (1.05 g) contained 77% by mass of thiolacetic-d_3 acid and was used without further purification in the following reaction step. ^{1}H NMR ($CDCl_3$, 200 MHz) δ ppm: 4.57 (s, –S*H*), 2.36 (q, ^3J(H,D) = 2.2 Hz; CD_2H).

11-(Acetyl-d_3-thio)-2,2-bis(hydroxymethyl)undecan-1-ol (H_3L-d_3) A 50-ml three-necked round-bottomed flask equipped with a reflux condenser and a nitrogen inlet was sequentially charged with 2,2-bis(hydroxymethyl)-10-undecen-1-ol (0.500 g, 2.17 mmol), anhydrous toluene (15 ml), thiolacetic-d_3 acid (0.52 ml of 77% w/w solution in Et_2O, *ca.* 4.8 mmol) and 2,2'-azobis(2-methylpropionitrile) (0.108 g, 0.658 mmol) under nitrogen atmosphere. The stirred mixture was heated to 80°C for exactly 4 hours.

The reaction was quenched by cautious addition of aqueous 1 M $NaHCO_3$ (3.3 ml), allowed to cool down to room temperature under nitrogen and treated with water (4 ml). The mixture was extracted with ethylacetate (30 ml), the organic phase was separated and the aqueous phase was further extracted with ethylacetate (2 × 20 ml). The combined organic phases were washed with brine (5 ml) and dried over $MgSO_4$. Complete solvent evaporation in vacuum gave the crude triol as a light yellow solid (0.567 g), which was purified by column chromatography (silica gel, 24 × 4 cm, dichloromethane:methanol 14:1) to give 11-(acetyl-d_3-thio)-2,2-bis(hydroxymethyl)undecan-1-ol as an off-white solid (0.445 g, 66%). ^{1}H NMR ($CDCl_3$, 200 MHz) δ ppm: 3.76 (s, 6 H; –CH_2OH), 2.87 (t, ^3J = 7.2 Hz, 2 H; CH_2S), 2.24 (s, 3H; O*H*), 1.65–1.50 (m, 2 H; CH_2CH_2S), 1.39–1.21 (m, 14 H; CH_2)

6.5 Mass spectrometry characterisation

In order to have consistent results from ToF-SIMS investigations we employed both Fe_4 molecules, the deuterated and the non-deuterated ones (Fe_4C_9SAc-d_6 and Fe_4C_9SAc) to record spectra of SAM and bulk samples, the latter obtained by the drop cast method. It's important to stress that the grafting procedure is performed without addition of deprotecting agents because of their incompatibility with the chemical nature of the complex.

Monolayers of Fe_4C_9SAc and Fe_4C_9SAc-d_6 were prepared by immerging flame-annealed evaporated gold on mica substrates in a 2 mM dichloromethane solution of the complex for 20 hours. The gold slabs were later washed by immersion in the same pure solvent for 10 minutes. Bulk reference samples, few hundreds nanometer thick, were prepared by drop casting 50 µl of a 2 mM dichloromethane solution of the complexes on similar gold substrates. All operations were carried out under dry nitrogen flow or in glovebox.

ToF-SIMS spectra, using a gold liquid-metal primary ion source, were acquired on SAM of both Fe_4C_9SAc and Fe_4C_9SAc-d_6 derivatives and on their corresponding bulk samples for reference, collecting both positive and negative ions. Here, only the significant, positive ones are showed. The most significant part of the spectrum, corresponding to the the region *m/z* 1350-2100 of positive ions, is reported in Figure 6.8 and summarized in Table 6.1.

H	D	Fe_4C_9SAc bulk	Fe_4C_9SAc – d_6 bulk	Fe_4C_9SAc SAM	Fe_4C_9SAc -d_3 SAM	Assignment
2086	2086	-	-	w	M	$[M - Ac + Au]^+$
2055	2055	-	-	-	-	$[M - dpm - 2Ac + 2Au]^+$
2050	2053	-	-	vw	Vw	$[M - SAc + Au]^+$
1929	1935	vw	Vw	-	-	$[M]^+$
1899	1902	-	-	s	S	$[M - dpm - Ac + Au]^+$
1747	1753	s	S	vw	Vw	$[M - dpm]^+$
1703	1706	w	w	m	M	$[M - dpm - Ac]^+$
1670	1673	vw	vw	m	M	$[M - dpm - SAc]^+$
1563	1569	m	m	-	-	$[M - 2dpm]^+$
1519	1522	-	-	w	W	$[M - 2dpm - Ac]^+$

Table 6.1: Characteristic peaks detected in the positive ToF-SIMS spectra of Fe_4C_9SAc (H) and Fe_4C_9SAc-d_6 (D) samples drop-cast and SAM.

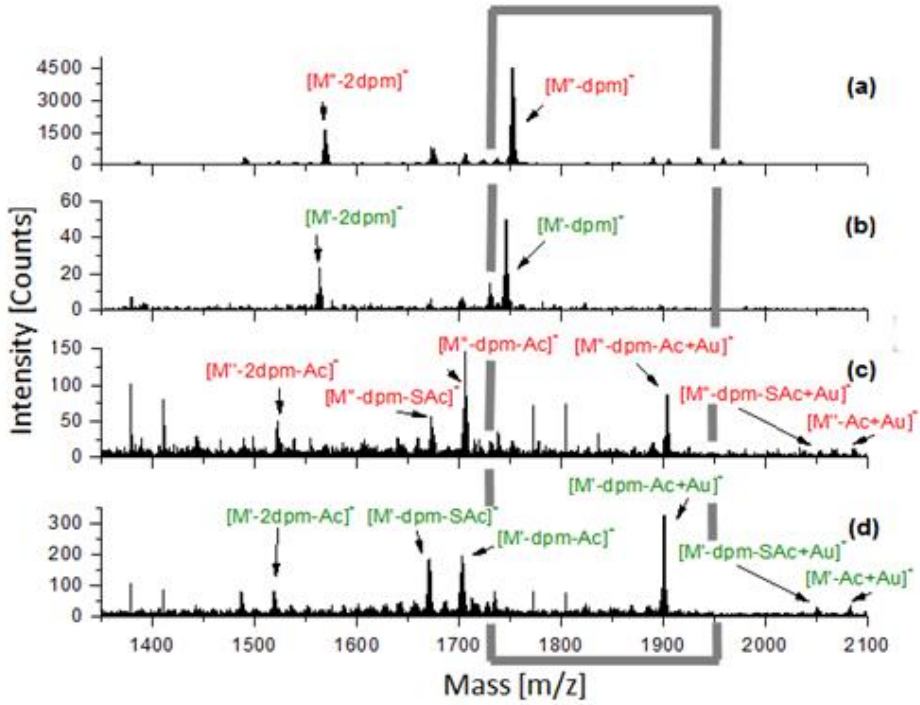

Figure 6.8: Positive ToF-SIMS spectra in *m/z* 1350-2100 region of:
(a) bulk $Fe_4C_9SAc\text{-}d_6$ (b) bulk Fe_4C_9SAc
(c) SAM $Fe_4C_9SAc\text{-}d_6$ (d) SAM Fe_4C_9SAc

Starting from the bulk samples – spectra **(a)** and **(b)** - we can notice that the most intense peaks of the spectrum arise from ion fragments which have lost one or two dpm ligand $[M\text{-}dpm]^+$, occurring at *m/z* 1747 (1753 for the deuterated complex) and $[M\text{-}2dpm]^+$ at *m/z* 1653 (1659), typical for these molecules.[24] The molecular peak M^+ (*m/z* 1929 – 1935 for Fe_4C_9SAc and $Fe_4C_9SAc\text{-}d_6$,respectively) is very weak in the spectrum of both samples.

Interestingly, the $[M\text{-}dpm]^+$ is practically absent in the SAM of Fe_4C_9SAc and very weak in that of $Fe_4C_9SAc\text{-}d_6$ – spectra **(d)** and **(c)** - confirming that the adopted cleaning procedure is able to remove practically all physisorbed species. In both SAMs the *m/z* 1900 (1903) peak, that does not compare in the bulk spectrum, turns out to be the most meaningful and distinctive. This peak can be unambiguously associated to the fragment of formula $[M\text{-}dpm\text{-}Ac+Au]^+$, as the 3 *m/z* shift between the two samples confirms that one Ac-d_3 group has been lost. This observation, as well as those of other, although weaker, peaks like the *m/z* 2083 (2086) attributed to the $[M–Ac+Au]^+$ fragment, confirm the hypothesis that the grafting process leads to spontaneous deprotection of the sulphur atom.

In Figure 6.9 are shown expanded views of the spectra for the main mass peak, focusing on the fragments $[M\text{-}dpm]^+$ and $[M\text{-}dpm\text{-}Ac+Au]^+$. The isotopic distributions calculated for these fragments are coherent with the experimental spectra and confirm the right assignment of each peak.

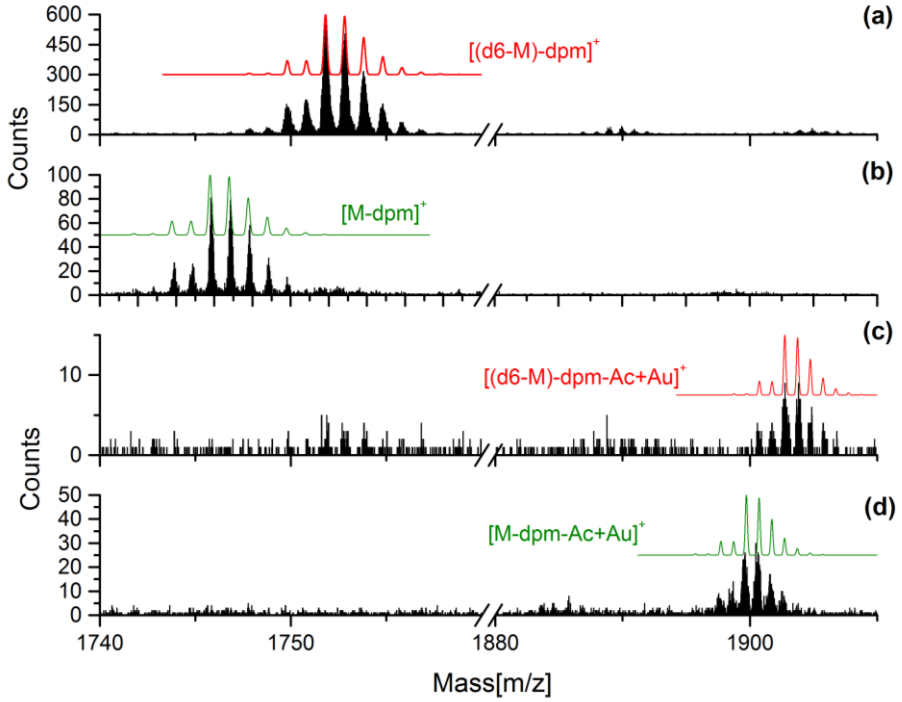

Figure 6. 9: Expansion of the four ToF-SIMS spectra in the region of the relative interesting peak. The red and the green line are the calculated isotopic distribution.
(a)bulk $Fe_4C_9SAc\text{-}d_6$ (b) bulk Fe_4C_9SAc
(c) SAM $Fe_4C_9SAc\text{-}d_6$ (d) SAM Fe_4C_9SAc

For what concerns the double grafting, it is interesting to notice that there is no experimental evidence about its formation. The lack of any significant fragments having lost both acetyl group, *e.g.* $[M\text{-}dpm\text{-}2Ac+2Au]^+$ (*m/z* 2055) however does not allows to exclude completely its formation. We can say that recently Au nanoparticles surface-functionalised with Fe_4 have been synthesised, where an extended network is formed thanks to the bridging capabilities of the bi-functionalised Fe_4 molecules. This suggests that grafting of the two anchoring groups on the same substrate is not a particularly favoured configuration. It must be said that in that case a different linking group, the thioctic moiety, was employed.[43]

6.6 Conclusions

In order to investigate how star-shaped tetrairon(III) complexes graft onto a gold surface, a deuterated analogue of Fe_4C_9SAc, $Fe_4C_9SAc\text{-}d_6$ have been synthesised. These molecules are provided with two alkoxide tripodal ligands which make the structure more robust and contain the labelled protecting anchor group -SAc. ToF-SIMS measurements were performed on the bulk and self assembled monolayer samples and the spectra were compared.

Firstly it is worth noting that the primary ions used, Au^+, despite being of the same chemical nature of the atoms of the substrate, do not interact with the deposited molecules and don't compromise the measurements. No observed peak of the bulk sample shows the addition of atoms of gold into the released fragment.

From the experimental data obtained we can conclude that the deposit of molecules on the gold substrate is a chemisorbed monolayer. The main peak for the bulk sample revealed to be the fragment in which the molecule has lost a dpm ligand $[M\text{-}dpm]^+$, which does not appear in the SAM sample. It means that all the physisorbed specie are have been removed through the washing operations in the SAM preparation.

Moreover the most intense peak, regarding the SAM samples, is the one assigned to $[M\text{-}dpm\text{-}Ac+Au]^+$, confirmed by the calculated isotopic distribution. The mass shift, of this peak, between the deuterated and non-deuterated sample demonstrate that one acetyl protecting group undergoes a cleavage in the formation of the S-Au bond. Thus, certainly, a mono-grafting of the molecules to the surface occurs. Instead no peak of a double grafting can be revealed, which however does not fully rule out the formation of two S-Au bonds in the same Fe_4C_9SAc molecule.

These results clearly supports our previous evidences of the formation of a monolayer-based film and suggest that the grafting strategy adopted here can be extended to heterometallic star shaped SMMs with improved magnetic properties, *e.g.* the Fe_3V systems described in chapter 4, are modified when organised in nanostructures or if, like in the case of Fe_3Cr[44] the deposition on gold surface is not altering the magnetic properties of this versatile family of SMMs.

(1) Joachim, C.; Gimzewski, J. K.; Aviram, A. *Nature* **2000**, *408*, 541–548.

(2) Bogani, L.; Wernsdorfer, W. *Nat. Mater.* **2008**, *7*, 179–186.

(3) Cornia, A.; Mannini, M.; Sainctavit, P.; Sessoli, R. *Chem. Soc. Rev.* **2011**, *40*, 3076–3091.

(4) Yamada, H.; Imahori, H.; Nishimura, Y.; Yamazaki, I.; Ahn, T. K.; Kim, S. K.; Kim, D.; Fukuzumi, S. *J. Am. Chem. Soc.* **2003**, *125*, 9129–9139.

(5) Ulman, A. *Chem. Rev.* **1996**, *96*, 1533–1554.

(6) Kluth, G. J.; Sander, M.; Sunga, M. M.; Maboudian, R. *J. Vac. Sci. Technol. A* **1998**, *16*, 932–936.

(7) Rodriguez-Douton, M. J.; Mannini, M.; Armelao, L.; Barra, A.-L.; Tancini, E.; Sessoli, R.; Cornia, A. *Chem. Commun. (Camb).* **2011**, *47*, 1467–1469.

(8) Mannini, M.; Pineider, F.; Sainctavit, P.; Danieli, C.; Otero, E.; Sciancalepore, C.; Talarico, A. M.; Arrio, M.-A.; Cornia, A.; Gatteschi, D.; Sessoli, R. *Nat. Mater.* **2009**, *8*, 194–197.

(9) Mannini, M.; Pineider, F.; Danieli, C.; Totti, F.; Sorace, L.; Sainctavit, P.; Arrio, M.; Otero, E.; Joly, L.; Cezar, J. C.; Cornia, A.; Sessoli, R. *Nature* **2010**, *468*, 417–421.

(10) Díaz, C.; Araya, E.; Santa Ana, M. A. *Polyhedron* **1998**, *17*, 2225–2230.

(11) Tour, J. M.; Jones, L.; Pearson, D. L.; Lamba, J. J. S.; Burgin, T. P.; Whitesides, G. M.; Allara, D. L.; Parikh, A. N.; Atre, S. *J. Am. Chem. Soc.* **1995**, *117*, 9529–9534.

(12) Cai, L.; Yao, Y.; Yang, J.; Price, D. W.; Tour, J. M. *Chem. Mater.* **2002**, *14*, 2905–2909.

(13) Shirai, Y.; Cheng, L.; Chen, B.; Tour, J. M. *J. Am. Chem. Soc.* **2006**, *128*, 13479–13489.

(14) Genorio, B.; He, T.; Meden, A.; Polanc, S. *Langmuir* **2008**, *24*, 11523–11532.

(15) Park, T.; Kang, H.; Choi, I.; Chung, H. *Bull. Korean Chem* **2009**, *30*, 441–444.

(16) Béthencourt, M. I.; Srisombat, L.; Chinwangso, P.; Lee, T. R. *Langmuir* **2009**, *25*, 1265–1271.

(17) Vaughan, O. P. H.; Turner, M.; Williams, F. J.; Hille, A.; Sanders, J. K. M.; Lambert, R. M. *J. Am. Chem. Soc.* **2006**, *128*, 9578–9579.

(18) Jaccob, M.; Rajaraman, G.; Totti, F. *Theor. Chem. Acc.* **2012**, *131*, 1150.

(19) Stapleton, J. J.; Harder, P.; Daniel, T. A.; Reinard, M. D.; Yao, Y.; Price, D. W.; Tour, J. M.; Allara, D. L. *Langmuir* **2003**, *19*, 8245–8255.

(20) Singh, A.; Dahanayaka, D. H.; Biswas, A.; Bumm, L. a; Halterman, R. L. *Langmuir* **2010**, *26*, 13221–12226.

(21) James M. Tour, LeRoy Jones II, Darren L. Pearson, Jaydeep J. S. Lamba, Timothy P. Burgin, George M. Whitesides, David L. Allara, Atul N. Parikh, S. A. *J. Am. Chem. Soc.* **1995**, *117*, 9529–9534.

(22) Lau, K. H. A.; Huang, C.; Yakovlev, N.; Chen, Z. K.; O'Shea, S. J. *Langmuir* **2006**, *22*, 2968–2971.

(23) Barra, A.-L.; Bianchi, F.; Caneschi, A.; Cornia, A.; Gatteschi, D.; Gorini, L.; Gregoli, L.; Maffini, M.; Parenti, F.; Sessoli, R.; Sorace, L.; Talarico, A. M. *Eur. J. Inorg. Chem.* **2007**, *2007*, 4145–4152.

(24) Pineider, F.; Mannini, M.; Danieli, C.; Armelao, L.; Piras, F. M.; Magnani, A.; Cornia, A.; Sessoli, R. *J. Mater. Chem.* **2010**, *20*, 187–194.

(25) Vickerman, J. C.; Brown, A.; Reed, N. M. *Secondary Ion Mass Spectrometry : Principles and Applications*; Clarendon: Oxford, U.K., **1989**.

(26) Ghonaim, N. W.; Nieradko, M.; Xi, L.; Nie, H.-Y.; Francis, J. T.; Grizzi, O.; Yeung, K. K. C.; Lau, L. W. M. *Appl. Surf. Sci.* **2008**, *255*, 1029–1032.

(27) Leone, G.; Consumi, M.; Lamponi, S.; Magnani, A. *Appl. Surf. Sci.* **2012**, *258*, 6302–6315.

(28) Mannini, M.; Sorace, L.; Gorini, L.; Piras, F. M.; Caneschi, A.; Magnani, A.; Menichetti, S.; Gatteschi, D. *Langmuir* **2007**, *23*, 2389–2397.

(29) Tencer, M.; Nie, H.-Y.; Berini, P. *Appl. Surf. Sci.* **2011**, *257*, 4038–4043.

(30) Mrksich, M. *ACS Nano* **2008**, *2*, 7–18.

(31) Sabbatini, L.; Zambonin, P. G. *Surface Characterisation of Advanced Polymers*; Wiley, **1993**; p. 304.

(32) Eynde, X. Vanden; Reihs, K.; Bertrand, P. *Macromolecules* **1999**, *32*, 2925–2934.

(33) Chilkoti, A.; Castner, D. G.; Ratner, B. D. *Appl. Spectrosc.* **1991**, *45*, 209–217.

(34) Morris, M. R.; D.E. Riederer, J.; Winger, B. E.; Cooks, R. G.; Ast, T.; Chidsey, C. E. D. *Int. J. mass Ion Process.* **1992**, *122*, 181–217.

(35) Frisbie, C. D.; Martin, J. R.; Duff, R. R.; Wrighton, M. S. *J. Am. Chem. Soc.* **1992**, *114*, 7142–7145.

(36) Tancini, E.; Rodriguez-Douton, M. J.; Sorace, L.; Barra, A.-L.; Sessoli, R.; Cornia, A. *Chem. Eur. J.* **2010**, *16*, 10482–10493.

(37) Cornia, A.; Fabretti, A. C.; Garrisi, P.; Mortalò, C.; Bonacchi, D.; Gatteschi, D.; Sessoli, R.; Sorace, L.; Wernsdorfer, W.; Barra, A.-L. *Angew. Chemie (International ed.)* **2004**, *43*, 1136–1139.

(38) Accorsi, S.; Barra, A.-L.; Caneschi, A.; Chastanet, G.; Cornia, A.; Fabretti, A. C.; Gatteschi, D.; Mortalo, C.; Olivieri, E.; Parenti, F.; Rosa, P.; Sessoli, R.; Sorace, L.; Wernsdorfer, W.; Zobbi, L. *J. Am. Chem. Soc.* **2006**, *128*, 4742–4755.

(39) Schiff, R. *Ber.* **1895**, *28*, 1204–1206.

(40) Tarugi, N. *Gazz. Chim. Ital.* **1895**, *25*, 269–273.

(41) Muth, A.; Asam, A.; Huttner, G.; Barth, A.; Zsolnai, L. *Eur. J. Inorg. Chem.* **1994**, *127*, 305 – 311.

(42) Armarego, W. L. .; Perrin, D. . *Purification of Laboratory Chemicals*; 4th ed.; Butterworth-Heinemann, **1997**; p. 544.

(43) Perfetti, M.; Pineider, F.; Poggini, L.; Otero, E.; Mannini, M.; Sorace, L.; Sangregorio, C.; Cornia, A.; Sessoli, R. *Small* **2013**. (10.1002/smll.201301617)

(44) Tancini, E.; Mannini, M.; Sainctavit, P.; Otero, E.; Sessoli, R.; Cornia, A. *Chem. Eur. J.* **2013**, *19*, 16902–16905.

Acknowledgements

I would like to express my gratitude to Prof. Roberta Sessoli and Prof. Andrea Caneschi for the opportunities they gave me, even before this work formally started. Their friendly way to be the bosses makes the lab a family place. I extend my heartfelt acknowledgments to the whole LAMM group. Everyone there taught me something during these long (but short) three years. Many thanks to Dr. Lorenzo Sorace for his boundless competence. Thanks to *Docteur* Marie Emmanuelle Boulon for sharing with me good times and bad times in the lab and for her sincerity, the help she offered me was always precious. A very special thanks goes to Dr. Matteo Mannini for his support in extremis moments. I sincerely want to thank Dr. Pine and Dr. Pone, because they have been older brothers for me. Thanks to all 3387 crew and to the ones who are my Friends before being colleagues.

A special thanks to Prof. Andrea Dei because every conversation with him surely is a stimulating and funny one.

A sincere thanks to Dr. Samuele Ciattini for his brilliant support and for his iron-y.

Professional and infinite personal thanks to Prof. Jaísa Fernandes Soares for everything she did for me, for what she taught me, for the complete availability she demonstrated and for illimitable perseverance. I will never be able to exchange them. I would also thank all my friends from Curitiba, who made warmer the cold *chuvitiban* winter.

Thanks to my friends and flatmates because a day cannot be a normal one with them.

Thank to my family, for being there.

Finally, my greatest and loving gratitude goes to Olimpia, the person who is always beside me and I’m happy about it.